Closing the Gap to the Diffraction Limit: Near Wavelength Limited Tabletop Soft X-Ray Coherent Diffractive Imaging

by

Richard Lunt Sandberg

B.A., Brigham Young University, 2004

A thesis submitted to the

Faculty of the Graduate School of the

University of Colorado in partial fulfillment

of the requirements for the degree of

Doctor of Philosophy

Department of Physics

2009

This thesis entitled:
Closing the Gap to the Diffraction Limit: Near Wavelength Limited Tabletop Soft X-Ray Coherent Diffractive Imaging
written by Richard Lunt Sandberg
has been approved for the Department of Physics

Prof. Henry C. Kapteyn

Prof. Margaret M. Murnane

Date

The final copy of this thesis has been examined by the signatories, and we find that both the content and the form meet acceptable presentation standards of scholarly work in the above mentioned discipline.

Sandberg, Richard Lunt (Ph.D., Physics)

Closing the Gap to the Diffraction Limit: Near Wavelength Limited Tabletop Soft X-Ray Coherent Diffractive Imaging

Thesis directed by Prof. Margaret M. Murnane and Prof. Henry C. Kapteyn

Light microscopy has greatly advanced our understanding of nature. The achievable resolution, however, is limited by optical wavelengths to around 200 nm. Using novel imaging and labeling technologies, resolutions beyond the diffraction limit can be achieved for specialized specimens using techniques such as near-field scanning optical microscopy, stimulated emission depletion microscopy and structured illumination microscopy [1–3]. This dissertation presents a versatile soft x-ray diffraction microscope with 50 nm resolution using tabletop coherent soft x-ray sources. This work represents the first high resolution demonstrations of coherent diffractive or lensless imaging using tabletop extreme ultraviolet and soft x-ray sources [4, 5].

This dissertation also presents the first use of field curvature correction in x-ray coherent imaging which allows high numerical aperture imaging and near-diffraction-limited resolution of 1.5λ. The relevant theory behind high harmonic generation, the primary tabletop source used in this work, will be discussed as well as the theory behind coherent diffractive imaging. Additionally, the first demonstration of tabletop soft x-ray Fourier Transform holography is shown with important applications to shorter wavelength imaging with high harmonic generation with limited flux. A tabletop soft x-ray diffraction microscope should find broad applications in biology, nanoscience, and materials science due to its simple optical design, high resolution, large depth of field, 3D imaging capability, scalability to shorter wavelengths, and ultrafast temporal resolution.

Dedication

"Trust in the Lord with all thine heart; and lean not unto thine own understanding.

In all thy ways acknowledge him, and he will direct thy paths."' Proverbs 3:5-6

To my best friend and wife Deanne

Acknowledgements

First of all, I feel very lucky to have worked with my advisors, Margaret Murnane and Henry Kapteyn. Thanks for your generosity, perspective, support, encouragement, and advice. I was extremely blessed to have had great coworkers, life-coaches, and friends in so many who were instrumental in this work, especially Ariel Paul, Daisy Raymondson, and Bill Schlotter. From UCLA, John Miao, Changyong Song, Kevin Raines and others for image reconstructions and being excellent teachers, friends, and collaborators. Many thanks to all in KM Group: Chan La-o-vorakiat, Matt Seaberg, Ethan Townsend, Luis Miaja-Avila, Mark Siemens, Amy Lytle, Paul Arpin, Ra'anan Tobey, Dave Gadiosi, Oren Cohen, Steffen Hädrich, Jim Holtsnider, Scott Hoch, Nick Wagner, Rachael and Matt Tearle, Kim Reid, Sterling Backus and KM Labs and so many others that I don't have room to list. Thanks to the EUV ERC: at CSU Przemek Wachlak, Mario Marconi, Carmen Menoni, Jorge Rocca, and Sheila Davis; at CXRO Anne Sakdinawat, David Attwood, Yanwei Liu, and Farhad Salmassi. In OSEP: Ricki Hadow, Dana Anderson, Matt Squiers, Barb Tennis, Dan Dessau at CU and Dave Pappas at NIST and groups, NSF and OSA (for $). In JILA/CU: Hans Greene, Dave Alchenberger, all Instrument, Electronics, and other staff and the summer Ultimate lunch crew. Thanks to former undergrad friends and mentors at BYU and Bruno La Fontaine and group at AMD. I'm sure I'm forgetting so many, thanks to you too. Finally, thanks to family, friends, especially my parents, and to Deanne, our beautiful kids Karadyn, Savannah, and Nathan, and to God for everything.

Contents

Chapter

Figures

Figure

Chapter 1

Introduction to Tabletop Coherent Diffractive X-ray Imaging

This thesis will present the first results of a high resolution (<100 nm) diffractive x-ray microscope using a tabletop, coherent x-ray source. Originally developed at large, 3rd generation synchrotron sources, this technique for nano-scale imaging is elegant when applied to more limited flux, tabletop x-ray sources because of its stability, robustness, and ability to produce high resolution images without the need of difficult to manufacture and lossy imaging optics. Additionally, as will be shown, this technique is applicable in high numerical aperture schemes meaning that the resolution is ultimately limited not by the point spread function of the imaging optic, but by source brightness, wavelength, and radiation damage of the sample [23]. The source used for the majority of the work presented in this thesis is phase matched high harmonic generation of an intense femtosecond laser. This source is very attractive because of its complete spatial coherence and high temporal coherence, compactness, stability, and ability to produce sub-femtosecond pulses of x-rays ($< 10^{-15}$ s). However, first this chapter will review the basic principles of microscopy as well as compare several microscopy modalities in order to provide a framework against which to present the results.

1.1 Imaging at the nanoscale

Microscopy is a critical enabling tool for understanding the nano-world. Since Hooke first applied the microscope to viewing the cellulose structure in cork [28], mi-

croscopy has had an especially important impact on biology. Standard visible light microscopes can image living cells with a resolution as low as 200 nm [29], especially with the use of fluorescent markers. However, this resolution is fundamentally limited by the wavelength of visible/near-UV light. Increasing the resolution in imaging has driven technology and science in areas as disparate as biotechnology, semiconductor fabrication, materials science, and defense.

Traditionally, the resolution of an imaging system is described by the so called Rayleigh Criterion [6, 29]. This limit is given by

$$r = \frac{0.61\lambda}{NA} \tag{1.1}$$

where r is the transverse or spatial resolution, λ is the illuminating wavelength, NA is the numerical aperture of the imaging system, and the prefactor (0.61) comes from Rayleigh's criterion for resolving two points imaged with system with circular apertures. Abbe put forth a similar resolution criterion in his seminal work on microscope design, where the prefactor is 0.5 [1,30,31]. To further increase resolution, two major strategies have been taken: increasing the numerical aperture and decreasing the wavelength.

Increasing the numerical aperture of a microscope is a common practice, and high quality, high numerical aperture lenses have found numerous applications. The numerical aperture (NA) of a lens is given by

$$NA = n \sin\theta \tag{1.2}$$

where n is the index of the refraction of the material between the sample and objective lens and θ is the half angle of the light collected by the objective lens [32]. High quality, short focal length objective lenses are available for optical microscopes with a practical collection angle of up to about 72° ($NA = \sin(72°) \cong 0.95$). With the development of immersion microscopy–where the air gap between the sample and objective lens is replaced with a higher index of refraction material–numerical apertures of 1.4 are

practical with high quality immersion oil ($n = 1.51$) [29, 33, 34]. Immersion optics have found numerous applications in biological imaging and semiconductor lithography where they have allowed sub-wavelength information to be extracted (as in microscopy) or imprinted (as in lithography) [1, 2, 35]. However, even with these techniques the resolution of optical microscopes is limited to about 200 nm [36]. In the next section we will discuss different types of imaging techniques that work to beat this optical resolution barrier and compare their advantages and disadvantages.

1.2 Comparison of different microscopies

This section will compare and contrast different imaging techniques that strive to push imaging from the microscopic regime to the nanoscopic regime. The discussion will focus on far-field techniques that can be used to extract three dimensional information of thick samples as opposed to near field or scanning probe techniques. These near field and scanning probe techniques, such as atomic force microscopy or near field optical microscopy can achieve very high resolution, even atomic resolution in some cases, but are limited to studies of the surfaces of samples [37]

1.2.1 Optical Microscopy

Optical microscopies have been the work horse of microscopy for centuries. Due to their compact and relatively inexpensive nature, optical microscopes are ubiquitous in elementary school class rooms and biotechnology firms alike. However, until the last decade the resolving power of optical microscopes has been limited by a diffraction limited spot of the optical wavelength ($\sim \lambda/2$) [1, 31].

One of the main advances in optical biological microscopies has been the use of green fluorescent proteins (GFP) as markers or labels that can be introduced into biological systems. This fact was recognized by the awarding of the 2008 Nobel prize in Chemistry to Osamu Shimomura, Martin Chalfie, and Roger Y. Tsien for "the discovery

and development of the green fluorescent protein" [38]. These proteins typically absorb light in the blue region of the spectrum and fluoresce at longer wavelengths in the green portion. Several techniques utilize these markers to increase or isolate the signal from these proteins through the means of spectral or spatial filtering. Several of these techniques are summarized in Figure 1.1 from the excellent review by Stefan Hell entitled "Far-field optical nanoscopy" [1]. The first pane of Figure 1.1 demonstrates a very common optical technique known as confocal microscopy. Confocal microscopy places a pinhole in the focal plane of the objective lens and thus rejects out of focus light from the sample. Additionally, confocal microscopy can be used in a scanning modality where a single, diffraction limited spot can be scanned around a sample. Thus, it is possible to illuminate a single GFP molecule and locate it to $\sim$ 200 nm. While an increase in image quality ensues, there is no true enhancement of resolution unless the pinhole size is reduced which sacrifices image intensity and acquisition speed. The next technique described is 4Pi, where two counter propagating beams illuminate a sample and set up a standing wave [1, 39]. A three dimensional interference pattern is produced where a sub-wavelength spot exists at the focus of the system. Thus in a similar fashion as confocal microscopy, a single small volume of the sample can be interrogated. However, 4Pi has the drawback of having side lobes of the interference pattern next to the focal spot that must be accounted for.

A similar technique to 4Pi that holds great promise is structured illumination (SI) microscopy as demonstrated by Gustafsson [40]. In SI, pupil fill filtering or apodization is used to produce a sinusoidally varying illumination pattern where the period of the sinusoidal illumination can be as small as half the wavelength of light. Multiple images of a sample illuminated with such a pattern are taken while the illumination pattern is rotated and shifted by $\lambda/2$. These images, which are Moiré patterns, are then processed in a computer and an enhancement of a factor of 2 in resolution to about 100 nm can be achieved. A nonlinear version of this techniques that involves saturation of

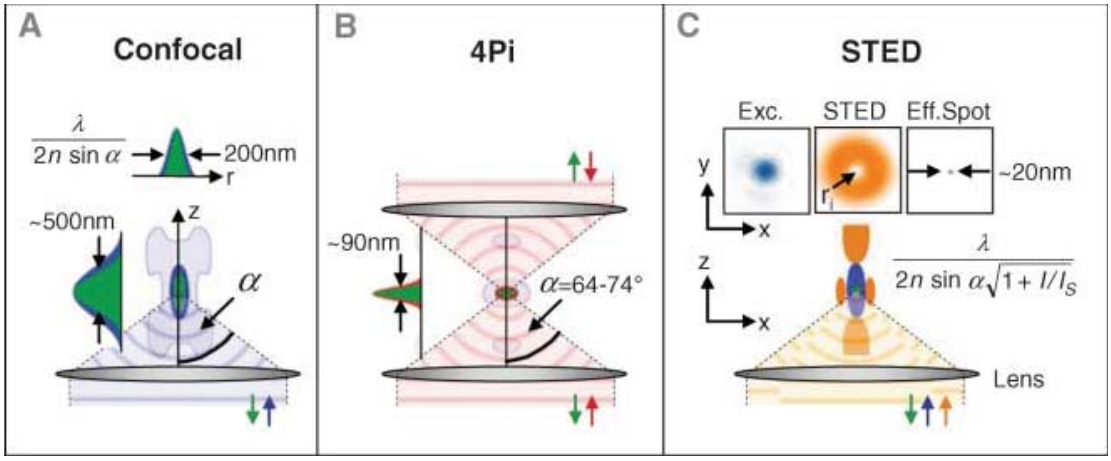

Figure 1.1: Description of three popular optical techniques to beat the diffraction limit using fluorescent proteins as markers from [1]. A) Description of confocal microscopy where a pinhole in the focal plane of the objective microscope reduces out of focus light from fluorescence (green wave) of a green fluorescent protein (GFP) illuminated by the blue wave. B) Description of the 4Pi technique whereby two counter propagating beams (red waves) interfere and produce a sub-diffraction limited spot. C) Description of STED, where a probe laser (blue wave) is used to excite a large spot of many GFP molecules. A second laser (orange wave) and a singular optics is used to produce a phase vortex and donut mode that quenches fluorescence from all GFP except what is in the center of the beam. Thus fluorescence from only a very small spot is gathered.

the GFP has also been demonstrated with $\sim$ 50 nm resolution [3]. One advantage of this technique is that it is a full-field technique as opposed to a scanning technique such as confocal scanning microscopy. The drawback to this technique is that it uses a computer reconstruction algorithm, that data collection can take a long time, and that in the case of the nonlinear technique high intensities are needed that can damage biological samples.

One final set of optical imaging techniques that perhaps has the most promise is a set that uses the ability of the GFP to be placed in a so called dark state where the GFP will not fluoresce [1]. This can be achieved by a variety of means, but most modalities use saturation of the protein as means to increase resolution by essentially turning off proteins you do not want to image. One of the most popular techniques in this category is stimulated emission depletion microscopy (STED). STED is depicted in panel (C) of Figure 1.1. As shown in the figure, this technique uses two illuminating beams. The first beam illuminats the GFP and excites it. The second beam passes through a singular optic which produces a phase vortex donut beam which has a minimum at the axial center. This beam saturates all the GFP illuminated by the first beam, except in the central null. In this way, fluorescence from a sub-diffraction limited spot can be collected. Many variations on technique have been introduced both in scanning and full field modalities and have produced images with resolution down to some 10's of nanometers when combined with time resolved readout and computer algorithms for fitting of point spread functions [1]. One final imaging technique that is worth mentioning is multiphoton microscopy where the second or third harmonic of an intense ultrafast laser pulse is detected. This technique utilizes the fact that the second order or third order nonlinear cross section of materials is smaller than the first order absorption cross section. However typically this means using red or near IR pulses which moves a diffraction limited spot size more towards 400 nm rather than 200 nm.

These modern optical techniques have truly broken the 200 nm barrier, but they

have some drawbacks. First, the optical systems have become much more complicated and expensive requiring $100,000 to upwards of $1 million dollars for systems that can produce three dimensional images with 50 nm resolution or less. Much of this expense comes from high quality, closed loop piezoelectric stages that can provide nanometer step resolution and nanometer stability. Additionally, mechanical stability of less than the optical resolution is required for these techniques. Finally, all of these techniques except for multi photon microscopy require labeling with GFP. While this technique has become a gold standard in biological imaging, it has not found as many implementations in materials science imaging.

1.2.2 Electron Microscopy

After optical microscopy, the next most commonly used microscopic technique is the electron microscope. Since Ernst Ruska built the first electron microscope in 1931, it has found countless applications in biology, physical science, and material science and engineering. Due to the large impact of his invention, Ruska was awarded the 1986 Nobel prize in Physics [38]. The electron microscope uses the fact that high energy electrons have an extremely short wavelength. The quantum mechanical description of the electron's de Broglie wavelength is given by

$$\lambda = h/p = \frac{h}{\sqrt{2m_0eU}} \tag{1.3}$$

where h is Planck's constant, m_0 is the electron's mass, e the electrons charge, and U the accelerating electric potential. Most electron microscopes have accelerating potentials between 10kV and some few 100kV, making the electrons velocity relativistic. Hence the relativistic wavelength of the electron wavelength will be

$$\lambda = h/p = \frac{h}{\sqrt{2m_0eU}} \frac{1}{\sqrt{1 + \frac{eU}{2m_0c^2}}} \tag{1.4}$$

where c is the speed of light [41]. Thus, an electron that is accelerated across a 30 kV potential will have a wavelength of 0.012 nm (0.12 Å). Thus we see from equation

1.1 that even with modest numerical aperture electron microscopes atomic resolution is feasible and it has been demonstrated [41].

Electron microscopes can be classified into two basic classifications: scanning electron microscopes (SEM) and transmission electron microscopes (TEM) [41]. Scanning electron microscopes typically raster scan a focused electron spot over a sample and collect the secondary electrons released or the backscattered electrons. Therefore, SEMs are very surface sensitive and often require labeling or coating with materials that will increase the contrast of the electron intensity image. Transmission electron microscopes also typically scan a focused spot of electrons over the sample, but instead detects the transmitted electron intensity. Both SEM and TEM can be used for elemental specific studies by spectrally resolving the energy of the transmitted or secondary electrons and comparing these spectra to known binding energies. Thus, electron microscopes have become a very powerful tool for nanoscale imagine with elemental specificity.

While electron microscopes have found broad application, there are several drawbacks that should be discussed here. First, the free mean path of high energy electrons in air is very short requiring electron microscopes to work in vacuum [1, 41, 42]. This added level of complexity may require many steps of sample preparation such as freeze drying, cryo-fixing, or chemical fixing, especially in biological or wet materials. Second, electrons are charged particles and interact very strongly with matter, giving them a very short mean free path of only a few hundreds of nanometers ($<$500 nm according to Spence [41]). Thus when trying to image thick samples such as a whole cell (few μm diameter) or when trying to produce three dimensional images, electron microscopy often requires sectioning of chemically or cryo-fixed samples possibly introducing structural damage or artifacts. Additionally, the high energies of the electrons used means that they are ionizing radiation and cause sample damage [23, 41]. Finally, when high temporal resolution is required of dynamical processes, electron microscopy is limited in the shortness of the pulse durations it can produce to about 100 fs because of Coulombic

repulsion of the charged particles. In addition to electron microscopes, a gamut of other particle microscopes have come on line recently such as focused ion beam microscopes and neutral atom (typically He) microscopes. These microscopes are similar enough to electron microscopes in the function and application that they will not be discussed, but references [43, 44] provides more information on these devices.

1.2.3 X-ray Microscopy

X-ray microscopy provides an alternative approach to electron microscopy where high resolution imaging of thick samples is required. By virtue of its short wavelength, x-ray microscopy has made it possible to obtain nanometer-scale resolution images of whole unstained cells, magnetic permalloy wires, internal structures in nanocrystals, and magnetic domains in thin film samples [45–48]. Extreme ultraviolet and soft x-ray (EUV/SXR) radiation is particularly useful because it can penetrate relatively thick samples in comparison to electron microscopy, thus opening up the possibility for three-dimensional tomography of nano-objects. This region covers the electromagnetic spectrum from about 1 nm to 50 nm wavelength, or alternatively, from about 30 eV to 8 keV of photon energy as shown in Figure 1.2 from Attwood [6]. A very useful relationship between the photon energy, E in electron-volts (eV), and wavelength, λ in nm, is given by

$$E[eV] = \frac{1240[nm * eV]}{\lambda[nm]}. \tag{1.5}$$

Furthermore, as is shown in Figure 1.2, numerous core-level absorption edges and widely varying elemental absorption cross sections provide excellent inherent image contrast in the soft x-ray region of the spectrum. Two such examples are biological imaging around 400 eV or magnetic contrast imaging through x-ray circular dichroism in magnetic nanostructures around 800 eV [6, 45, 48]. Since EUV and SXR radiation is so strongly absorbed these wavelengths do not propagate readily through air, thus requiring a vacuum environment. However, at higher photon energies (5-10 keV) the mean free path

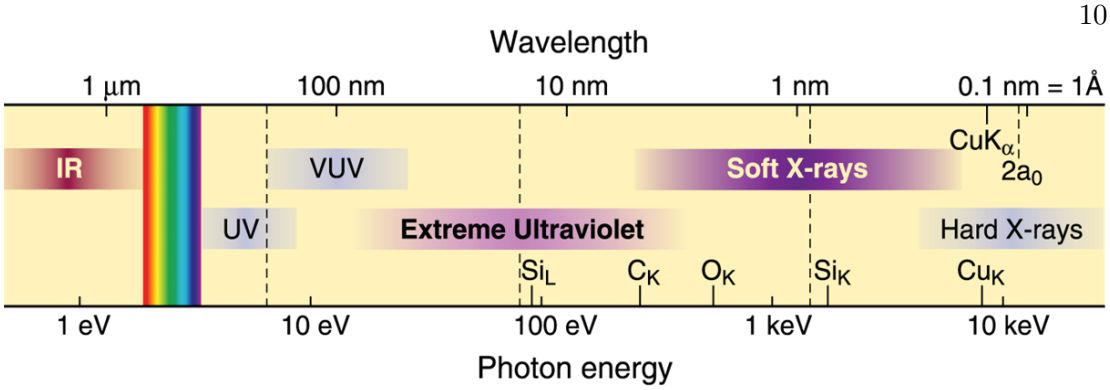

Figure 1.2: Electromagnetic spectrum with emphasis on the extreme ultraviolet (EUV) and soft x-ray imaging (SXR) portion. EUV/SXR microscopy has been shown to be useful because of the numerous absorption edges that exist in this region [6].

of x-rays in air is sufficiently long such that samples can be studied at atmosphere [6]. At those photon energies the dominant imaging process is phase contrast rather than absorption, so high contrast imaging becomes difficult. Additionally, radiation damage is a factor since EUV, SXR, and x-ray radiation are ionizing sources. These effects will be discussed later in chapter 3.

Two challenges have limited the broader application of soft x-ray microscopy: the difficult fabrication of x-ray imaging optics and the limited number of suitable x-ray sources available worldwide. Since soft x-rays are strongly absorbed by matter, diffractive or reflective optics (rather than refractive optics) must be used. The highest spatial resolution x-ray microscope demonstrated to date ($\sim$ 10 nm) used zone-plate condenser and focusing lenses with feature sizes as small as 15 nm [49]. These optics are thus challenging to fabricate and limited in availability. Moreover, the bright, tunable x-ray sources required for soft x-ray microscopy have generally only been available at a limited number of large-scale synchrotron facilities. Additional comparisons between zone plate imaging verses coherent imaging are discussed thoroughly in Ariel Paul's dissertation, chapter 5 [24].

However, recently, significant progress has been made that promises to open

up soft x-ray microscopy for more widespread use. First, new diffractive microscopy techniques using coherent x-ray beams have made possible nanometer-scale resolution imaging by essentially replacing the imaging optics in a microscope with a computer reconstruction algorithm [20, 22, 47, 48, 50–53]. Second, advances in coherent soft x-ray generation using tabletop ultrafast lasers have made it possible to implement practical tabletop soft x-ray sources with sufficient coherent flux for soft x-ray imaging [17,54–58].

1.3 Overview of work to be discussed

This dissertation will present recent work demonstrating coherent diffractive microscopy with an oversampling iterative phase retrieval algorithm (also called lensless imaging) using coherent, tabletop, soft x-ray sources. Chapter 2 will present the theory behind high harmonic generation (HHG) as a tabletop coherent soft x-ray source. Chapter 3 will present the important theory behind diffraction, sampling, and lensless or coherent x-ray imaging. Chapter 4 will discuss the first demonstration of high resolution (<100 nm) tabletop coherent x-ray imaging. The experimental setup and initial lower resolution results will be discussed as well as improvements necessary for higher resolution imaging. Image resolutions of 94 nm were obtained using 29 nm light produced by high-order harmonic upconversion of an ultrafast laser, while resolutions of 71 nm were obtained using a 46.9 nm soft x-ray laser [4, 5]. Much of this early work was done with Ariel Paul and additional details, especially on the experimental setup, can be found in his dissertation [24]. Next, another technique, Fourier Transform holography, will be demonstrated in chapter 5 with near 50 nm resolution using the same coherent tabletop x-ray source. This holographic technique has important applications for lower flux imaging with shorter wavelength sources. Finally, chapter 6 will present pathways towards shorter wavelengths and higher resolution as well as discussing important applications of a tabletop coherent x-ray microscope.

These techniques show great promise for further rapid progress. High harmonic

generation, for example, is attractive as a soft x-ray light source because it generates fully coherent beams with pulse durations of <10 fs using an extreme nonlinear optical upconversion technique. Moreover, the ultrafast laser systems required to implement a high harmonic light source are widespread and readily available. Currently, high harmonic beams with sufficient flux for diffractive or zone plate microscopy can be generated at wavelengths longer than 13 nm, where the nonlinear upconversion process can be phase matched [17, 55]. However, this source can also produce reduced flux at higher photon energies such as in the biologically important water window region [59,60] and even as high as 1 keV [61]. It has also been shown that high harmonic yields at these higher photon energies can be enhanced several orders of magnitude through the application of quasi-phase matching techniques [62–65] or through phase matching with longer wavelength lasers [66].

Chapter 2

High Harmonic Generation as a Bright, Coherent Source of EUV and SXR Radiation

2.1 Introduction to high harmonic generation

The development of a new generation of ultrafast lasers during the 1990's has had a significant impact on science and technology. These lasers have made accessible the regimes of extremely short time scales (femtosecond to attosecond dynamics), high bandwidth (hundreds of gigahertz), and very high field intensities (greater than a petawatt/cm^2) [13, 67]. The high field intensities achievable with ultrafast lasers have made possible entirely new types of nonlinear optical processes, and this in turn has spawned new techniques and technologies. One of these techniques, high harmonic generation (HHG), converts optical radiation at photon energies of $\sim$ 1.5 eV to extreme ultraviolet (EUV) or soft x-ray (SXR) radiation with photon energies up to several keV ($\sim$ 1 nm wavelength) [12, 61].

This chapter presents an introduction to high harmonic generation (HHG) from intense ultrafast lasers as a tabletop source of coherent x-rays. A brief history of the development of HHG is reviewed, and the semiclassical three-step model that describes this highly nonlinear optical effect is discussed. Various numerical models are considered that describe the quantum mechanical aspects of HHG. Finally, it will be shown how efficient HHG can be obtained through phase matching techniques and how phase matching in hollow waveguides produces highly coherent soft x-ray beams.

2.2 Ultrafast laser technology

As we will see in the following discussion, a necessary forerunner of tabletop high harmonic generation is the ability to produce very strong short laser pulses. One way to achieve this is through very intense optical laser pulses. Soon after the laser was first demponstrated in 1960 by Maiman, it was realized that this new device was a very useful tool for creating high peak fields [68]. Within two years the field of nonlinear optics was born when Franken and colleagues demonstrated optical harmonics by tightly focusing a laser into a quartz crystal [69]. Laser technology advanced rapidly in the next 40 years, and with that advancement came ever increasing peak intensity. However, until short-pulsed, broadband lasers were developed the ionization of atoms with laser fields was not attainable. Specifically, the development of ultrafast lasers was needed that produce pulses with durations on the order of picoseconds (ps or 10^{-12} s) or femtoseconds (fs or 10^{-15} s). Here we briefly review the developments that are pertinent to HHG as outlined in Backus et al [67].

One of the early pioneering methods developed in ultrafast laser science was modelocking a laser. When a laser is modelocked, it ceases to emit a steady beam of coherent radiation, but instead emits a train of short pulses. Throughout the 1980's, modelocked Neodymium-glass (Nd:glass) lasers or synchronously pumped and mode-locked dye lasers were common. These lasers were very unstable and would often drop out of the modelocked state. Also, these laser systems did not have enough bandwidth to produce very short duration pulses, thus limiting the duration of available pulsed lasers to the 100 fs to 1 ps range. Even though temperamental at times, these lasers were capable of high average power (10s of Watts). However, since the pulses were still relatively long (0.1-100 ps), peak laser intensities necessary for HHG (approximately 10^{13} W/cm^2) were limited to a few groups of scientists with state-of-the-art lasers. In the late 1980's and early 1990's, many developments in ultrafast lasers brought great

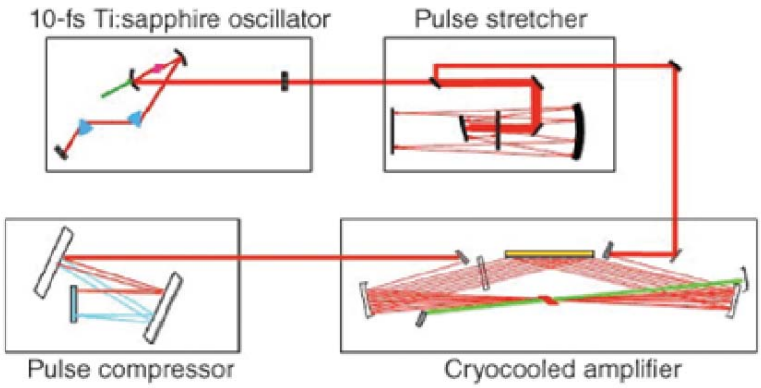

Figure 2.1: Schematic of a typical chirped-pulsed-amplifier (CPA) system with cryo-cooling. The output of a titanium-sapphire oscilator is stretched in a grating based stretcher and then amplified in a multipass amplifier. Finally, the amplified pulse is telescoped to a larger diameter and then compressed with a grating based compressor. This specific design is a KMLabs Dragon^{TM} design [7, 8].

progress in HHG [67]. Older style lasers such as the Nd:glass were improved and new lasers were introduced such as the titanium-doped sapphire laser (Ti:sapph). The mod-elocked Ti:sapph laser was introduced by Sibbet and his group in 1990 [70]. Ti:sapph is a very desirable laser material because it has a very broadband gain from approximately 700 nm to 1100 nm, meaning that ideally all of these wavelengths can be amplified in the crystal simultaneously [67]. Additionally, new laser amplifier systems were devel-oped such as chirped-pulse amplification or CPA. CPA uses two components known as a stretcher and compressor that spread out the pulse in time before amplification and then recompress it after amplification. This is necessary because the large pulse energies of approximately 1 mJ can easily damage the optics in the amplifier if the pulses are too short. After compression, the pulse duration can be as short as 5 fs with 1 mJ of energy at a repetition rate of several thousand Hz [67] These newer femtosecond lasers enabled researchers to obtain peak intensities that were previously unattainable with tabletop sources. In a 100 μm focus of a standard CPA ultrafast laser beam, peak intensities of 10^{18} W/cm^2 are easily achievable [67]. The peak electric field strength of these laser pulses can be many times higher than 10^9 V/cm, much higher than the binding field of

valence electrons of atoms [13].

2.3 Theory of High Harmonic Generation

High-order harmonic generation (HHG) of ultrashort-pulse lasers has emerged in the past decade as an attractive table-top source of EUV/SXR light with unique properties: HHG light is both coherent and can be used to generate light pulses even shorter than 100 as (attosecond is 10^{-18} s) in duration [12, 71–73]. High harmonic generation occurs when intense ultrashort laser pulses interact with atoms. Noble gases are typically used as targets. Noble gases are self restoring after being ionized (unlike crystals or solids) and have the highest ionization potential of all atoms. Their high ionization potentials allow the noble gas atoms' electrons to remain bound at higher laser intensities. Other compact sources of EUV radiation that are currently being used and further developed include laser produced plasmas and soft x-ray lasers [74, 75]. A good review of these sources is given in Attwood chapters 6-7 [6].

When light is incident on a material, the electric field polarizes the atoms or molecules of the material. This polarization in turn affects the propagation of the light in a way that is described by Maxwell's equations [76]. The induced polarization reradiates, both at the same frequency as the incident light, and in some cases, at high harmonics. For low intensities ($I \ll 10^{11} W/cm^2$), the induced polarization is linearly dependent on the electric field, E, and is given by

$$P = \epsilon_0 \chi E \tag{2.1}$$

where ϵ_0 is the permittivity of free space and χ is the electric susceptibility of the material [13]. If the polarization is oscillating, then the oscillating dipoles will reradiate light at the frequency of their oscillation as described by electromagnetic theory. As the incident intensity of the light is increased, the induced polarization reaches a nonlinear

regime where the induced polarization can be described by

$$P = \epsilon_0 \chi E + a_1 E^2 + a_2 E^3 + ... \tag{2.2}$$

where the ith-order term in this expansion is $P = a_i E^{i+1}$ and the nonlinear coefficient a_i is given by

$$a_i = \epsilon_0 \chi^i_{ijk} \tag{2.3}$$

χ^i_{ijk} where is the i^{th}-order electric susceptibility of the material. Equations 2.2 and 2.3 describe a perturbative expansion of the polarization that is valid as long as the higher order terms decrease monotonically. For a sinusoidal driving field $E(t) = E_0 cos(\omega t)$, the induced polarization includes higher order terms with frequencies of 2ω, 3ω, etc. These constitute second, third, and higher order harmonic generation. In these processes, multiple fundamental laser photons are absorbed and reemitted with the combined energy $q\hbar\omega$ in a single harmonic photon.

As mentioned earlier, if the intensity of the peak driving laser is increased even further to approximately 10^{13} to 10^{15} W/cm^2, the laser electric field will begin to approach the same strength as the Coulomb field binding the outermost electron of an atom [9]. In this range, the perturbation approach described above will not accurately describe the induced polarization because the electron will ionize, and the laser target is converted into a plasma. At these intensities, equation 2.2 does not converge, so traditional nonlinear optical theory does not suffice. This nonperturbative regime is known as the strong-field regime. The physics of multiphoton absorption and emission processes such as second harmonic generation and two photon absorbtion have corresponding higher-order processes in the strong field regime–HHG and above threshold ionization (ATI) [13] The later is a multiphoton ionization process in which more fundamental field photons are absorbed by an electron than are needed to exceed the binding Coulomb potential. In both HHG and ATI, the energy spectrum of either the photons or the photoelectrons produced in the process has a structure consisting of discrete peaks

that approximately correspond to multiples of the fundamental laser frequency.

2.3.1 Discovery and three step model

The transition from the perturbative regime to the strong field regime can be seen in the photoelectron and photon energy spectrum in ATI and HHG. In the perturbative regime, the intensities of successive peaks decrease monotonically so that the expansion in equation 2.2 converges. However, as the driving laser intensity is increased, more peaks appear, and all peaks increase in strength until a plateau of peaks with nearly equal intensity becomes apparent. These plateaus are characteristic of HHG spectra and were first observed in ultrafast laser studies of noble gases in the late 1980's [9, 77]. Figure 2.2 shows a typical HHG spectrum from Argon [77]. Notice the monotonic decrease of the first three peaks to the plateau region (harmonic order 7-29) followed by an abrupt cutoff (about the 33^{rd} harmonic). It is also interesting to note that HHG only produces odd harmonics. This is due to symmetry considerations in the nonlinear optical process – the generation of even harmonics requires a medium without inversion symmetry, and of course an atomic gas cannot have any such asymmetry.

Over the last several years, HHG has progressed from a novel nonlinear process to a robust table-top source of high energy photons. A key part of this progress was a development of the theoretical understanding of the process. The next section of this paper is dedicated to reviewing the pertinent theoretical models that have aided in understanding HHG.

In the early 1990's, the efforts of several groups, most notably Krause, Schafer, and Kulander [10] and Corkum [11], produced a semiclassical description of HHG known colloquially as the three step model. Several adaptations of this model have been demonstrated [13], but all have the same underlying features. These features are shown schematically in Figure 2.3. The three step model describes how the electron is first ionized by the laser field, then the electron is accelerated by the electric field of the

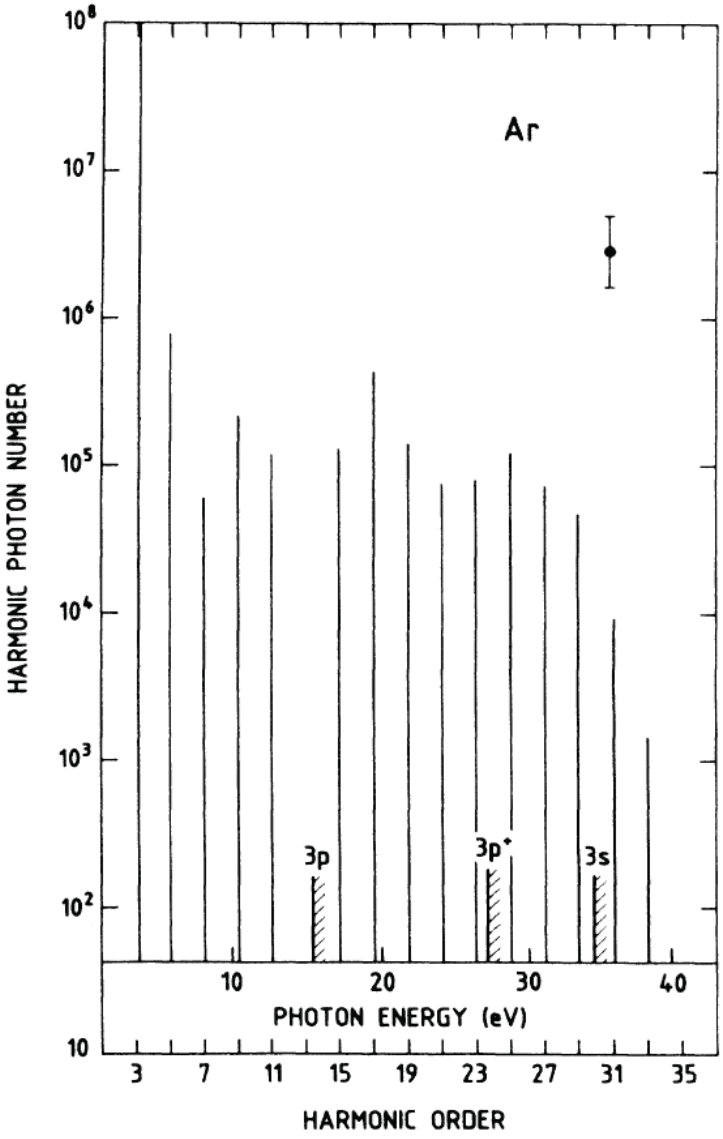

Figure 2.2: Typical HHG spectrum of Ar gas as seen in Li et al. [9] Notice the steady decrease in intensity in the first few harmonics, followed by the plateau region and eventually the cutoff near the 33rd harmonic. The plateau and cutoff are typical for HHG spectra. Li et als experiment focused 1064 nm light from a 10 Hz, 36 ps pulsed Nd:YAG laser into a 15 Torr gas jet. Also shown are various ionization energies for argon.

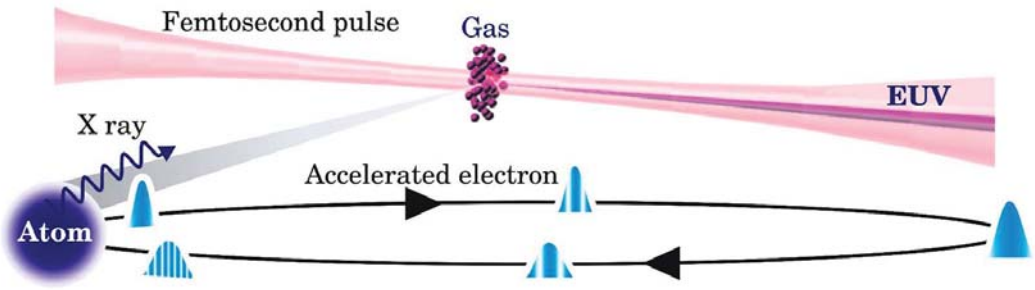

Figure 2.3: Pictoral representation of the three step model [10,11] of how the electron is ionized and accelerated by the fundamental intense, femtosecond laser beam and then is recombined with the atom, producing EUV and soft x-ray light as shown in Kapteyn, Murnane, and Christov [12]. The cycle shown represents one half cycle of the driving electric field. The fringes in the electron wave packet show its evolution throughout the trajectory.

laser, and finally it recombines with the ion producing a high energy photon. The highest photon energy is accurately described by the cutoff law first suggested by Krause, Schafer, and Kulander and further explained by Corkum. This energy is given by

$$E_{max} = \hbar\omega_{max} = I_p + 3.17U_p \tag{2.4}$$

where $\hbar$ is Planck's constant divided by 2π, E_{max} is the highest photon frequency produced by the HHG process, I_p is the ionization potential of the most weakly bound electron, and U_p is the ponderomotive energy of the electron in the oscillating electric field. The ponderomotive energy, which is the average kinetic energy of an electron in a sinusoidal electric field, is given by

$$U_p = \frac{e^2E^2}{4m_e\omega_0^2} = 9.33 \times 10^{14} eV * I\lambda^2 \tag{2.5}$$

where e is the electron charge, E is the magnitude of the maximum electric field of the laser, m is the mass of the electron, ω_0 is the laser frequency, I is the maximum laser intensity, and λ is the laser wavelength. Thus, we see that the maximum photon energy (or shortest wavelength) is propotional to the peak laser intensity I and to the squared driving wavelength, λ^2. The discussion that follows will briefly review the three step model and cutoff law as they apply to HHG.

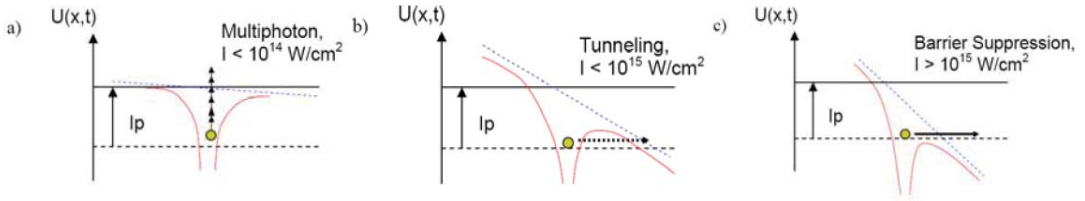

Figure 2.4: Different photoionization processes of extreme nonlinear optics dependent upon the driving laser intensity: a) multiphoton absorption ionization, b) tunneling ionization, and c) barrier suppression ionization. The red line corresponds to the Coulomb potential suppressed by the laser field. Adapted from reference [13].

2.3.1.1 Step 1: Ionization

The first step in the model occurs when the electric field of the driving laser is sufficient to ionize the target atom. The process behind the ionization differs depending upon the peak laser intensity, as shown in Figure 2.4. The first type of ionization described earlier is multiphoton ionization, including ATI. In this process, several driving laser photons, typically with wavelengths of $0.8 - 1.06\ \mu m$, are absorbed simultaneously, thus giving the electrons enough kinetic energy to escape the binding Coulomb potential. Multiphoton ionization occurs at peak intensities below $10^{14}\ W/cm^2$ for these wavelengths. As the laser intensity increases, the Coulomb potential becomes more and more distorted until only a narrow barrier prevents the electron from being released. At this point, the electrons tunnel through the distorted barrier as shown in Figure 2.4. Finally, if the laser field strength is large enough, the Coulomb barrier will be sufficiently suppressed such that the electron can escape over it. This process is known as barrier suppression ionization (BSI) and occurs at peak intensities above $10^{15}\ W/cm^2$ where the peak electric field of the laser exceeds the atomic binding electric field of about 10^{10} V/m. However, BSI usually only occurs for the shortest of laser pulses (~ 5 fs) because longer length pulses will cause the electron to tunnel out before the intensity reaches the level needed for BSI. The Keldysh parameter is the common yardstick used to determine which of these various ionization processes occurs [78]. The Keldysh parameter, γ, is

given by

$$\gamma = \frac{\omega\sqrt{2mI_p}}{eE} \tag{2.6}$$

where e is the electron charge, E is the magnitude of the peak electric field of the laser, m is the mass of the electron, ω is the laser frequency, and I_p is the ionization potential of the valence electron. This parameter can be understood as the laser frequency times the approximate tunneling time. When $\gamma < 1$, the electron most likely undergoes barrier suppression ionization. If $\gamma > 1$, then the electron most likely is ionized through tunneling. Accordingly, the nonperturbative nonlinear optics regime can be classified as the regime where $\gamma \ll 1$ [13]. A more accurate way of determining the ponderomotive energy to be used in the cutoff energy estimates (Equation 2.4) is to use the laser intensity at which ionization occurs based on the tunneling ionization rates [14]. These rates are determined from a quantum mechanical calculation by Ammosov, Delone, and Krainov and are known as the ADK rates [79]. From these rates we can calculate the number of atoms that have been ionized and thus determine how many electron-ion pairs can produce EUV light through HHG after being accelerated and recombining.

2.3.1.2 Step 2: Electron Acceleration

After ionization, the next step in the three step model is the propagation of the free electron in the driving laser field. The assumption that the electron is free after ionization is justified because outside of the atomic potential, the laser field is much greater than the Coulomb potential. Corkum [11] explains that classically the electron moves according to the equations of motion given by

$$x = x_0 \cos\omega t + v_0 t + x_0 \tag{2.7}$$

and

$$v_x = v_0 \sin\omega t + v_0 \tag{2.8}$$

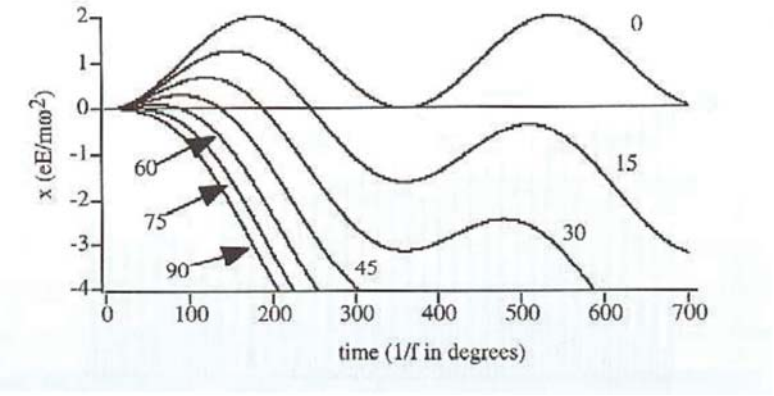

Figure 2.5: One dimensional electron trajectories of freed electrons after tunneling for various initial laser field phases. An initial phase of zero corresponds to the electron being released at the peak of the driving laser field. Notice that for initial phases greater than 90 degrees, the electron never returns to the parent ion ($x = 0$). These trajectories are given by the classical equations of motion (Equations 2.7 and 2.8) [14].

where ω is the laser frequency, x_0 is the initial displacement of the electron from the ion, and v_0 is the initial velocity of the electron after tunneling. Depending upon when the electron is freed from the atomic potential by tunneling, these equations might be modified by a phase shift due to the relative phase of the driving laser. The initial phase of the released electron with respect to the driving laser field will determine the value of the initial velocity and the phase of the oscillating portions of equations 2.7 and 2.8. These equations, in turn, will determine the velocity of the electron upon returning to the vicinity of the parent ion. This return velocity will determine the value of the kinetic energy which the electron will be able to give up in addition to the ionization potential when the electron recombines with the parent ion. This energy is released as a high harmonic photon.

2.3.1.3 Step 3: Recombination

The final step of the three step model is recombination of the propagating free electron with the parent ion. The electron has gained kinetic energy while being accelerated by the driving laser field. As the field direction reverses, the electron is accelerated

toward the parent ion. For linearly polarized light, the electron will return to the vicinity of the ion and can recombine, giving up its energy as a high energy photon. Thus, the energy of the photon is given by the ionization potential of the atom plus the kinetic energy of the electron represented by the ponderomotive energy term in Equation 2.4.

As shown in equations 2.7 and 2.8, the maximum velocity and kinetic energy of the returning electron will depend upon the phase of the driving laser field at the time the electron escapes. Figure 2.5 shows the one dimensional trajectories of the free electrons according to equation 2.7 for several initial laser field phases [14]. An initial phase of zero corresponds to the electron tunneling at the peak of the driving laser field. Notice that for initial phases greater than 90 degrees the electron never returns to the ion. The kinetic energy of the electron is dependant on its velocity when it recombines, which is given by the slope of the trajectory as it crosses zero. The greatest slope corresponds to an initial phase of 0.3 radians or 17.2 degrees. These are the trajectories that produce the highest harmonics near the cutoff region. For electrons that are released before or after the time corresponding to a phase of 0.3 rad, their return kinetic energy will be less as shown in Figure 2.6 [14]. As can be seen, there is a degeneracy in the return kinetic energy for electrons not released at the peak of the pulse where two different electron trajectories contribute photons of the same energy. Often these trajectories are refered to as long trajectories (which spend more time in the continuum) and the short trajectory (less time in the continuum). The harmonics made up of photons from these trajectories make up the plateau region of the spectrum. Thus, the 3.17 law of the three step model predicts that the maximum photon energy of the harmonics produced will be the sum of the ionization potential and the maximum return kinetic energy. This model uses classical arguments to describe the electron's propagation and the maximum recombination energy with quantum mechanical tunneling. This prediction has been verified by comparison to experimental results [9, 12, 13, 77]. While the three step model is useful for an intuitive understanding of HHG and for estimating

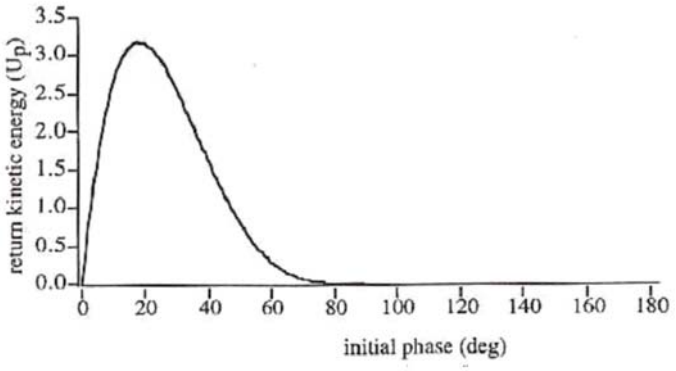

Figure 2.6: Return kinetic energy of the electron in units of ponderomotive energy (U_p) as a function of the phase of the driving laser field (initial phase). A phase of zero degrees corresponds to the electron tunneling at the peak of the laser electric field. The maximum value of return kinetic energy is given by 17.2 degrees and gives a kinetic energy of $3.17U_p$ [14].

the highest photon energies possible, the three step model cannot produce the harmonic peaks of the spectrum. To obtain a more complete understanding of HHG, quantum mechanics must be invoked.

2.3.2 Path integral interpretation of HHG

After the success of the semiclassical three step model, researchers sought to understand the quamtum mechanical aspects of HHG. Nearly all early approaches were based on Krause, Schafer, and Kulander's initial approach [10]. This involved numerically solving the time dependent Schrödinger equation (TDSE) for the electron wavefunction in order to calculate the dipole acceleration. The square of the Fourier transform of the dipole acceleration is proportional to the single atom power radiation. The dipole acceleration is given by

$$a(t) = \frac{d^2 \langle \psi | \mathbf{r} | \psi \rangle}{dt^2} \tag{2.9}$$

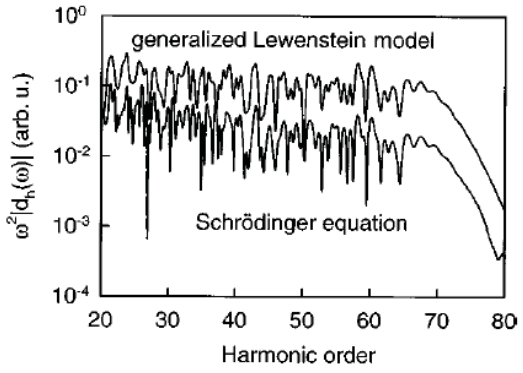

Figure 2.7: Comparison of calculated HHG spectrum using a generalized form of the Lewenstein model and solving the time dependent Schrödinger equation. The Lewenstein model slightly overestimates the dipole strength due to the neglect of the lateral spread of the electron wavefunction as it propagates, thus decreasing the probability of recombination [13].

where $|\psi\rangle$ is the electron eigenfunction of the TDSE. The single atom radiated power is given by

$$P(\omega) = \frac{e^2|a(\omega)|^2}{6\pi\epsilon_0 c^3} \tag{2.10}$$

where e is the electron charge, $a(\omega)$ is the Fourier transform of the dipole acceleration, ϵ_0 is the permittivity of free space, and c is the vacuum speed of light. Most methods involve using a single active electron approximation with various approximations of the Coulomb potential [13]. Since the oscillating electric field is periodic, the HHG process is also periodic, thus leading to discrete energy peaks in the spectrum. This approach, while effective in reproducing experimental results, does not give us an intuitive understanding of the quantum mechanics of the HHG process.

Another quantum mechanical method for calculating a HHG spectrum that is more intuitive is that presented by Lewenstein et al [80]. The spectra produced by the TDSE method and a modified Lewenstein method are compared in Figure 2.7. The important aspects of the Lewenstein model can be summarized in the following equation

for the induced dipole moment $x(t)$:

$$x(t) = i \int_0^t dt' \int d^3\mathbf{p} d^*(\mathbf{p} - \mathbf{A}(t')) E(t') d(\mathbf{p} - \mathbf{A}(t')) e^{-iS(\mathbf{p},t,t')} + c.c. \tag{2.11}$$

where t' is the time of electron ionization, t is the time at which the electron recombines with the atom, $\mathbf{p}$ is the momentum of the electron, $\mathbf{A(t)}$ is the laser vector potential, $E(t)$ is the driving electric field of the laser, $d(\mathbf{p}-\mathbf{A}(t'))$ are the dipole transition matrix elements, and $S(\mathbf{p}, t, t')$ is the classical action integral given by

$$S(\mathbf{p}, t, t') = \int_{t'}^{t} dt'' \left(\frac{[\mathbf{p} - \mathbf{A}(t')]^2}{2} + I_p \right) \tag{2.12}$$

with I_p as the ionization potential. As stated by Lewenstein et al. [80], this formulation has a very satisfying interpretation as a product of probabilities. The $E(t')d(\mathbf{p} - \mathbf{A}(t'))$ term gives the probability of an electron transitioning from a bound state to a continuum state with momentum $\mathbf{p}$ at time t'. The phase of the propagating electron from time t' to time t is represented with the exponential including the classical action integral. Notice that the Coulomb potential is ignored in the classical action due to the fact that the laser field dominates once the electron is ionized. Finally, the $d^*(\mathbf{p} - \mathbf{A}(t'))$ is the dipole transition probability back into the ground state at time t. These probabilities are summed over all paths and all ionization times by the integrals. Therefore, the dipole acceleration that will be Fourier transformed and used in equation 2.10 to give the single atom power spectrum is obtained by taking the second time derivative of $x(t)$ in equation 2.11. As seen from Figure 2.7, the Lewenstein model gives excellent agreement with the TDSE method except for the overestimation of the dipole strength. This overestimation is a result of the neglect of the fact that the electron wavepacket will spread transversely as it propagates, thus reducing the probability of recombination. Several adaptations of the Lewenstein model include the wavepacket spreading as well as other considerations. For details on these adaptations, see Brabec and Krausz [13].

2.3.3 Phase matching

One of the factors limiting the wider application of HHG as a light source is the limited amount of flux. The highest conversion efficiencies reported to date are on the order of 10^{-5} to 10^{-6} [6,12,13]. These efficiencies were obtained though matching of the phase velocity of the fundamental laser fields and the produced harmonic signal. The phase velocity of the light pulses is affected by the different components of the gas target. Neutral atoms in the gas target slow down the optical phase velocity; however, the effect of the plasma is just the opposite. The optical and near-IR phase velocities in the laser pulses speed up in plasmas. When the phases of the laser light and produced harmonics accumulate a phase difference of π, the newly produced SXR radiation destructively interferes with the SXR radiation created from previous cycles. Thus the coherence length over which the HHG process constructively adds is given by

$$L_c = \frac{\pi}{\Delta k} \quad , \quad \Delta k = k_q - qk_0 \tag{2.13}$$

where k_q is the wavevector of the q^{th} order harmonic and Δk is the phase mismatch between the fundamental and harmonic fields. However, if phase matching is achieved ($\Delta k = 0$), the produced harmonic signal increases quadratically with interaction length until the absorption of the harmonics by the neutral gas limits the signal. This is demonstrated in Figure 2.8. Early attempts at phase matching involved adjusting whether the laser focused before or after a gas jet of a noble gas [81]. This allowed researchers to balance the phase mismatch of the neutral gas on the laser field and the Gouy phase shift due to the Gaussian beam focusing. However, the interaction length was limited, so efficient EUV production was not achieved. Later, phase matching by pressure tuning in hollow gas-filled fibers was demonstrated [14, 82, 83]. This technique, by tuning the pressure of the gas in the waveguide, allows the dispersion of the neutral atoms to be balanced with the anomolous dispersion of the plasma. Additionally, this allowed phase matching over longer interaction lengths [12]. Additionally, the SXR radiation from

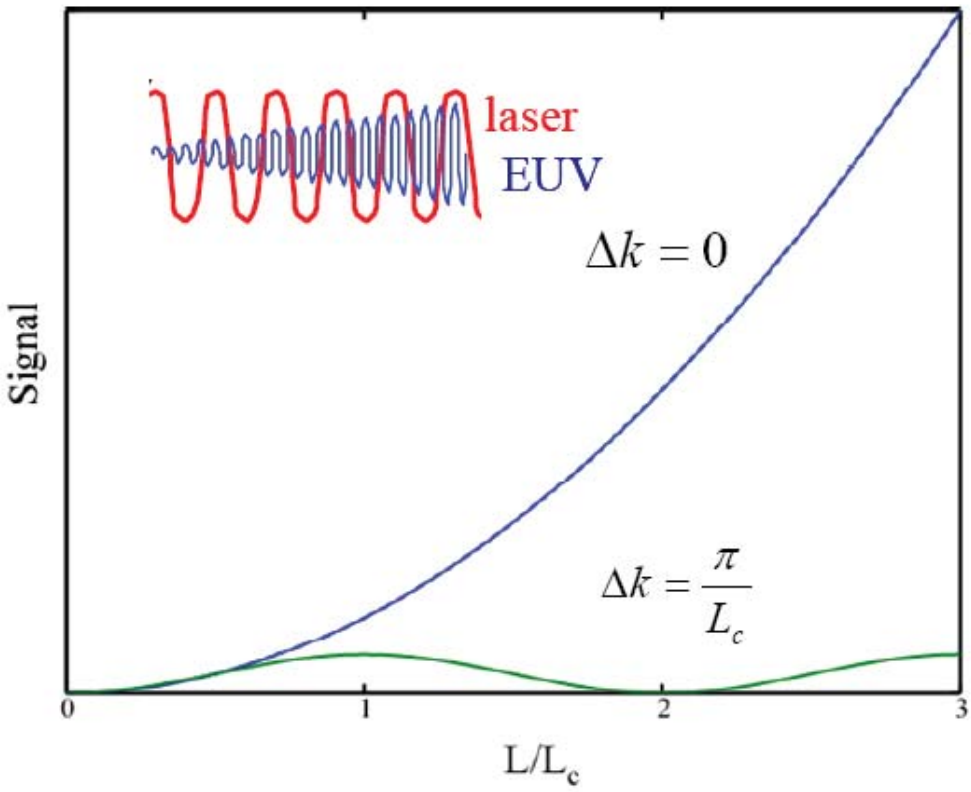

Figure 2.8: As the EUV signal from the harmonics and the laser signal propagate, they will go in and out of phase. The length over which the two remain in phase is called the coherence length, L_c. If phase matching is achieved, the signal will increase quadratically until it is limited by reabsorption of the neutral gas [12].

these fibers exhibits high spatial coherence [17], effectively making HHG a coherent, tunable, femtosecond SXR source. This technique has been shown to produce HHG efficiently (in the 10^{-5} range) for lower photon energies at and below about 50 eV. For higher photon energies, the laser intensity must be increased, which raises the ionization and introduces negative net dispersion of the produced harmonics. This dispersion increases the phase mismatch and prevents efficient harmonic generation above about 80 eV [12]. Above this energy, quasi-phase matching (QPM) techniques are needed. In QPM, the HHG process is effectively shut off periodically after each coherence length. This allows the EUV and fundamental signals to get back into phase and prevents the destructive interference. Periodic poling in nonlinear crystals achieves the same result for lower order harmonic generation [12]. Preliminary QPM has been demonstrated in fibers with periodically modulated inner diameters [84, 85], with counter-propagating beams [62,86,87], and with periodic gas jets [64]. While promising as a technique to enhance shorter wavelength HHG, bright soft x-ray radiation has yet to be demonstrated with quasi-phase matching.

2.4 Coherence and mode quality

This chapter has thus far reviewed the important background and theory of high harmonic generation, but has yet to describe its coherence properties that make it useful as a tabletop source for coherent imaging. This section will describe what coherence

Figure 2.9: Schematic showing high harmonic generation in a hollow fused silica waveguide. When the pressure of the gas inside the waveguide is tuned, the phase velocities between harmonics and driving laser are matched and the harmonic flux builds up coherently. The harmonic beam then has very small divergence (<1 mrad).

means at short wavelengths and why high harmonic light from hollow waveguides exhibits a high level of spatial and temporal coherence.

2.4.1 Definitions of coherence

Coherence is the property of electromagnetic radiation to have a well defined phase relationship either as a function of time or space. Typically, this property can be divided in two directions across an electromagnetic wave [6]. Spatial coherence is the property of an electromagnetic wave to have a well defined phase at two points separated in a direction perpendicular to the propagation of the wave and is closely related to mode quality. Temporal coherence is the property of an electromagnetic wave to have a well defined phase at two points that are separated only in time, or equivalently, two points separated in a direction parallel to propagation. As the topic of coherence at short wavelengths is covered extensively in chapter 8 of Attwood [6] and in section 2.3 of Schlotter [15], the discussion here will be limited to only what is relevant for coherent imaging with tabletop soft x-ray sources.

These two types of coherence are illustrated in Figure 2.10 [6, 15]. Figure 2.10 illustrates the idea of spatial coherence in part (a) and in part (b) it illustrates the idea of temporal coherence. A source with full spatial coherence is a perfect plane wave and therefore all points perpendicular to the direction of propagation will have a well defined phase relationship, namely they will all have the same phase. Since perfect plane waves do not exist, no source exhibits perfect spatial coherence, however a spherical wave far from a point source approaches an ideal plane wave. Therefore, spatial coherence can often be described in terms of source size as is shown in Figure 2.10 (a) (reproduced from Attwood chapter 8.1 [6]). A smaller source will produce a more spherical wave front. As a source increases in size, the phase of the radiated electromagnetic radiation from the individual radiators in the extended source (atoms, electrons, molecules, etc.) can become uncorrelated, thus reducing the coherence of the average radiated wave.

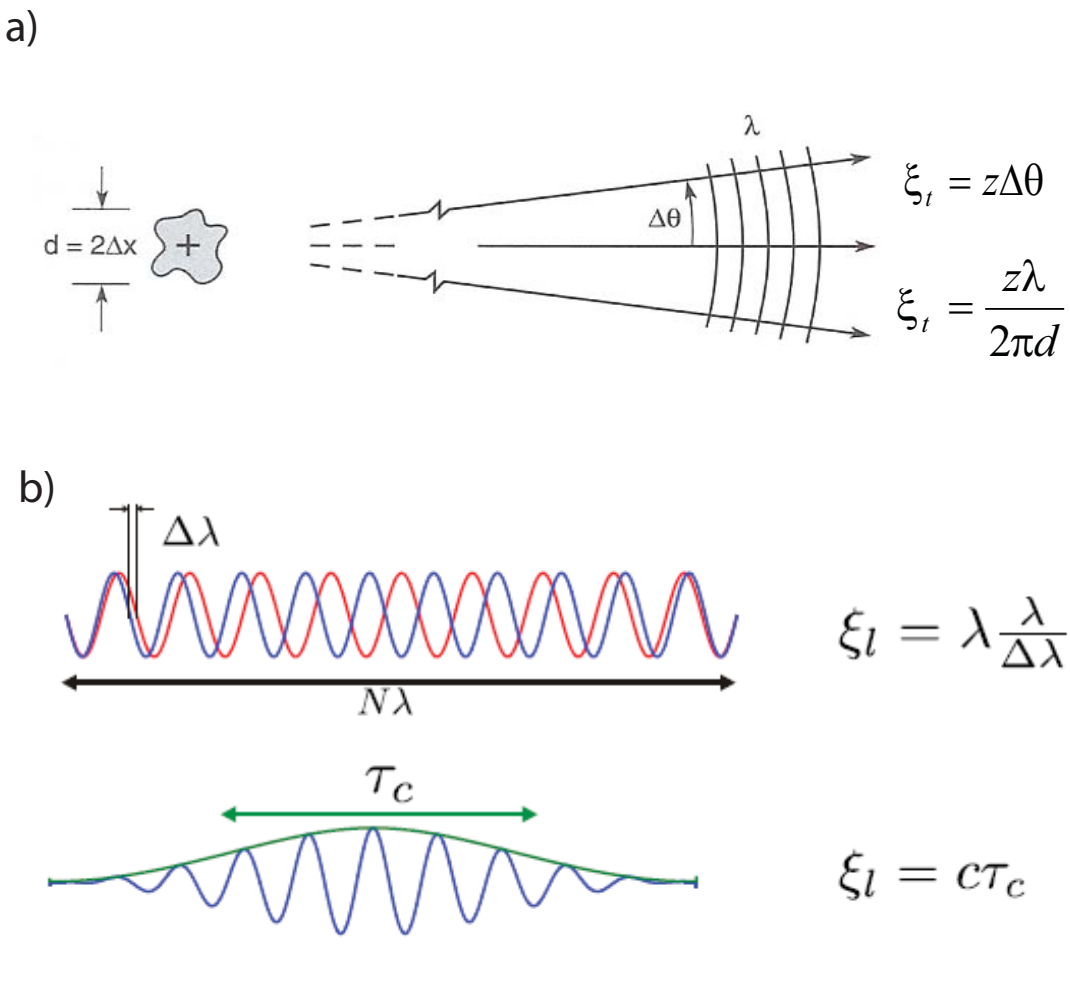

Figure 2.10: Illustration of the two types of coherence: a) spatial coherence is well defined phase travsversely to the wave propagation and can be quantified by the transverse coherence length, ξ_t (from Attwood [6]), temporal coherence is well defined phase along the direction of wave propagation and can be quantified by a longitudinal coherence length, ξ_l (from Schlotter [15]).

The relavant quantity used in describing spatial coherence is the transverse coherence length, ξ_t as given by

$$\xi_t = z\Delta\theta = \frac{z\lambda}{2\pi d} \tag{2.14}$$

where $\Delta\theta$ is the divergence angle of the source, z is the distance from the source (assuming the small angle approximation), λ is the wavelength, and d is the source diameter. This equation as derived by Attwood from the Heisenberg uncertainty principle differs from Schlotter's definition by a factor of $1/2\pi$ [6, 15].

There are multiple ways by which this coherence length can be measured; however, the most commonly used technique is with a wave front interferometer or Young's double slit experiment. This experiment introduces two small pinholes in an otherwise opaque mask some distance z away from a source with divergence angle $\Delta\theta$ and the interfererence from these two pinholes is measured on a distant screen. Once the pinholes are separated by a greater distance than ξ_t, the phase relationship between the two pinholes ceases to be correlated and the interference fringes on the distant screen will lose contrast [6].

While spatial coherence is a measure of the beam quality of a source, temporal coherence is a measure of the temporal bandwidth of the source [6,15]. Temporal coherence describes the phase relationship between two points located parallel or longitudinally along the direction of propagation as is shown in Figure 2.10 (b) from Schlotter [15]. Temporal coherence can be quantified by the longitudinal coherence length, ξ_l, given by

$$\xi_l = \frac{\lambda^2}{\Delta\lambda} \tag{2.15}$$

where λ is the central wavelength of the source and $\Delta\lambda$ is the full width half max (FWHM) bandwidth of the source [15]. Again, there is some ambiguity in this definition as Attwood has an additional factor of $1/2$ in the definition of the longitudinal coherence length [6]. The longitudinal coherence length can be measured with a spectrometer, such as a grating, or by a Mach-Zender or Michelson interferometer [18]. In the case of

an interferometer, the longitudinal coherence length takes on an especially significant description. As additional path length is added to one arm of the interferometer, fringes will appear on the output of the interferometer until the the path length difference exceeds the longitudinal coherence length, ξ_l, at which point the phases of the different wavelengths of light in the source cease to be well correlated. Thus, the definition of longitudinal coherence length given in equation 2.15 is intuitive as the ratio $\lambda/\Delta\lambda$ can be interpreted as the number of wavelengths of path difference over which a source has strong phase coherence longitudinally. This distance can also be thought of in terms of a coherence time, τ_c, as shown in Figure 2.10 [15].

2.4.2 Coherence properties of HHG through phase matching in a hollow waveguide

Now that we have defined what coherence in x-ray sources means, we can explore why phase matched HHG in hollow waveguides exhibits such a high degree of spatial coherence. As mentioned earlier in section 2.3.1, HHG occurs when an electron rescatters with its parent ion under the influence of an intense, ultrafast laser driving field. As described by Bartels and colleagues, since the laser field driving the nonlinear up-conversion is coherent and the HHG process is deterministic classically, it would be expected that the harmonic radiation produced would also be coherent [17]. However, this was not the case until Rundquist and colleaques demonstrated pressure tuned phase matching in hollow waveguides [17, 82]. Before phase matching in hollow waveguides, several groups had studied the coherence properties of high harmonic generation in gas jets [88, 89]. These groups measured limited spatial and temporal coherence of the harmonics due to several macroscopic effects. First of all, since HHG occurs when intense, ultrafast laser pulses ionize a gas target, the index of refraction of the produced plasma forms a negative lens and rapidly varies in time. This rapidly changing index of refraction prevents the coherent buildup of flux and destroys the mode quality of the

harmonic generation process [17]. Furthermore, as was mentioned in section 2.3.1.3, multiple electron trajectories can contribute to each harmonic and these different trajectories tend to have different divergence angles [88, 90]. The longer trajectories have a larger divergence angle and the shorter trajectories a smaller divergence angle. Thus, this effect of multiple trajectories gives the non-phase matched harmonic wavefront a multimodal behavior [17].

Phase matching of the harmonic up-conversion process in a hollow waveguide overcomes these challenges and produces high coherence. Previously it had been shown that when phase matching in a gas jet a single electron quantum trajectory could essentially be selected [81]. This greatly improves the temporal coherence of the source and also the mode quality. Phase matching in a hollow waveguide also selects a narrow range of electron trajectories improving the mode quality and temporal coherence of the source [14,17,82]. Additionally, since the driving laser propagates in a well defined mode of the waveguide, plasma defocusing and index effects are reduced [17]. Thus, the harmonic field from a phase matched hollow waveguide source does take on the coherence effects of the confined laser mode as was shown by Bartels and colleagues [16, 17].

Bartels and colleagues measured the coherence properties of the phase matched high harmonic source from hollow waveguides using a Young's two pinhole setup as shown in Figure 2.11 and as described earlier in section 2.4.1. They showed that the harmonics had a very low divergence angle (<1 mrad) and essentially full spatial coherence as demonstrated in figure 2.12 [17]. In their experiment, two pinholes, each with a diameter of about 40 μm, and with varying distances between them, were placed about 3 m from the exit of a hollow waveguide where the beam was about 1 mm in diameter. The interference of the transmitted light was recorded on a charged-coupled device (CCD) camera about 1 m after the pinholes. The interference in Figure 2.12 shows essentially unity fringe visibility out to about 80% of the diameter of the beam. This suggests essentially full spatial coherence accross the beam diameter. The fact that

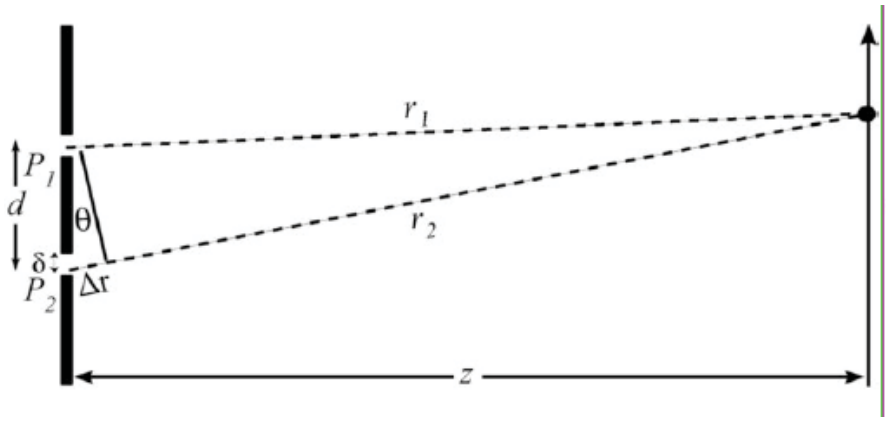

Figure 2.11: Schematic of a Young's double pinhole (wavefront interferometer) used to test spatial coherence from [16].

the finge visibility does wash out at larger separations (400-800 μm) can be attributed to the fact that the phase matched source in argon still produced a comb of about five harmonics centered at about the 19^{th} harmonic (about 30 eV). Let us now analyze the measurement from Bartels *et al* in light of transverse and longitudinal coherence length [17]. In terms of longitudinal coherence length, the authors state that the phase matched beam produces a spectrum with about 4-5 harmonics (17^{th} to 23^{rd} harmonics). This corresponds to a bandwidth, $\Delta\lambda$, of about 12 nm at a central wavelength, λ, of about 40 nm. This ratio, $\lambda/\Delta\lambda$, is about 3.5, suggesting that after 3.5 wavelengths difference in path length (Δr from Figure 2.11) between the two pinholes the interference pattern will wash out. This path difference then exceeds the longitudinal coherence length of $\xi_l = 3.5\lambda = 140$ nm. This would correspond to about three and a half fringes from the central maximum, which agrees well with the number of fringes shown in Figure 2.12. Therefore, any reduction in fringe visibility is most likely due to limited longitudinal coherence length (temporal coherence) not transverse coherence length (spatial coherence).

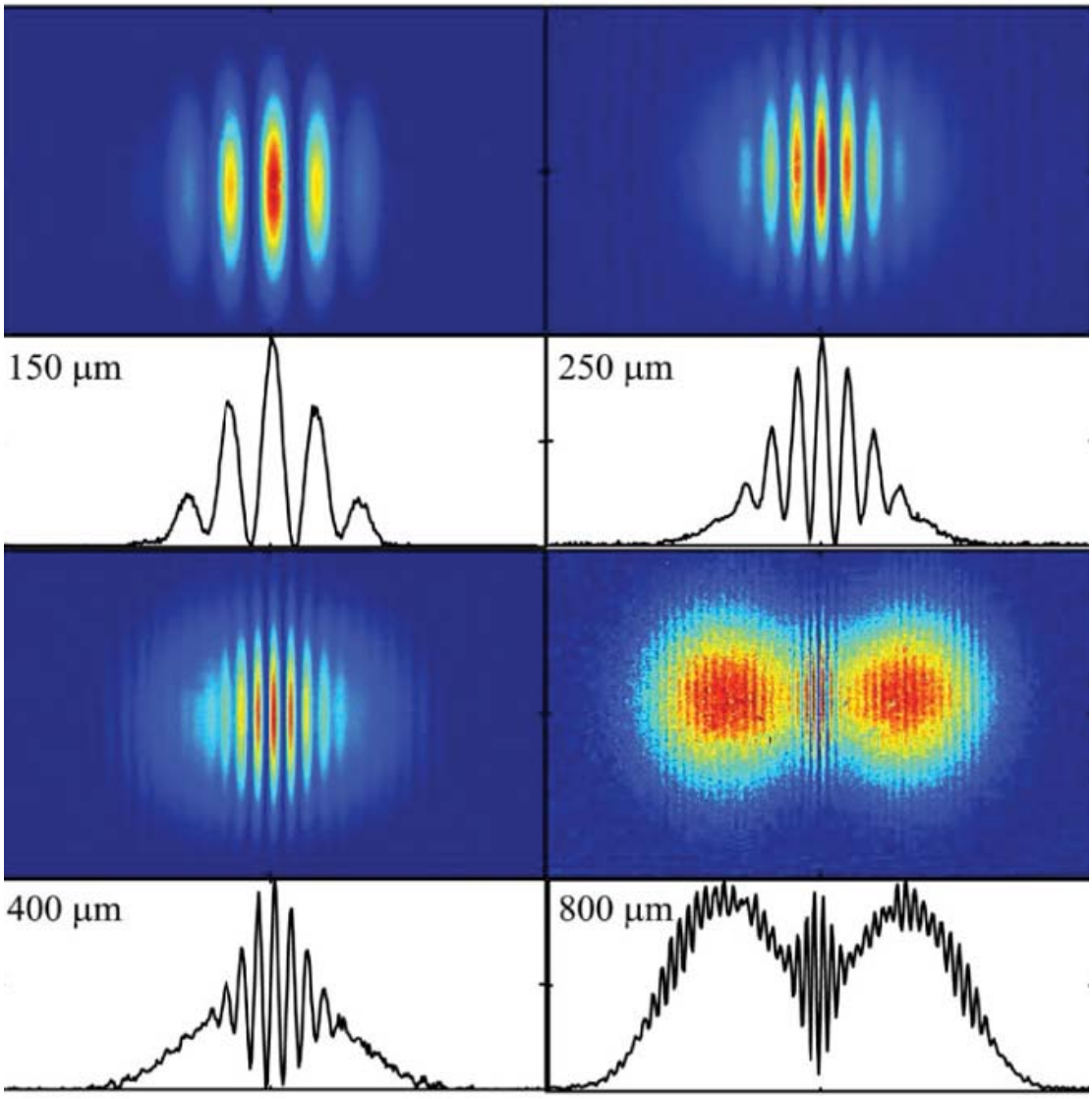

Figure 2.12: Measurement of the coherence of phase matched high harmonic generation from a hollow wave guide reproduced from Bartels *et al* [17]. Measurements were made where the beam diameter was about 1 mm with two pinholes (about 40 μm diameter each) at different separations as shown. Notice the very high fringe visibility out to almost 80% width of the beam.

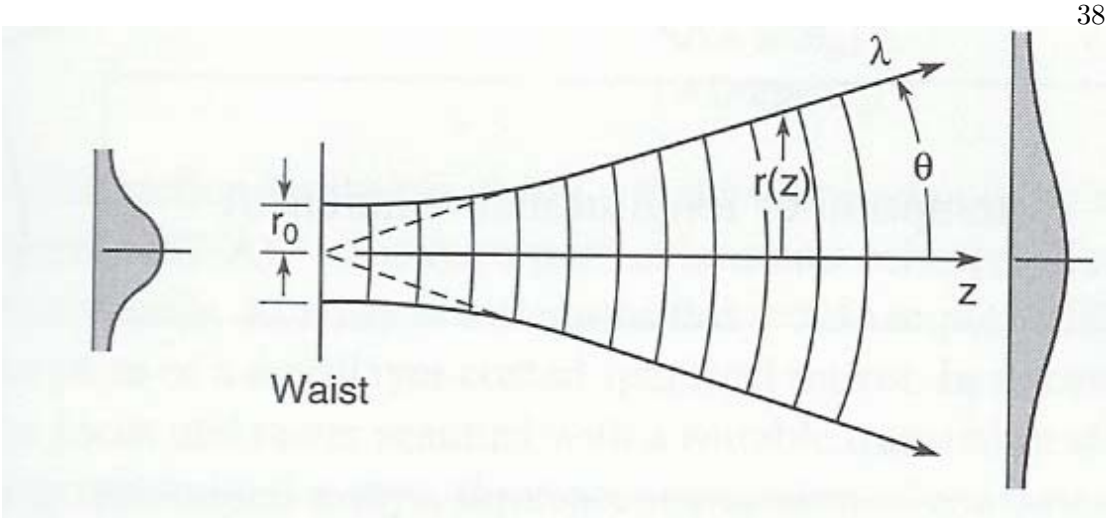

Figure 2.13: Illustration of the phase properties and temporal coherence of a diverging Gaussian beam (from Attwood [6]).

2.4.2.1 Gaussian mode

If we calculate the transverse coherence length according to equation 2.14 with a 40 μm source size with a central wavelength of 40 nm as given by reference [17] and a z distance of 2.85 m, then we get a coherence length of $\sim$ 500 μm (corresponding to a radius). This amount is equal to the divergence angle by the relationship $\theta = r_0/z$, suggesting that the beam is completely coherent spatially. In fact, Attwood describes how for a Gaussian beam, the transverse coherence length is the same as the far field divergence of the beam. This conclusion is logical since a Gaussian beam is the lowest order and simpliest mode in which electromagnetic radiation will naturally propagate as a beam [18]. The far field divergence (and hence transverse coherence length) for a Gaussian beam is shown in Figure 2.13 (reproduced from Attwood [6]). This fact can be shown mathematically as follows [6]. The radius at which the intensity is $1/\sqrt{e}$ the value of the peak intensity of a Guassiam beam, $r(z)$, is given as a function of distance, z, from the smallest radius, r_0, (known as the waist) in

$$r(z) = r_0\sqrt{1 + (\frac{\lambda z}{4\pi r_0^2})^2}. \tag{2.16}$$

If we calculate the far field divergence angle, $\Delta\theta$, (defined as θ in Figure 2.13) far from the waist position (z_0) we obtain

$$\Delta\theta(z \gg z_0) = \frac{r(z)}{z} \cong \frac{\lambda}{4\pi r_0}. \tag{2.17}$$

Finally, if we multiply this value by the distance from the waist (which can be considered a source in this discussion) in order to calculate the far field radius ($1/\sqrt{e}$), we obtain

$$r(z) = z\Delta\theta = \frac{z\lambda}{2\pi d} \tag{2.18}$$

where d is the source diameter ($2r_0$). This result is exactly the same result as the transverse coherence length in equation 2.14. Thus, a Gaussian beam exhibits total transverse (or spatial) coherence.

Because of the foregoing discussion, it might not come as a suprise that a phase matched high harmonic beam from a hollow waveguide will produce a Gaussian beam. The far field beam of the 27^{th} harmonic (29 nm) is shown in Figure 2.4.2.1. This beam was measured on a CCD camera after bouncing off of two multilayer mirrors in a setup that will be described in chapter 4. These mirrors act as a monochromator, effectively selecting a single harmonic. Figure 2.4.2.1 (top) shows the logarithmic Gaussian high harmonic beam which covers almost the full dynamic range of the camera (~ 65000) and (bottom) a Gaussing fit to the verticle lineout of the Gaussian beam showing very good agreement. The true measure of how well a beam matches to a TEM_{00} Gaussian mode is given by measuring a beam's M^2 (M-squared) value which compares the divergence of the beam with the ideal divergence of a Gaussian beam. Measuring the M^2 of our phase matched harmonic beam is a future project that needs to be completed.

2.4.2.2 Temporal coherence of phase matched high harmonic generation

As mentioned earlier, phase matching of the high harmonic process can effectively select effectively a single electron trajectory. The harmonic resulting from this single

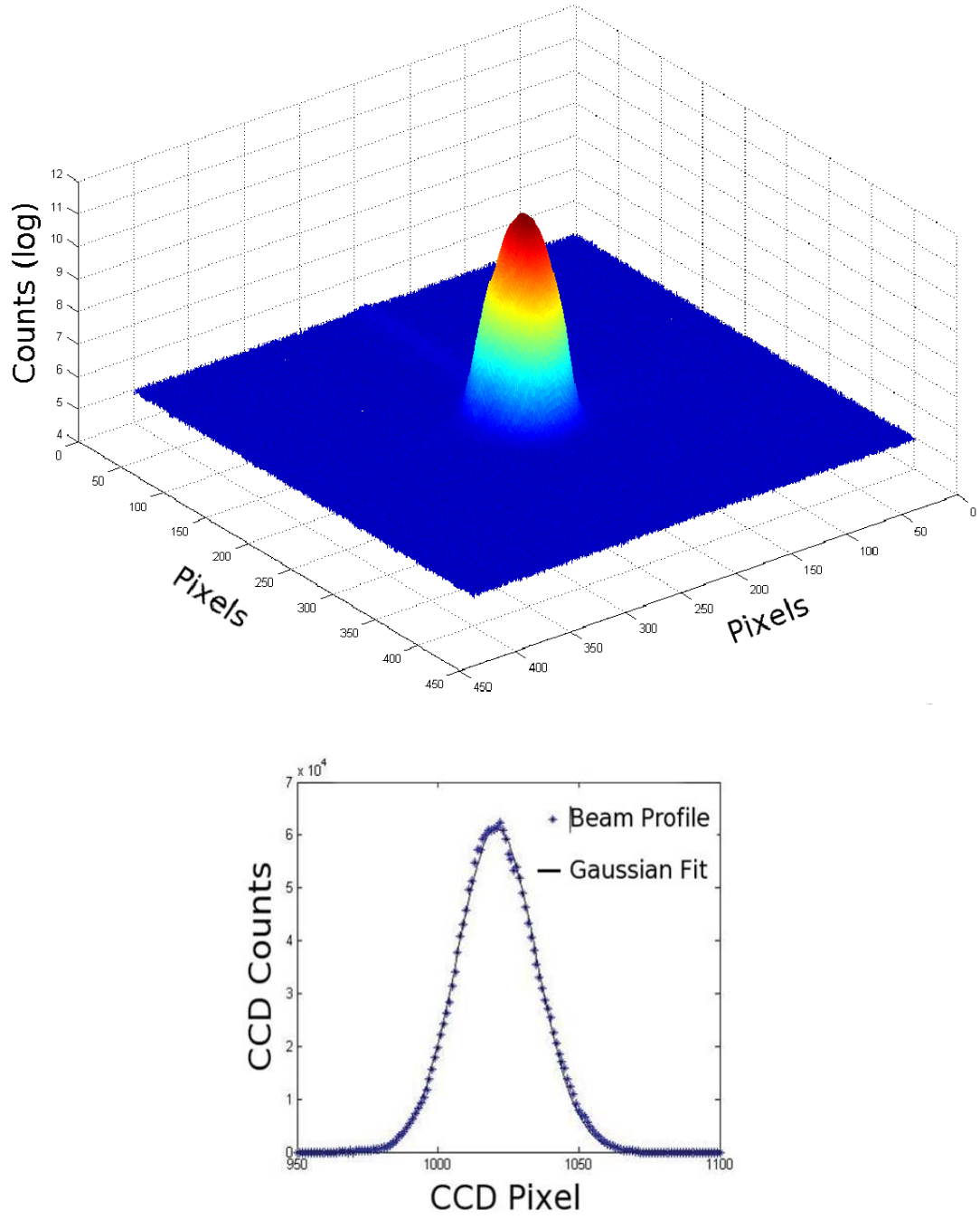

Figure 2.14: (Top) Measured optimized 29 nm mode (log scale) on the CCD after two multilayer mirror reflections. (Bottom) Gaussian fit to horizontal line out of HHG mode showing excellent fit with $R^2 = 0.9986$.

trajectory would be expected to have a very narrow bandwidth and long longitudinal coherence length. However, as we discussed earlier in this section, Bartel's measurement of coherence suggests a $\lambda/\Delta\lambda$ of 3.5. This, however, is due to the fact that their phase matched source was optimized for brightest flux resulting in 4-5 harmonics being phase matched. The individual bandwith of each harmonic may be much narrower than 3.5. Single harmonics can be selected by use of a grating or multilayer mirror monochromator. Such a measurement of a single harmonic produced from a gas jet reports a $\lambda/\Delta\lambda$ of 71 [91]. However, this source is not fully phase matched, thus we might expect a broader bandwidth. Bartels *et al*, in a separate work involving optimization of harmonic generation with pulse shaping measure spectrometer resolution limited bandwidth of the 27^{th} harmonic (29 nm or 42 eV) to be 0.25 eV [92]. This corresponds to a $\lambda/\Delta\lambda$ bandwith of about 170. Subsequent observations in work contributing to this dissertation from diffraction patterns and spectrometers have measured $\lambda/\Delta\lambda \geq 250$ from the 27^{th} harmonic after two bounces from multilayer mirrors which each have a bandpass of about 3.3 eV (or 2.5 nm). Thus, phase matched high harmonic generation can produce truly laser like EUV and SXR radiation with high temporal and spatial coherence. In the next chapter it will be shown why this high coherence is necessary for high resolution coherent imaging.

2.5 Comparison to other tabletop SXR sources

Before moving onto the next chapter, we should briefly overview other tabletop sources of EUV/SXR radiation. We will start with the most incoherent sources and move to progressively more coherent sources. Laser produced plasmas have been shown to be a very bright source of EUV to hard x-ray radiation [6, 74, 93]. These sources operate by focusing a high power ($\sim$ 100 mJ/pulse, nanosecond pulse duration) laser into liquid or solid targets producing hot, dense plasmas [6]. These highly ionized plasma species can then produce atomic line radiation on top of a broad continuum of

Bremsstrahlung radiation. Thus these sources can have very high temporal coherence but low spatial coherence as the radiation is emitted into 4π steradians (sr). One particularly nice example of zone plate imaging with a laser produced plasma comes from Hans Hertz group in Sweden where a 3 ns Nd:YAG laser (100 mJ/pulse, 100 Hz) is focused into a liquid nitrogen jet target. The hydrogen-like liquid nitrogen K_α plasma line produces bright radiation at 2.478 nm which is in the biologically important water window [94]. While this source is extremely bright ($\sim 10^{14}$ photons/s) this is into 4π steradians [94]. The flux on the sample is $\sim 10^6$ photons/$(s \times \mu m^2)$ after a condensor optic (either a multilayer mirror or zone plate). This group demonstrates approximately 30 nm resolution in a five minute exposure, making practical nanometer scale imaging in the water window. While useful for many applications, these spatially incoherent plasma sources are not very tunable as they rely on atomic transitions. Additionally, they have relatively long pulse durations (nanoseconds) making them unsuitable for ultrafast imaging. More information on laser produced plasmas is available in Attwood, chapter 6 [6].

Another attractive source of tabletop EUV/SXR radiation is SXR lasers [6, 95]. These sources are more coherent than laser produced plasmas as they have high gain on highly ionized single atomic transition with spectral bandwidths of up to $\lambda/\Delta\lambda \geq 10^4$ and lower divergence (≤ 10 mrad divergence) [95]. Although they are lasers, their spatial coherence is lower than high harmonic generation sources due to the fact that the lasing action builds up from noise. Thus the extended sources are an ensemble of uncorrelated radiators. These lasers can broadly be classified into two groups: electrical discharge pumping of gas filled capillaries and laser pumped solid targets [6]. The electrically discharged lasers can show essentially full spatial coherence in a gain saturated long capillary [96], high power (~ 1 mW at 1-5 Hz repitition rate) in nanosecond pulses [75], and with both coherent imaging and zone plate imaging have shown wavelength limited resolution (47 nm) [57, 97]. Laser pumped solid target lasers have demonstrated lasing

down to 10.9 nm with Ni-like plasmas of metals (Te, Sn, Cd, Ti), with modest powers (~ 1 μW at 1-5 Hz) in picosecond pulses [98], and have demonstrated 38 nm resolution at 13.9 nm wavelength using zone plates [54]. These sources are very attractive for imaging, interferometry, and even nanopatterning due to their high flux and narrow bandwidth, but they are not tunable, have limited ps temporal resolution, and require a lot of pump energy (GJ of power for electrically discharged lasers). The practicality of scaling these sources to shorter wavelengths is difficult as the pump power necessary goes like $1/\lambda^4$, thus scaling to single wavelength lasers is not practical on tabletop systems [6]. A recent very exciting development with tabletop SXR lasers is seeding of the SXR laser with a high harmonic source [58], thus giving the source the divergence and mode properties of HHG with the spectral bandwidth of an SXR laser. While still limited to wavelengths ~ 10 nm, this source demonstrates unprecedented temporal and spatial coherence with ≤ 1 μW of power, making it an excellent source for tabletop coherent imaging.

2.6 Chapter Summary

With the development of efficient HHG, table-top, coherent, femtosecond EUV sources are available. HHG has developed from first being observed in the late 1980's into an efficient EUV/SXR source through phase matching techniques. The development of the three step model and the use of numerical quantum calculations has aided in explaining the HHG process and predicting how it can be made more efficient. Now, EUV/SXR radiation from HHG is finding applications in spectroscopy, imaging, and perhaps in the future lithographic techniques [6, 12, 13]. Additionally, HHG has made possible the production of isolated sub-femtosecond or attosecond radiation pulses [71–73, 99]. Thus HHG presents a fruitful area for further research and technological development especially in ultrafast coherent imaging.

Chapter 3

Theory of Coherent Diffractive Imaging

3.1 Overview

As mentioned in chapter 1, an attractive alternative to traditional x-ray microscopy involving imaging optics is x-ray coherent diffractive imaging. This rapidly developing technique would greatly benefit from a coherent tabletop source of x-rays, such as high harmonic generation. This chapter will describe the relevant background and theory of x-ray coherent diffractive imaging (XCDI). Specifically, this chapter will describe the oversampling phase retrieval algorithm, including the system requirements and limits of this technique. Additionally, this chapter will describe some recently developed techniques of CDI that will make this technique much more applicable.

3.2 Diffraction Theory

This section will review aspects of scalar diffraction theory important to understanding CDI. We will seek to describe the Fourier relationship between the transmitted electromagnetic wave immediately following an illuminated sample (known as an exit surface wave) with the scattered light (diffraction pattern) on a distant screen. Diffraction is a very common subject of electromagnetic radiation and multiple excellent sources are available on the subject; specifically, Goodman is a seminal work on Fourier optics, diffraction, and diffractive imaging [100]. However, for nostalgic reasons, we will follow the discussion from Peatross and Ware [18]. For brevity, we will begin

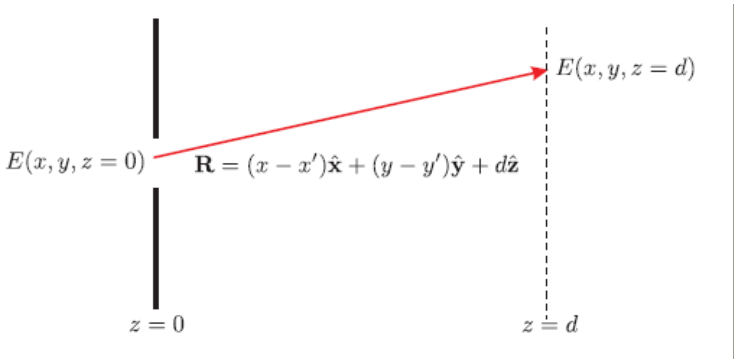

Figure 3.1: Schematic showing the relevant parameters and variables for setting up diffraction theory (from Peatross and Ware [18]).

with the Fresnel-Kirchhoff diffraction formula 3.1. This formula describes the scattered electromagnetic radiation on a distant screen from a sample that is illuminated with a coherent bean as shown in Figure 3.1 [18]. We have made only a few assumptions to this point. Specifically, these are that the aperture or sample size, D, and the distance from the sample to screen, d, are many times larger than the illumination wavelength: $D, d \gg \lambda$. Additionally, we have assumed that the measurements made on the distant screen are in the paraxial approximation, thus the measurement screen is in the forward direction so that the scattering angles are small (see Peatross and Ware chapter 10 [18]). The diffracted electric field distribution, $E(x, y, z = d)$, on the distant screen is given by the Fresnel-Kirchhoff formula

$$E(x, y, z = d) = \frac{-ie^{ikd}e^{\frac{ik}{2d}(x^2+y^2)}}{\lambda d} \int\int E(x', y', 0)e^{\frac{ik}{2d}(x'^2+y'^2)}e^{-\frac{ik}{d}(xx'+yy')}dx'dy' \quad (3.1)$$

where $k = 2\pi/\lambda$, $E(x', y', 0)$ is the coherent illuminating wave, and the integration is over the aperture or sample. The coordinate system is given by coordinates x, y, z with positive z in the direction of beam propagation. The aperture or sample is located at $z = 0$ which we will refer to as the sample plane and the distant screen (or later in this chapter, the CCD) is located at $z = d$, with $d \gg \lambda$, which we will call the detector plane. It should be noted that the two phase factors in front of the integrals are global phase factors that do not affect the intensity. Additionally, we note the quadratic phase

factor, $\frac{ik}{2d}(x'^2 + y'^2)$, in the exponential in the integrand that describes how the pattern evolves as it propagates in z. Equation 3.1 gives the observed diffraction pattern in the detector plane and is said to be in the near field.

All of the measured diffraction patterns in this dissertation were measured in the so called far field of the aperture. The far field diffraction intensity is given by the Fraunhofer diffraction formula. The Fraunhofer diffraction pattern is a simplified version of the Fresnel diffraction pattern, and is described as follows by Peatross and Ware [18]. The Fresnel diffraction pattern is valid everywhere after the aperture as long as the previously described assumptions are satisfied. As the scattered light propagates farther away from the aperture it evolves according to the quadratic phase factor. However, at some point, the diffraction stops evolving and the transverse electric field distribution stays the same except for growing larger proportionally to the distance from the aperture. At the point that the diffraction pattern stops evolving, it is said to be in the far field. The far field distance is given by

$$d \gg \frac{k}{2}(x'^2 + y'^2) \quad \text{so that} \quad e^{\frac{ik}{2d}(x'^2+y'^2)} \approx 1 \tag{3.2}$$

where $x'^2 + y'^2 = D^2$ is the squared aperture or sample diameter, D. Equation 3.2 can be simplified to be expressed only in terms of the aperture or sample to measurement screen distance, d, the wavelength, λ, and the sample diameter, D, as follows:

$$d \gg \frac{\pi D^2}{\lambda}. \tag{3.3}$$

When this condition is satisfied, the diffraction pattern electric field is given by the Fraunhofer diffraction formula

$$E(x, y, z = d) = \frac{-ie^{ikd}e^{\frac{ik}{2d}(x^2+y^2)}}{\lambda d} \int\int E(x', y', 0)e^{-\frac{ik}{d}(xx'+yy')}dx'dy'. \tag{3.4}$$

Several aspects of equation 3.4 are worth noting. First, we note that the Fraunhofer diffraction formula is essentially a two dimensional Fourier transform of the exit

surface wave at the sample plane except for the global phase factors in front of the integrals. Thus, the 'shadow' of the sample and the far field diffraction pattern represent a Fourier conjugate relationship. The coordinates in the far field can be thought of as spatial frequencies with

$$f_x = \frac{x}{z\lambda} \text{ and } f_y = \frac{y}{z\lambda} \tag{3.5}$$

where x, y are the coordinates or characteristic distances in the sample plane [100]. This Fourier relationship is one of the founding principles of XCDI and is ubiquitous in the reconstruction process, usually in the form of the fast Fourier transforms (FFT).

3.3 Sayre and oversampling

Now that we understand the fundamental Fourier relationship between the sample exit surface wave and the far field diffraction pattern, we can discuss the next fundamental building block of XCDI: oversampling of far field diffraction patterns. This idea was presented as a natural extension of x-ray crystallography by David Sayre in 1952 in his seminal work "Some implications of a theorem due to Shannon" [101]. X-ray crystallography has been the primary tool for determining the atomic scale structure of many materials, including many important biomolecules such as DNA [102, 103].

However, many important biological molecules and also whole cells cannot be crystallized easily. Thus, traditional x-ray crystallography techniques cannot easily determine their structure. In 1952, Sayre recognized that, even though a recorded diffraction pattern contains no phase information (only the intensity is measured), if the diffraction pattern is sampled at a sufficient rate the phase information can be extracted [101, 102, 104]. This process can be thought of as solving a set of nonlinearly coupled equations that describe the Fourier relationship between the exit surface wave of a sample and the far field diffraction pattern. Therefore, if we can determine the phase of the electromagnetic wave in the far field, the surface exit wave of the sample can be

determined. If the sample diffraction pattern is sampled at the spatial Nyquist frequency ($f_N = D/z\lambda$ where D is the sample diameter), then the number of unknowns (phases) in the set of coupled nonlinear equations exceeds the number of knowns (amplitudes). However, if the diffraction pattern is sampled at a higher rate than the spatial Nyquist frequency then the set of equations can be solved. This technique is called oversampling.

The oversampling ratio describes the amount of oversampling. In the sample plane, the oversampling ratio can be described as

$$\sigma = \frac{\text{electron density region + no density region}}{\text{electron density region}} \tag{3.6}$$

where $\sigma \geq 2$ [101]. The terminology of electron density comes from x-ray crystallography because the x-rays interact almost exclusively with the atomic electrons (valence to core depending on the energies) through processes of scattering and absorption [6]. Thus, the recovered exit surface wave or sample shadow is related to the sample electron density through Babinet's principle [18]. In the detector plane, the oversampling ratio can be thought of as the number of sampling points in the detection plane per diffraction speckle. In a linear sense for a two dimensional sample, the linear oversampling is given by $O = \sigma^{\frac{1}{2}}$ where

$$O = \frac{1}{pf_D} = \frac{z\lambda}{Dp} \tag{3.7}$$

where f_D is the spatial frequency of the largest sample distance (diameter) D given by equation 3.5, p is the CCD or detector pixel width, and z is the sample to detector distance [105]. Practically speaking, the speckle size on the CCD that corresponds to the spatial frequency f_D is the smallest speckle in the diffraction pattern and is given by the 'spatial period' $1/f_D$ [100].

Now we will present a very insightful empirical derivation of the oversampling theorem from Miao and Sayre [102] which follows closely Ariel Paul's description in chapter 5 of his dissertation [24]. Figure 3.2 also presents the Fourier relationship of oversampling between the sample and detector planes. Typically the diffraction pattern

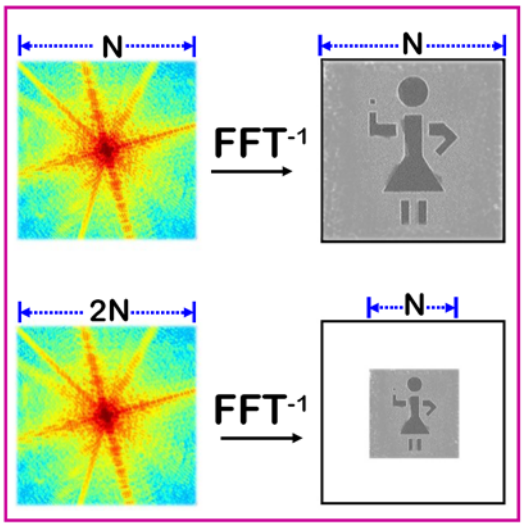

Figure 3.2: An illustration of the no-density region generated by oversampling the diffraction pattern. Here we surround the object with a no-density region where there are no scatters.

is measured on a CCD or other array detector with $N \times N$ sampling points. Because the number of pixels in the reconstructed sample cannot exceed the number of detected points, the sample cannot be sampled at any higher rate than $N \times N$. This is the so called 'conservation of pixels' rule.

The following discussion will present how sampling the far field diffraction pattern is synonymous to surrounding the sample with a no density region. If the electron density of an object is assumed to be $\rho(\mathbf{x})$, then the Fourier transform of this object is given by

$$F(\mathbf{k}) = \mathscr{F}[\rho(\mathbf{x})] = \int_{-\infty}^{\infty} \rho(\mathbf{x}) \exp[2\pi i \mathbf{k} \cdot \mathbf{x}] d\mathbf{x} \tag{3.8}$$

where $\mathbf{x}$ is the three-dimensional spatial coordinate in real space and $\mathbf{k}$ is the three-dimensional frequency coordinate in reciprocal space. If $F(\mathbf{k})$ is sampled at the Nyquist frequency of the object ($f_N = fD = N/D$), then we can replace the continuous Fourier transform is replaced by the discrete Fourier transform

$$F(\mathbf{k}) = \sum_{\mathbf{x}=0}^{N-1} \rho(\mathbf{x}) \exp[2\pi i \mathbf{k} \cdot \mathbf{x}/N], \qquad \mathbf{k} = 0, \ldots, N-1. \tag{3.9}$$

where $\mathbf{x}$ and $\mathbf{k}$ have become discrete and range from 0 to $N-1$ in each dimension. However, if $F(\mathbf{k})$ is sampled at twice the Nyquist frequency, then

$$F(\mathbf{k}) = \sum_{\mathbf{x}=0}^{N-1} \rho(\mathbf{x}) \exp[2\pi i \mathbf{k} \cdot \mathbf{x}/(2N)], \qquad \mathbf{k} = 0, \ldots, 2N-1. \tag{3.10}$$

Let us introduce a new function $g(\mathbf{x})$ such that

$$g(\mathbf{x}) = \begin{cases} \rho(\mathbf{x}) & 0 \leq \mathbf{x} \leq N-1 \\ 0 & N \leq \mathbf{x} \leq 2N-1 \end{cases} \tag{3.11}$$

If $g(\mathbf{x})$ is substituted into Equation 3.10, then

$$F(\mathbf{k}) = \sum_{\mathbf{x}=0}^{2N-1} g(\mathbf{x}) \exp[2\pi i \mathbf{k} \cdot \mathbf{x}/(2N)], \qquad \mathbf{k} = 0, \ldots, 2N-1. \tag{3.12}$$

Equation 3.12 represents the relation between the density function $g(\mathbf{x})$ and its fast-Fourier-transform pattern sampled at the Nyquist frequency of $g(\mathbf{x})$. Thus, oversampling the discrete Fourier transform of the object's density function by sampling more finely than the object's Nyquist frequency generates a no-density region surrounding the electron density of the object as illustrated in Figure 3.2 [102]. Clearly, by the same logic, increasing the degree of oversampling increases the size of this no-density region. Thus, increasing the oversampling rate is increasing the ratio of knowns to unknowns in the set of nonlinear equations from earlier by surrounding the sample with known zero values. This no density region is known as the support and plays a crucial role in the phase retrieval process as we will see next [106].

3.4 Phase Retrieval

Even though Sayre suggested that an image of a sample could be retrieved from the diffraction pattern alone, it took several years to develop practical analytical tools for performing the phase retrieval [102, 104]. Twenty years later, Gerchberg and Saxton proposed the first phase retrieval algorithm based on Sayre's idea [107]. A few years

later Fienup et al improved upon Gerchberg and Saxton's work with two phase retrieval algorithms based on a finite support and a positivity constraint based on the fact that all actual physical samples will have to have a positive amplitude of the complex electron density [106].

Fienup's algorithms, error reduction and input-output, demonstrated that via phase retrieval a complex object can be reconstructed from the magnitude of the Fourier transform (diffraction pattern) alone. Various other algorithms have been developed and demonstrated and two excellent reviews compare and contrast these techniques [19,108]. Most of these algorithms are similar to Fienup's hybrid input-output (HIO) algorithm in their use of a finite support although it should be noted that Marchesini *et al's* 'shrinkwrap' algorithm has proven to be very robust and fast due to the use of a dynamic support [52]. This technique allows the support to periodically update based on an intensity threshold, thus "shrink-wrapping" the sample electron density region. For all the images presented in this dissertation, a genetic algorithm version of Fienup's original hybrid input-output (GHIO) algorithm was used. This technique was developed by our collaborators at University of California at Los Angeles in Professor John Miao's group [20, 47, 109]. The basic HIO algorithm is described in Figure 3.3. The basic aspects of the HIO iterative phase retrieval algorithm are [19, 106]:

1. The square root of the measured diffraction pattern intensity (the amplitude) is seeded with an initial random phase.

2. Each reconstruction iterates back and forth between real and reciprocal space with FFT (or inverse FFT) based on the Fourier relationship between the sample plane and detector plane. In the sample plane (sometimes called real space), two constraints are applied the support constraint and the positivity constraint. For the support constraint, a support is defined as a rectangular area containing the sample, with its size estimated from the linear oversampling ratio as in equation 3.7. The sample density

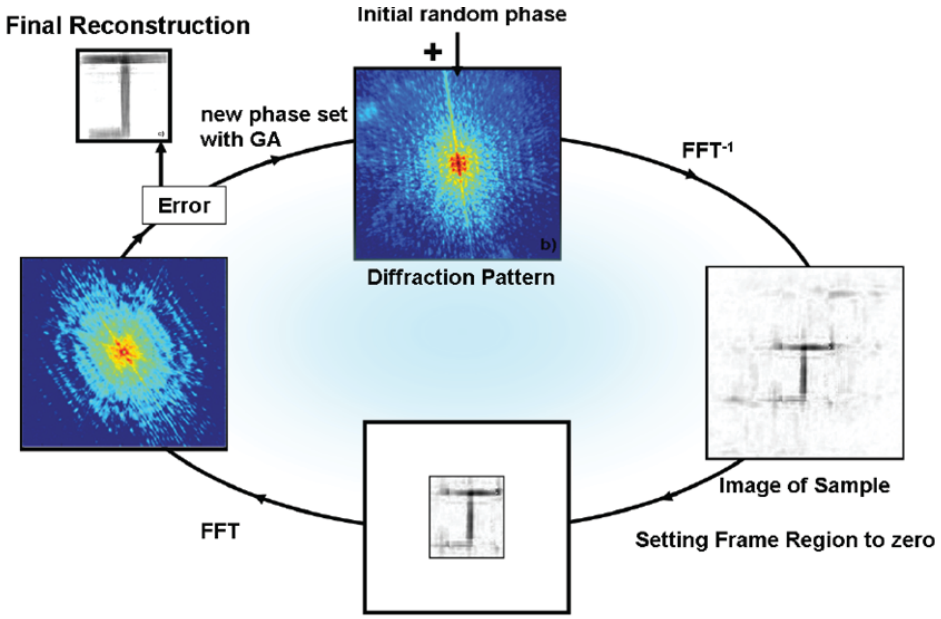

Figure 3.3: Illustration of hybrid input-output (HIO) algorithm from Fienup *et al* [19]. In this dissertation a genetic algorithm version of HIO was used known as guided HIO or GHIO [20].

outside the support and the negative real or imaginary part of the electron density inside the support are slowly pushed to zero (positivity constraint).

3. Next, after applying constraints in the sample plane, the FFT of the sample plane is performed in order to return to the detector plane (or reciprocal space). In the sample plane, the difference between the new magnitude of the FFT and the original measured diffraction pattern amplitude are compared in order to compute an error. Then, the amplitude of the FFT is replaced with the original measured diffraction pattern amplitude (square root of the diffracted intensity) but the phase is allowed to continue onto the next iteration.

4. This iterative process is continued by applying the support and positivity constraint in the sample plane and the amplitude constraint in the detector plane until the phase converges and a faithful high resolution image of the sample plane is reconstructed. This can be achieved by setting a threshold on the error at which point the algorithm is terminated.

Additional techniques can be applied such as running multiple reconstructions on different random phase starts in a genetic algorithm (known as GHIO) or by using a certain number of HIO iterations followed by a number of error reduction iterations [20,108,109]. The GHIO technique will be described in the next chapter in more detail. These phase retrieval techniques can be thought of as the spatial version of the ultrafast pulse measurement technique knows as Frequency Resolved Optical Gating (FROG) [110]. Additionally, it has been shown that these algorithms are very unique in their solutions. It has been shown that multiple solutions are "pathologically rare" and that "in general the 2-D phase retrieval problem will have a unique solution if one exists" [111]. Thus, iterative phase retrieval techniques have proven to be an effective coherent imaging method for oversampled far field diffraction patterns. Effectively an imaging optic is replaced by the iterative phase retrieval algorithm.

3.5 Implementing XCDI

3.5.1 Experimental developments of XCDI

Even though by the mid-1980's the theoretical and computational framework for XCDI existed, it took some fifteen years more until the first demonstration. There are several reasons as to why this delay occurred. First, as personal computers became cheaper and more powerful, they began to appear in ever more laboratories. The phase retrieval techniques discussed in the previous section, when applied to high resolution imaging, are very demanding computationally. Reconstructions can take days on a single processor because often it requires 100,000's of iterations, with each iteration involving two FFT's on array sizes up to several mega pixels. Second, the introduction of third generation synchrotrons with insertion devices such as wigglers and undulators greatly increased the amount of bright, coherent x-ray flux [6].

The first experimental demonstration of x-ray coherent diffractive imaging (or lensless imaging) was performed at Brookhaven National Lab at the National Synchrotron Light Source in the groups of David Sayre and Janos Kirz by John Miao and colleagues [50]. Since this time upwards of 40 groups across the world have pushed the technology and found numerous applications [47]. Perhaps one of the most attractive potential applications is the use of XCDI to image single biomolecules with a single, very intense femtosecond burst of x-rays from a x-ray free electron laser (FEL or fourth generation synchrotron) [51, 112].

Before proceeding, we should note several of the advantages and disadvantages of CDI in light of the phase retrieval algorithms. Several aspects of XCDI make it an extremely elegant and appealing technique. Because lensless imaging only requires illumination with a plane wave, $\sim$ mm accuracy in sample placement is sufficient. No multi-step focusing process is necessary, as is the case for imaging systems that require sample placement and stability at the micron level. With imaging optics, the magnifica-

tion is a purely geometric function of the object to image distance ratio, often requiring the detector to be a meter or more from the imaging optic. In contrast, for tabletop XCDI, the entire imaging apparatus fits in 0.5 m x 1.5 m. It should also be noted that the same experimental setup will work at any wavelength at which narrowband coherent light can be produced.

Additionally, as noted previously, CDI with phase retrieval does not require any imaging optics, which at x-ray wavelengths are lossy, difficult to manufacture, and impose a limited numerical aperture and finite point spread function. Thus, XCDI has the potential to be truly limited only by the wavelength of illuminating light, opening up opportunities for further development and potentially sub-wavelength or super-resolution techniques in analogy to optical wavelengths (see chapter 1). However, some of the disadvantages are the fact that for traditional XCDI image information is only available after significant computer processing and the need for fully coherent sources. Furthermore, for traditional XCDI, only isolated objects can be imaged because of the need for a finite support [19]. We will see in a coming section how this constraint has been overcome with curved beam techniques.

3.5.2 Other CDI techniques

Recently there has been a rush of activity to develop XCDI techniques that do not require a compact support. Of particular interest has been the development of curved beam XCDI techniques that greatly increase the stability and speed of the phase retrieval algorithms and which will allow imaging of extended samples [21, 22]. These techniques use the illumination profile as a support instead of demanding that the sample be finite. This adds a level of complexity by requiring a measurement and reconstruction of the beam using traditional phase retrieval algorithms. This can be achieved by removing the sample altogether. Additionally, these curved beam techniques are a step towards "structured illumination" XCDI techniques that will open various enhancements such

as extended field of view or increased resolution with the same exposure times.

The first technique, Keyhole Diffractive Imaging illuminates the sample with a curved wavefront by placing the sample in the Fresnel regime after the focus of an x-ray lens as shown in Figure 3.4 (b) [22]. Illuminating the sample with a curved wavefront allows for faster and more stable reconstruction of the image via phase retrieval and the ability to zoom in on regions of interest. This technique can be combined with a scanning coherent imaging technique, ptychography, in order to image extended samples efficiently without prior knowledge of the illumination support in Figure 3.4 (a) [21]. For this ptychographic technique, an additional sample plane constraint is added by requiring that the individual exposure regions overlap.

These techniques have faster converging reconstruction algorithms based on the additional phase curvature information on the illuminating beam. They also allow imaging of extended samples; however, they have some disadvantages worth noting. First, they require an optic that can produce a tight focus meaning that zone plates or high NA mirrors are again introduced. Additionally, they require mechanical stability of the beam-sample-detector line below the resolution desired. This is challenging if the goal is to achieve 10 nm resolution. This is a complication that is avoided in traditional XCDI when the sample is overfilled with the illuminating beam. In this case, vibrations are allowed up to the limit of a detector pixel size ($\sim$ 10 μm instead of 10 nm) greatly relaxing this restriction.

In addition to coherent imaging with iterative phase retrieval algorithms, holography has also proven to be capable of high resolution imaging with x-rays. The simplest technique for x-rays is known as Gabor or in-line holography in which a sample is simply illuminated with a coherent beam and the interference between the diffracted light and illuminating beam is recorded in the far field [113, 114]. The phase information is encoded in the interference between these two beams, thus an image can be reconstructed with a single Fourier transform instead of an iterative phase retrieval algorithm.

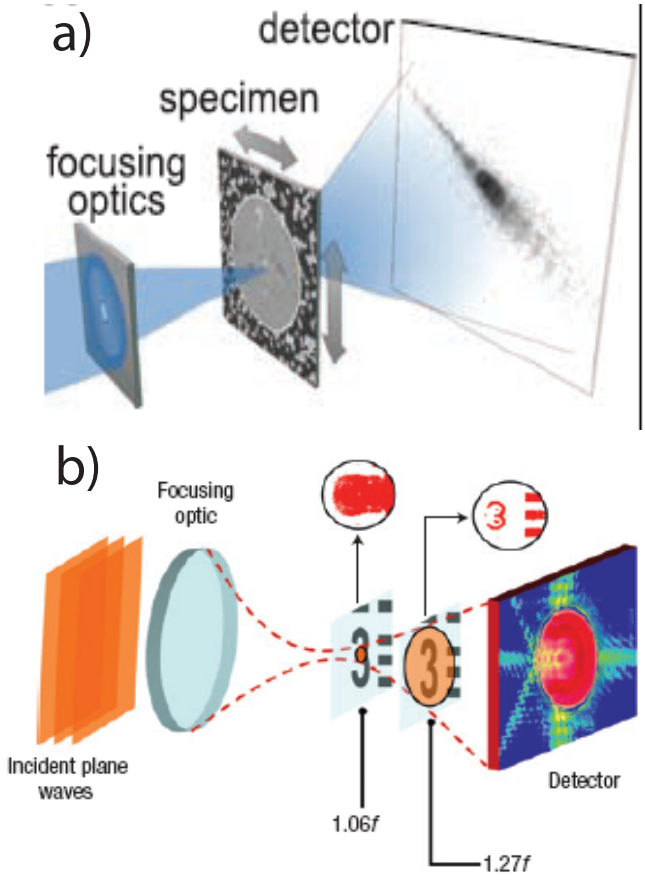

Figure 3.4: Illustration of novel coherent x-ray imaging techniques: a. Ptychography [21]; b. Keyhole Diffractive Imaging or curved wave imaging [22].

The first x-ray coherent imaging demonstrated with tabletop SXR sources was with a HHG source using Gabor holography by Bartels *et al* in the same work in which they demonstrated the spatial coherence of HHG [17]. These intial demonstrations had limited resolution of a few μms. Gabor holography has two notable disadvantages. First, high resolution Gabor holography requires a tightly focused beam in order to achieve good interference at high spatial frequencies. Second, there is a phase ambiguity in the reconstructed image leading to the 'twin image' problem which can cause ringing and distortions in the image [115].

3.6 System requirements

When implementing XCDI experimentally, it is necessary to keep several requirements in mind. This section presents a list of necessary relationships or 'governing equations.' Another treatment of this material can be found in Paul, chapter 5 [24] and in reference [105]. Figure 3.5 shows the relevant setup and parameters for the following discussion.

3.6.1 Geometrical considerations

The two most crucial relationships to consider for CDI are satisfying the requirements of Sayre's oversampling theorem and the phase retrieval algorithms. The oversampling ratio was given earlier in equation 3.7, but is so fundamental to CDI that is is repeated here: $O = z\lambda/pD$ where z, is the sample to detector distance, λ is the wavelength, p is the detector pixel size, and D is the sample size or diameter. Another crucial relation to remember is that the detector needs to be in the far field, so we restate the far field distance from equation 3.3: $z \gg \pi D^2/\lambda$.

The next aspect necessary for CDI is the coherence of the source. As we discussed in section 2.4.1, in order to encode phase information in diffraction patterns through high contrast interference fringes a source must exhibit high spatial and temporal coherence.

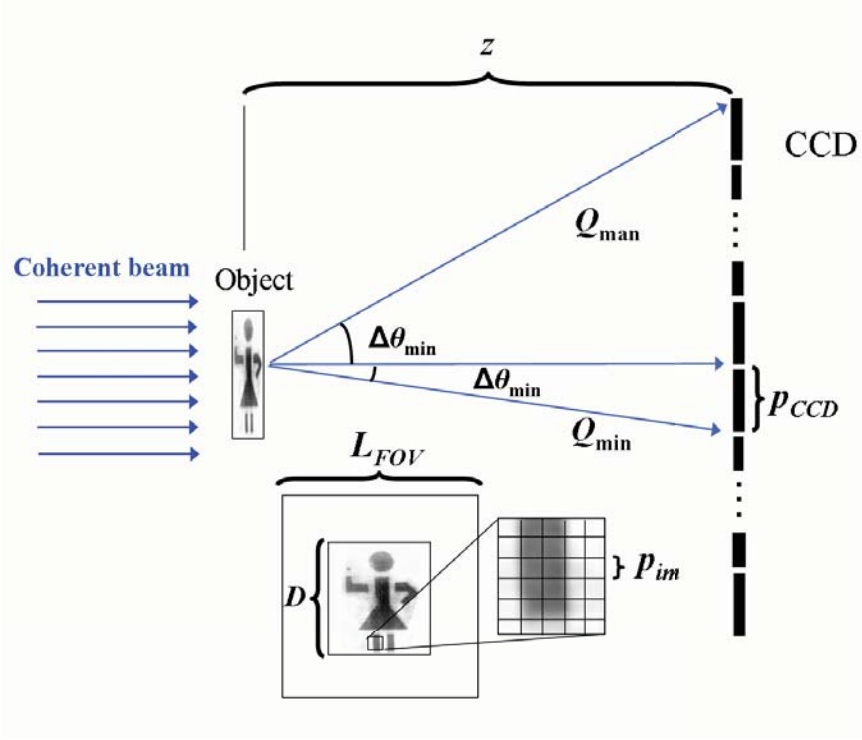

Figure 3.5: Setup of relevant parameters in oversampled coherent diffraction imaging.

As the coherence of the source degrades, these fringes begin to wash out (in the case of degraded spatial coherence) or spread into each other (in the case of degraded temporal coherence). Miao *et al* present empirical relations for how coherent a source needs to be for high resolution CDI [105]. The temporal coherence requirement for CDI is

$$\frac{\lambda}{\Delta\lambda} \geq \frac{OD}{r} \tag{3.13}$$

where as defined before (and shown in Figure 3.5) λ is the central wavelength of the source and $\Delta\lambda$ the bandwidth, O is the oversampling ratio, D is the sample size (diameter), and r is the highest resolution obtainable in the image reconstruction. Thus, we see that the spectral bandwidth places a limit on the image resolution by

$$r \geq \frac{OD}{\lambda/\Delta\lambda}. \tag{3.14}$$

This relation shows that more oversampling has the effect of lessening the spectral bandwidth requirement for lensless imaging.

In terms of longitudinal coherence length, ξ_l, the temporal coherence limit is

$$\xi_l = \frac{\lambda^2}{2\Delta\lambda} \geq \frac{OD\lambda}{2r}. \tag{3.15}$$

Ariel Paul gives a very intuitive and satisfying interpretation of this requirement in terms of path length difference (see chapter 5 in [24]) by using the Bragg diffraction condition, $\lambda = r\sin(\theta)$ (θ is the scattering angle), to replace λ/r with $\sin(\theta)$ as follows

$$\xi_l \geq \frac{OD\sin(\theta)}{2}. \tag{3.16}$$

Paul interprets equation 3.16 in terms of path length difference. Essentially what this requirement states is that the longitudinal coherence length, ξ_l, must be longer than the path difference between any two points that are separated by $O/2$ times larger than the sample size D. Thus, for the minimum oversampling necessary for CDI, this path length difference would arise from points on the opposite sides of the sample.

For spatial coherence, the requirement on transverse coherence length, ξ_t is more easily understood and is simply

$$\xi_t \geq OD \tag{3.17}$$

so that the transverse coherence length is larger than the total area illuminated OD [105]. As pointed out by Miao *et al*, the higher the oversampling, the finer the details of the diffraction pattern that must be faithfully sampled. Thus, higher oversampling allows a source to be less coherent temporally but at the expense that the source must become more coherent spatially.

Several other experimental aspects of XCDI are worth mentioning briefly but are covered in more detail in Ariel Paul's thesis [24]. These include light tightness, stability, and illumination. Since image resolution is achieved by sampling diffraction patterns at high angles where diffraction efficiency is low, the signal to noise ratio of these high spatial frequencies is very important. Thus the enclosure of the detector must be shielded from any stray light and the detector performance must be maximized for low signal detection and read out. Furthermore, the pointing and intensity stability of the source is very important so that a faithful diffraction pattern is recorded. Additionally, the sample should be illuminated with close to a uniform intensity which usually requires somewhat of a large radius of curvature on the beam and flat phase front. Increasing the beam size with respect to the sample size also tends to improve stability.

3.6.2 Data processing and resolution requirements

When setting up a CDI experiment, several factors are important to consider. The geometrical issues discussed previously such as oversampling, far field distance, coherence, etc., will allow an experimental setup that should produce high quality diffraction patterns. However, this alone will not guarantee a successful experiment. As in any imaging experiment, two parameters that are very important to consider are resolution and field of view (here we focus only on two dimensional imaging, but if three dimen-

sional imaging is considered then also depth of focus is an important parameter). With CDI, the resolution and field of view are determined by the Fourier relationship of the scattered light. Typically, this scattering process is quantified by the scattering angle or photon momentum transfer that is imparted to the photons. Figure 3.5 also describes the relevant parameters in this discussion. The momentum transfer, Q, is given by

$$Q = \frac{4\pi \sin(\theta)}{\lambda}. \tag{3.18}$$

where $\sin(\theta) = y/z$ where y is the transverse distance from the no deflection, zero momentum transfer ($Q = 0$) point. Thus the maximum momentum transfer measurable, Q_{max}, corresponds to $y = L/2 = Np/2$ with L being the width of the detector array, N the number of pixels, and p the detector pixel width. The minimum momentum transfer measurable, Q_{min}, is set by the transverse distance $y = p$.

Due to the Fourier relationship between the sample plane and the detector plane, the minimum measurable increment in one will set the largest distance in the other and vice a versa. This can be demonstrated by the fact that the detector pixel size determines the reconstructed image field of view, L_{FOV} by

$$L_{FOV} = 2\frac{2\pi}{Q_{min}} = \frac{\lambda}{\sin(\theta_{min})}. \tag{3.19}$$

If we make the small angle approximation so that $\sin(\theta_{min}) \approx \theta_{min} \approx p/z$, which is generally true for far field detection and appropriate oversampling, then we obtain

$$L_{FOV} = \frac{z\lambda}{p} = 1/f_{min}. \tag{3.20}$$

which we can also equate to the smallest spatial frequency f_{min}. Equation 3.20 can also be used to calculate the reconstructed image pixel size, p_{im}, through the principle of conservation of number of pixels between the detector and image. In this discussion, we will focus on linear pixels (as along one edge of the detector), N. The reconstructed image pixel size is a very important consideration when setting up an experiment, as it must be smaller than any detail of a sample that must be resolved. Therefore, the

absolute limit of an image resolution theoretically, r, with CDI is set by this value, p_{im}. Practically at least two, and preferably many image pixels must be used to resolve this feature so that $r \geq 2p_{im}$. The image pixel size is given by

$$p_{im} = \frac{L_{FOV}}{N} = \frac{z\lambda}{pN}. \tag{3.21}$$

Alternatively, one can calculate $p_{im} = 2\pi/2Q_{max}$ analogously to equation 3.19, where there will be a small discrepancy due to the small angle approximation. Furthermore, from the viewpoint of oversampling ($L_{FOV} = OD$, see 3.5), the image pixel size can be calculated as follows

$$p_{im} = \frac{OD}{N} = \frac{z\lambda D}{pND} = \frac{z\lambda}{pN} \tag{3.22}$$

which is exactly what we calculated in equation 3.21.

Finally, the practical limit on reconstructed image resolution that can be expected is set by the maximum detectable momentum transfer, Q_{max}. The exact value of Q_{max} is difficult to determine, and good signal to noise considerations are important. Bill Schlotter's thesis has a good review of signal to noise in chapter two [15] and in his article in reference [116]. An estimate of highest image resolution (half pitch) possible r_{diff} that is supported by diffraction will be

$$r_{diff} = \frac{2\pi}{Q_{max}} = \frac{\lambda}{2\sin(\theta_{max})} \tag{3.23}$$

where Q_{max} is the maximum detected momentum transfer (with good signal to noise), corresponding to the scattering angle subtended by the angle θ_{max}. We note that this is essentially the same as equation 1.1, except with the prefactor of 1/2 as set by the Abbe resolution criterion. This equation and the ability to calculate the image pixel size, p_{im}, are very useful to remember when analyzing data and determining resolution.

3.6.3 Scalability and limits to resolution set by radiation damage

Earlier, this thesis discussed the possibility that XCDI was capable of producing wavelength limited resolution. This achievement would be extraordinary, especially

since hard x-ray energies like those envisioned at future generation FELs might approach 1 Å or less, making atomic scale resolution possible. While the basic technique of CDI is capable of such resolutions, unfortunately the samples are not unless they are specially prepared. One of the main reasons for this is that both electron microscopy and x-ray microscopy use ionizing radiation, meaning that the energies that atoms or molecules receive when absorbing these particles are higher than at least the binding energies of the atom's valence electrons and often of the core electrons too. Other challenges are resolution dependence on wavelength/photon energy and flux due to scattering efficiency.

The first limit on the scalability of XCDI to atomic resolution is radiation damage. This topic has been studied by many groups along with comparisons to electron microscopy doses [23, 112, 117–119]. Miao points out that it has been widely accepted that at atomic scale resolution a radiation dose of 2×10^7 Gy will cause destruction of protein crystals in protein crystallography (1 Gray = 1 J/kg of absorbed energy) [47]. Marchesini *et al* present a very instructive study of radiation damage and its limits on resolution as shown in Figure 3.6. For illumination with about 1 keV of photon energy, the resolution limit before radiation damage destroys the feature to be resolved is about 5-8 nm in a frozen biological sample [23]. Thus, the radiation damage limited resolution of XCDI with long exposure times is a few nanometers. However, if a sufficient dose of x-rays can be delivered in a few fs pulse (such as from a FEL) it has been shown theoretically that sub-nm resolution may be possible [112, 120]. Neutze *et al* present a study of such a keV FEL pulse and show that radiation damage will manifest itself in about 10 fs [112]. This pulse duration is 1-2 orders of magnitude shorter than what is expected to be available in the first generation of FELs such as the Stanford Linear Coherent Light Source (LCLS).

Finally, it is important, especially for tabletop sources with limited flux, to point out how resolution depends on x-ray dose. Both Shen *et al* and Marchesini *et al* describe

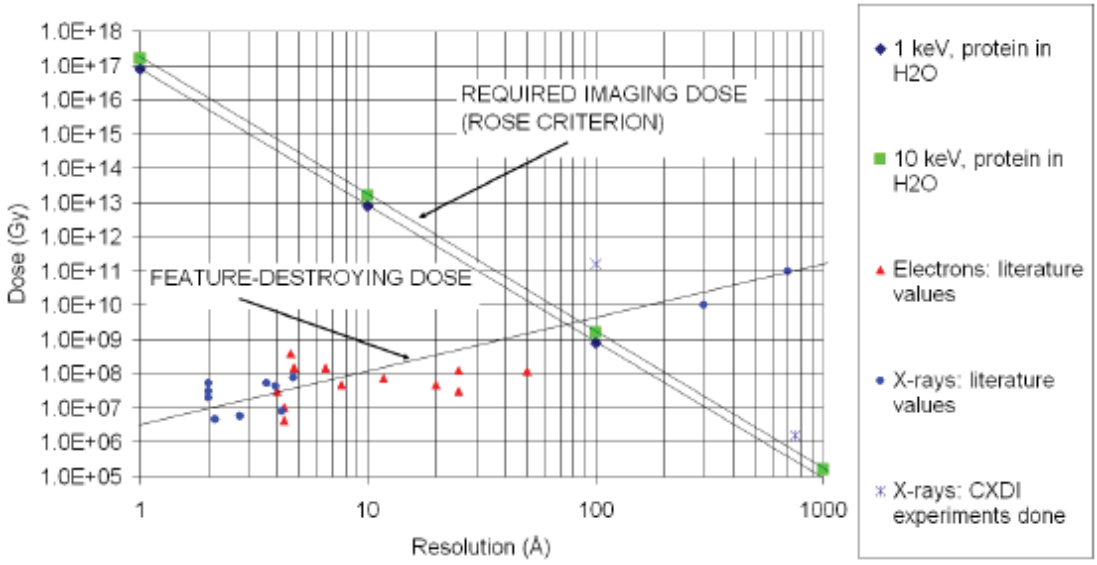

Figure 3.6: Study of radiation dose versus image resolution as a study of radiation damage with electron and x-ray microscopy (from Marchesini *et al* [23]).

how in general resolution scales with photon flux [23,119]. This dependence arises from the dependence of scattering efficiency as a function of spatial frequency or angle, among other parameters. The maximum resolution, r, as a function of incident flux, I_0, is given by

$$r \propto \begin{cases} I_0^{-1/4} & For\ 2D\ imaging \\ I_0^{-1/3} & For\ 3D\ imaging. \end{cases} \tag{3.24}$$

Here we have assumed that the wavelength is fixed. Additionally, Shen *et al* and Marchesini *et al* point out that as photon energies increase from 1-10 keV the absorption and scattering cross sections have a $1/\lambda^2$ dependence. Therefore as wavelengths are decreased in this regime, more flux will be needed to achieve the same spatial resolution. Therefore, most XCDI schemes that are focused on achieving the highest resolution are focusing on the 1 keV range. For shorter wavelengths around EUV and SXR wavelengths this dependence on wavelength will not be the same as there are multiple absorption edges in this region. Therefore, in the EUV/SXR region, resolution will scale more like $r \propto \lambda$ assuming that the scattered flux (not incident flux) is held constant, a difficult assumption to achieve experimentally due to the numerous absorption edges.

3.7 Chapter Summary

In this chapter we have discussed the important theory involved in x-ray coherent diffraction imaging. We reviewed relevant diffraction theory in order to understand how diffraction patterns form a two dimensional Fourier transform of the sample surface exit wave. Next, this chapter reviewed the idea of oversampling and how this idea, in combination with phase retrieval algorithms, provides a powerful technique for x-ray coherent imaging. We reviewed relevant geometric relations important for successfully implementing XCDI. Finally, we discussed the limitations on the resolution attainable.

Chapter 4

First Tabletop Demonstration of Soft X-ray CDI

As was discussed in chapter 3, given the need for coherent illumination, most small-scale EUV/SXR sources are not suitable for lensless imaging. Thus, to-date, lensless imaging has been the sole domain of large x-ray facilities such as synchrotrons or free-electron lasers, where the bright beams can be made coherent by spatial filtering. Recently, the first lensless imaging using a soft x-ray, free electron laser facility at 32 nm was demonstrated. In that work, the high per-pulse energy of the FEL allowed single shot diffraction data to be collected [51]. However, because the sample was destroyed in the process, increasing sample statistics or time-delay measurements on a single sample become difficult. Also, low spatial frequency information about the sample was missing due to a hole in the detector which allows the very intense FEL pulse to pass through without damaging the detector. Since this first demonstration, several other lensless imaging demonstrations have been published, including time resolved images of pump-probe experiments [121–124].

As was shown in chapter 2, high harmonic generation in a gas-filled waveguide generates spatially coherent EUV beams and is ideally suited for lensless imaging [17, 59, 125]. This light source has already been used for Gabor holography with resolution $<$10 μm [17]. Here, we present the first experimental demonstration of high resolution tabletop CDI using a tabletop source of coherent soft-x-rays. Much of this chapter will come from results published in two papers by Sandberg *et al* with invaluable assistance in

the image reconstruction from members of Prof. Janwei Miao's Coherent Imaging Group at UCLA, primarily with the help of Dr. Changyong Song [4,5]. The first of these papers was coauthored with Dr. Ariel Paul, and many specific details of the development and implementation of the experimental setup as well as alignment procedures are discussed in chapter 6 of his dissertation [24].

Section 4.1 discusses the compact XCDI microscope setup. Section 4.2 describes the first CDI results obtained in reflection mode imaging with a few μm resolution as well as necessary changes that needed to occur to achieve high resolution. The first high resolution, $\sim$ 200 nm, images of a thick sample are presented in section 4.3 [4]. Finally, we were able to push the resolution down to 1.5 times the illumination wavelength by going to a high numerical aperture regime and by using a 47 nm tabletop x-ray laser. These results will be presented in section 4.4 [5]. These results thus demonstrate that lensless coherent diffractive imaging can be successfully implemented using tabletop soft x-ray light sources, with broad potential application in nanoimaging and biological imaging.

4.1 Experimental Setup

The setup used for most of the results discussed in this dissertation are shown in Figure 4.1. In our experiment, 1.3 mJ, 25 fs pulses from a titanium doped-sapphire laser amplifier system (KMLabs Dragon^{TM} [8]) are focused with a 50 cm focal length lens into a gas-filled, hollow fused-silica waveguide at intensities of 5×10^{14} W/cm^2. While the waveguide is evacuated, the lens to waveguide distance is varied for maximum power coupling and mode quality. A typical distance from lens to waveguide entrance is typically $\sim$ 60 cm. Phase matching of the conversion process is achieved by pressure tuning the gas as described in chapter 2. In this regime, bright emission over a comb of odd-order harmonics from 25 - 31 is obtained at wavelengths near 30 nm [14, 82, 83]. The hollow waveguide is a 150 μm inner-diameter, 10 cm long fused silica capillary filled

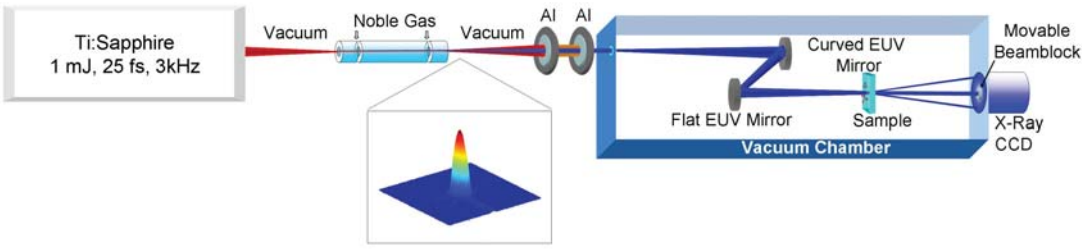

Figure 4.1: Experimental setup for lensless imaging using coherent high harmonic beams at a wavelength of 29 nm. A single harmonic order is selected and focused using a pair of normal-incidence multilayer mirrors. The sample stage is positioned near the focus, where it scatters the soft-x-ray beam onto a CCD. Inset, measured logarithmically scaled soft-x-ray beam profile that is a near-perfect gaussian TEM_{00} over 4 orders of magnitude (see section 2.4.2) [4].

with argon gas at $\sim$ 70 Torr pressure.

4.1.1 Phase matching and coherence optimization

When optimally coupled, an SXR beam is generated with a radius of $\sim$ 25 μm (FWHM) and a divergence of $\Delta\theta < 1$ mrad, giving a transverse coherence length of ξ_t equal to the full beam width and a flux of $\sim 10^{11}$ photons/second. In the initial work described in this chapter, a 10 cm long waveguide was used to insure full spatial coherence of the 29 nm source. However, in later studies it was found that 5 cm long waveguides could be used which increased the flux by about an order of magnitude while still maintaining the mode quality and spatial coherence. More details on the production, characteristics, and geometry of the v-groove waveguide and in addition other experimental details are available in chapter 6 of Dr. Ariel Paul's dissertation [24].

Two 200 nm thick aluminum filters (Lebow Company, Inc.) are used to eliminate the fundamental laser light (one is held in a custom light-tight fixture). A pair of narrowband, molybdemum/silicon multilayer (40 layer pairs, one flat, one with 50 cm ROC) mirrors centered at $\sim$ 29 nm acts as both a monochromator and a condenser, to gently focus the beam onto the sample with a beam waist to about 1.5-2 times the

sample diameter, D. The position of these mirrors is adjusted so as to optimally focus the beam on the sample by using a Gaussian beam propagation model (BeamView). Typical distances are around 1 m from the fiber output to the first mirror, about 10 cm between the mirrors, and about 20-30 cm between the second mirror and the sample. The narrowband mirrors each have a reflectivity of 25% in a 2.5 nm bandpass, to effectively select a single harmonic order. After reflecting from these mirrors, the soft x-ray beam has a narrow bandwidth of $\lambda/\Delta\lambda > 250$, giving a longitudinal coherence $\xi_l = \lambda/\Delta\lambda > 7.3$ μm. The sample is held in an x-y stage controlled by high-precision closed-loop dc motors (Physik Instrumente L.P.). The diffraction of the SXR light from the sample is recorded on a large-area x-ray CCD camera (Andor) with a 2048 x 2048 array of 13.5 μm pixels [126].

The bandwidth of the source is substantially smaller than that set by the mirrors, thus the narrow-band structure of the selected harmonic indicates a very high level of phase matching and the selection of essentially a very narrow band of electron trajectories. While the extent of how narrow this bandwidth can be made still needs to be studied, there are several logical reasons why we could expect it to be this narrow. As was mentioned earlier in section 2.4.2, Bartels *et al* demonstrated a very narrow bandwith ($\lambda/\Delta\lambda = 170$) by optimizing the HHG with shaped laser pulses [92]. We suggest that a similar process is occuring here. When the HHG is optimized prior to inserting a sample into the beam line, the SXR 29 nm mode is viewed on the CCD camera after it has bounced off the two multilayer mirrors. Thus we are already viewing essentially a single harmonic (27^{th}). To optimize the flux, all parameters possible are adjusted to maximize the flux and mode quality. These inlcude driving laser chirp and pulse timing, laser focus into the waveguide, an iris that controls the diameter of the beam before the focusing mirror, the waveguide coupling and pointing, and the gas pressure inside the waveguide. Thus, it is feasible that by adjusting all of these parameters while paying particular attention to the mode, we select essentially a single narrow band of

Figure 4.2: Large (>1 mm) and medium ($\sim$ 0.5 mm) beamblocks used to increase dynamic range of the diffraction patterns [24].

trajectories that produce a single harmonic, phase matched, Gaussian beam.

4.1.2 Beam blocks and alignement

Beam blocks of varying size are placed in the center of the diffraction pattern to block the intense diffraction coming from low spatial frequencies. A large-diameter beam block (>1 mm) allows us to acquire long exposure images to record the highest spatial frequencies diffracted from the sample, while a small beam block (<200 μm diameter) is used to record low spatial frequencies. These diffraction patterns are then stitched together, essentially extending the dynamic range of the camera from 4 to 12 orders of magnitude. These beam blocks are supported by a 12.5 μm wire tethered to a 2-inch diameter mounting ring, held in a kinematic x-y lens translator which allows fine control of the beam block position. For additional information about the beam blocks, see Paul chapter 6 [24].

As was mentioned in chapter 3, a high quality, spatially coherent, uniform soft-x-ray mode is needed for lensless imaging to ensure the sharpest diffraction data. Figure 4.1 (also Figure 2.4.2.1) shows the mode profile of the 29 nm SXR beam, which fits to

a near-perfect Gaussian to the full dynamic range of the camera ($\sim 10^4$). The sample is carefully placed to optimize the illumination, diffraction quality, and oversampling ratio. A flat SXR intensity profile, with a variation less than 10 percent, is required. Overfilling the sample leads to a flatter intensity and also tends to ensure long-term illumination stability, mode quality, and a large radius of curvature of the soft-x-ray beam compared to the aperture size.

The focal spot size, numerical aperture, and oversampling can be adjusted by moving the mirrors and sample stage in z (along the beam axis). The sample also must be placed far enough from the detector to guarantee a far field diffraction pattern, given by $z \geq D^2/\lambda$, where z is the sample to CCD distance, D is the sample diameter, λ is the wavelength. Finally, the distance from the sample to the CCD is chosen to give an appropriate linear oversampling ratio (>5) that allows for easily reconstructable diffraction patterns with high resolution [105]. As described in section 3.6, the linear oversampling ratio relates the smallest diffraction pattern speckles to CCD pixels, and is given by $O = z\lambda/pD$, where p is the pixel size of the CCD camera. For the two images described here ('J' slit and 15 μm Quantifoil), the linear oversampling ratios were $\sim$ 10. In these reconstructed images, each image pixel (not to be confused with a CCD pixel size p), corresponds to a size p_{im} given by $p_{im} = OD/N$, where N is the number of pixels.

4.2 First XCDI Results

While the previous section described the experimental setup used for the majority of the work, this section will briefly discuss an experimental setup and results where the sample was held in reflection mode. This work was never published but has some importance, as two of the applications that will be pursued with tabletop XCDI will be defect inspection of EUV lithography substrates and metrology of EUV lithography optics, both of which will need to be done in reflection mode.

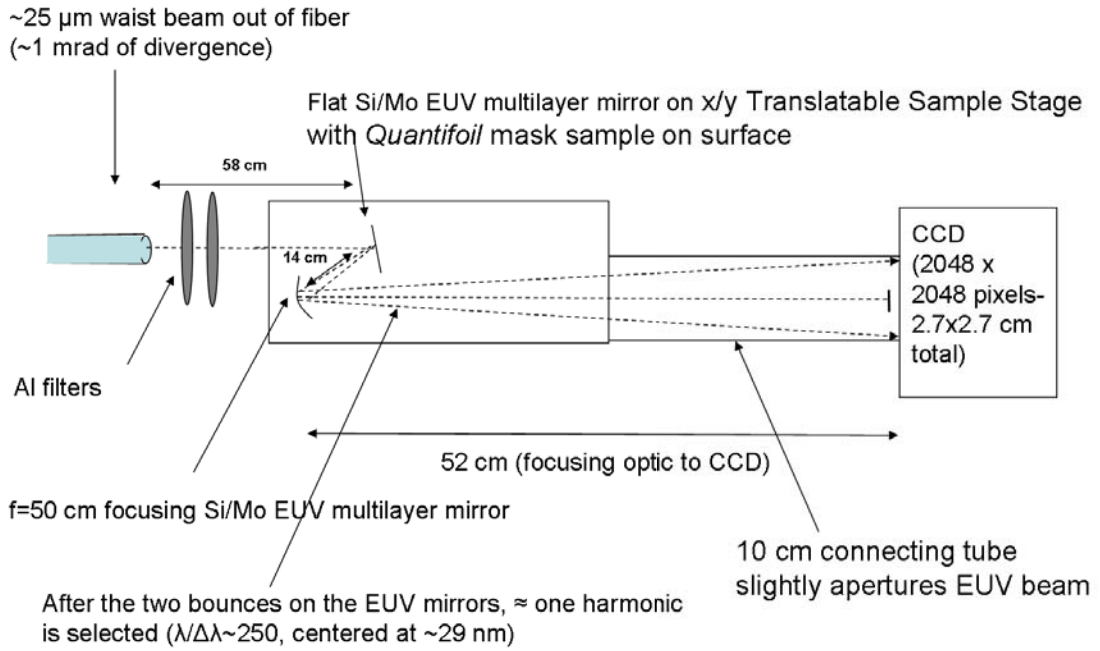

Figure 4.3: Reflection geometry used with previous vacuum chamber for imaging of Quantifoil® on the first Mo/Si mirror.

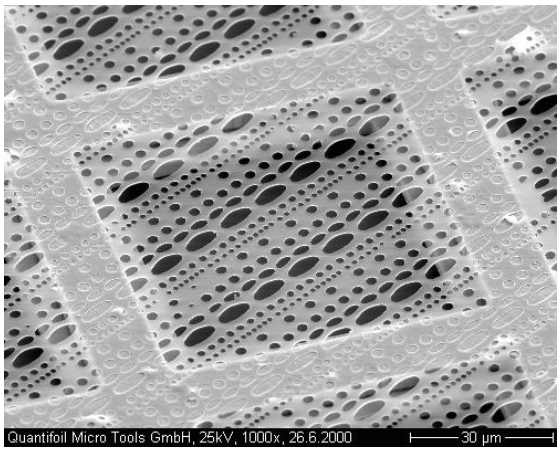

Figure 4.4: SEM image of Quantifoil® "Multi-A" carbon foil [25]. The holey carbon film is about 20 nm thick and rests on a 50 μm picth copper grid with about 10 μm wide gride lines.

Prior to the current "EUV Lensless Imaging Testbed" (ELITE) that was desinged and manufactured by Ariel Paul and Hans Greene (see Paul, chapter 6 [24], we used a smaller vacuum chamber that was large enough for only two Mo/Si mirrors. This setup is shown in Figure 4.3. The reflection geometry setup used the same laser, high harmonic cell, metal filters, and Mo/Si optics as described in the previous section. Thus, we expect the flux and coherence properties of the light to be the same.

4.2.1 Reflection mode results with 150 μm apertured Quantifoil

The sample we used here was a Quantifoil® "Multi-A" carbon foil [25]. The sample consists of a commercially available transmission electron microscopy (TEM) grid that was affixed to a 150 μm pinhole on a thin metal shim. The TEM grid consists of thin 10 μm wide copper grids spaced by about 50 μm (approximately 40 μm x 40 μm open area) with a holey carbon film on top that is approximately 20 nm thick as is shown in Figure 4.4. The pinhole and TEM grid were then affixed to the first (flat) Mo/Si multilayer mirror with the TEM holey film immediately affixed to the mirror. In order to increase the opacity of the TEM film, $\sim$ 100 nm of gold were sputter coated onto the film before it was affixed to the mirror.

The results of the reflection mode imaging are shown in Figure 4.5 with about 1 hour of exposure time. The top pane of Figure 4.5 shows the high spatial frequency data with about 1 hour of exposure with an oversampling ratio of $O = 7.7$. A large beam block (>1 mm diamter) blocks the more intense spatial frequencies and a vacuum tube connecting the chamber and CCD apertures some high spatial frequency data. Additional exposures without the beam block (not shown here) were also taken in order to fill in the missing low spatial frequency data. Figure 4.5 (bottom pane) shows the reconstruction using the GHIO algorithm (to be described later). The basic structure of the Quantifoil can be seen (refer to Figure 4.4), however the grid spacing to pitch ratio of the copper grid seems to be smaller here (perhaps 1/4 or 1/3) compared to

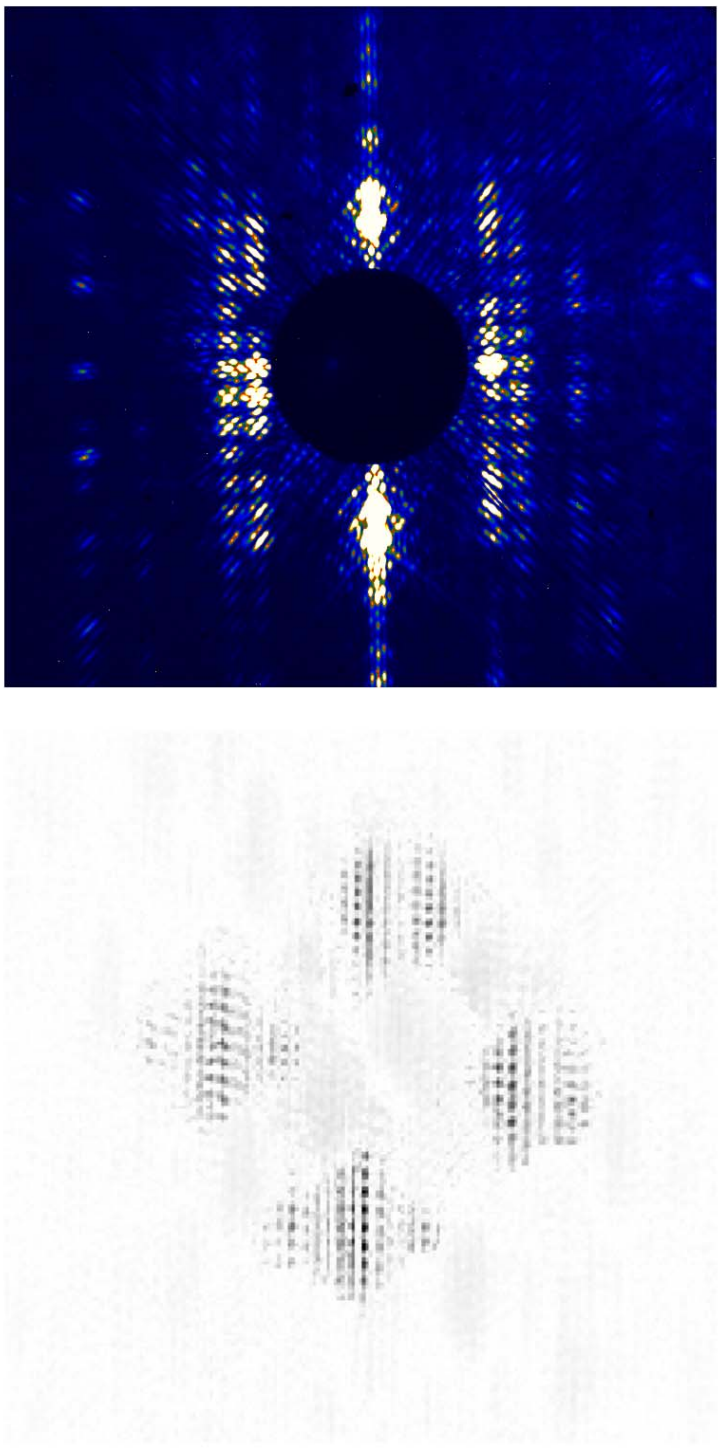

Figure 4.5: A portion of the high spatial frequency data for the reflection geometry on a linear scale (top), the reconstructed image showing some basic features but poor resolution of about 2 μm (bottom) [24].

the sample (1/5). This is probably due to a limiting of the open aperture caused by the sample being held on a mirror at slightly less than normal incidence ($\sim$ 8 degrees). The resolution here is on par with one of the larger holes in the film, so about 2 μm as determined from the highest momentum transfer, Q_{max}.

4.2.2 Improvements

While performing this first demonstration in reflection mode, Ariel Paul and I realized that in order to achieve $\sim$ 100 nm resolution, we needed to get the sample much closer to the camera. This initiated a new design that led to the current ELITE chamber. Additionally, a number of stability improvements were initiated such as floating the optical table in order to reduce vibrations and enclosing the laser beam path in boxes to reduce air currents. These improvements as well as the effect they had on the data are described in Paul chapter 6 [24].

4.3 First High Resolution Tabletop XCDI

After the new ELITE chamber was finished, the experiment was reconfigured into the setup described earlier in section 4.1. With the new setup, we were ready to try a simple transmission sample for demonstration purposes. These results are described in the paper that Ariel Paul and I coauthored with others in *Physical Review Letters*, and much of the text in this section comes from that paper [4] (see also Paul chapter 6 [24]). We used two objects for these experiments: a rectangular "J" aperture with a length of 80 μm, and the same 20 nm thick carbon Quantifoil with holes of various sizes described in section 4.2, placed over a 15 μm diameter aperture in a thin metal film.

4.3.1 Results with "J" slit sample

For the "J" object, the linear oversampling ratio was 9, with a sample to CCD distance z = 33 cm and a sample size D = 80 μm, resulting in an image resolution of

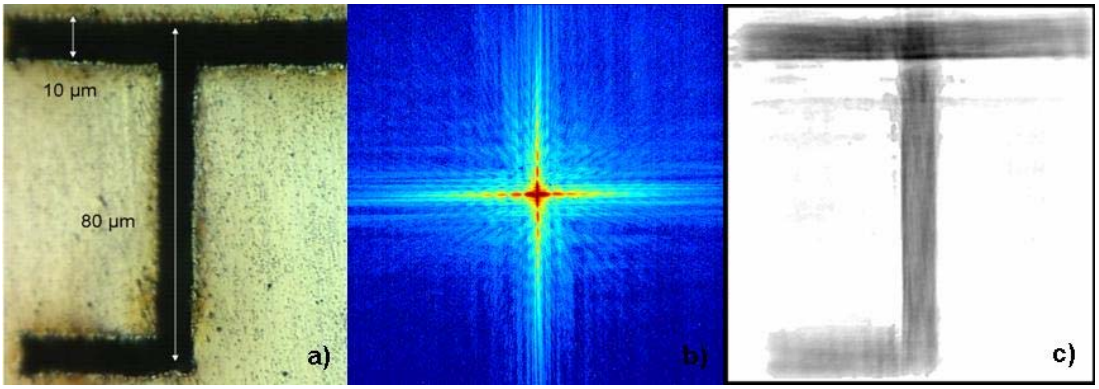

Figure 4.6: (a) Optical image of J-slit. (b) Oversampled diffraction pattern from this sample where the diffraction at the edge of the image corresponds to a momentum transfer of 0.018 nm^{-1}. (c) Magnitude of the reconstructed lensless image. [4]

~ 1 μm. For the carbon TEM film, the linear oversampling ratio was 13, with $z = 9$ cm and $D = 15$ μm. Figure 4.6 (b) shows the coherent diffraction pattern from the "J" slit. Three different diffraction patterns, shown in Figure 4.7, were stitched together to increase the dynamic range, using a 1 minute exposure with no beam block, a 10 minute exposure with a ~ 200 μm beam block, and a 120 minute exposure with a $\sim$ 3 mm beam block. Figure 4.6(c) shows the final image of the 'J' pattern, with each pixel corresponding to 347 nm. The reconstructed image is consistent with the optical microscope image shown in Figure 4.6 (a). However, electron density noise can be seen in this image, arising from long-term instability of the SXR source and the finite spectral bandwidth of $\lambda/\Delta\lambda \sim 250$ at 29 nm combined with the large path differences in the diffraction pattern that arise with this large sample.

To reduce noise in the intensity of the final diffraction patterns, we applied an inverse Fourier transform to the measured intensity to obtain the autocorrelation function of the sample. Since the linear oversampling ratio is $\gg 2$, the autocorrelation function is surrounded by a large region that should have no signal. However, because of camera noise that signal is not exactly zero. We therefore applied a low-pass filter to force this region to be zero. We then numerically integrated the diffraction intensity by binning

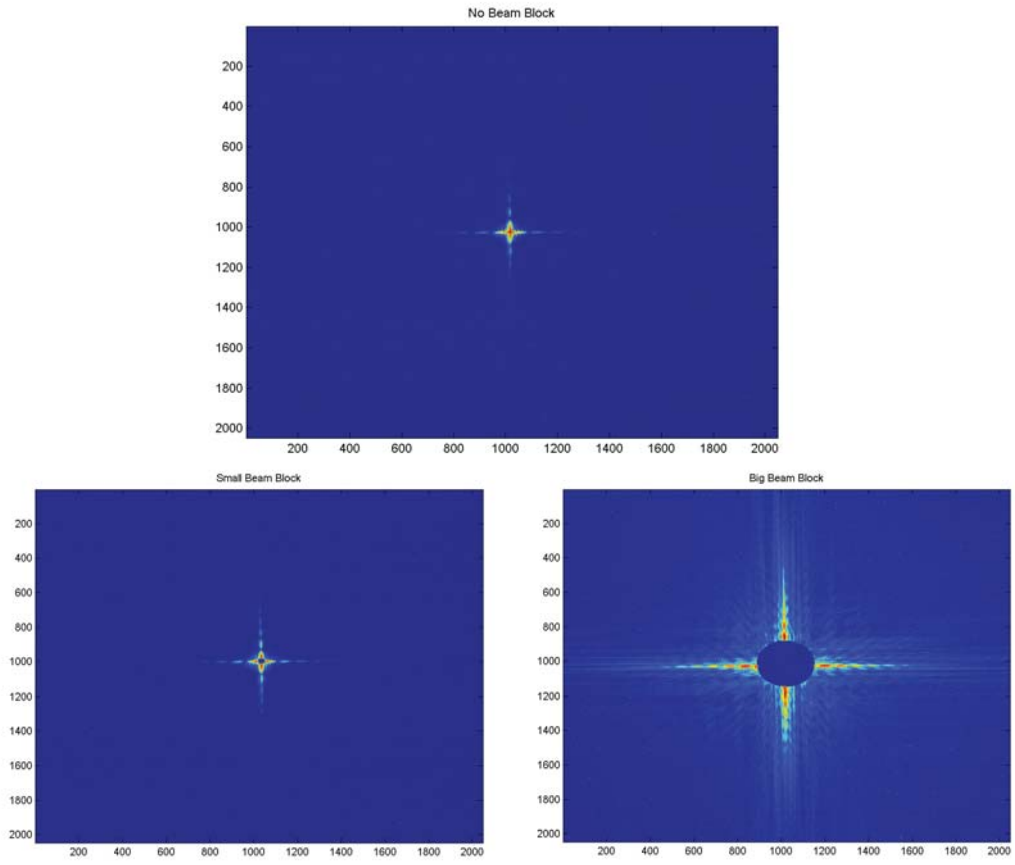

Figure 4.7: Logarithmic raw diffraction patterns from the "J" slit sample: (top) 1 minute exposure with no beam block, (left) 10 minute exposure with a 200 μm beam block, (right) 120 minute exposure with a 3 mm beam block. The figures represent the full area of the camera and have not been cropped.

3×3 pixels into 1 pixel and applying a deconvolution to remove the artifacts in the diffraction pattern due to intensity integration [20]. This step significantly enhanced the signal-to-noise ratio of the coherent diffraction pattern. The analyzed diffraction pattern has a linear oversampling ratio $\sim 1/3$ smaller, and an array size of 680×680 pixels. This also eases the requirement on the temporal coherence by a factor of 3.

4.3.2 Phase retrieval reconstruction using GHIO

Phase retrieval of the coherent diffraction pattern is carried out using the guided hybrid-input-output (GHIO) algorithm (see section 3.4 or references for more details [20, 47, 109]). This algorithm starts with 16 independent reconstructions of the diffraction pattern, where random initial phases are used as the input. Each reconstruction iterates back and forth between real and reciprocal space. In real space, a support is defined as a rectangular area containing the sample, with its size estimated from the linear oversampling ratio. The sample density outside the support and the negative real or imaginary part of the electron density inside the support are slowly pushed to zero. In reciprocal space, the magnitude of the Fourier transform (i.e. square root of the diffraction intensity) remains unchanged, and the phase is updated with each iteration.

After 2000 iterations, 16 images are reconstructed, which is defined as the 0^{th} generation. An error value (magnitude of retrieved amplitude minus measured amplitude divided by measured amplitude) is calculated for each image based on the difference between the measured and calculated magnitude of Fourier transform. The image with the smallest R value is selected as the seed. The inputs for the 1st generation are obtained by multiplying the seed with each of the 16 images and taking the square root of the product. We repeat the procedure for the next generation, and after the 8th generation, the 16 reconstructed images became consistent. From the reconstructed images, we define a tight support that represents the true envelope of the object. Using this tight support, we use another GHIO run to obtain the final reconstructed image. Because

the diffraction pattern is non-centro-symmetric, the electron density of the sample is complex, which in principle makes the phase retrieval more difficult than for real objects. By using a tight support with GHIO, and imposing a positivity constraint on both the real and imaginary parts, we have shown that complex objects can be reliably reconstructed from oversampled diffraction patterns.

4.3.3 Results with 15 μm apertured Quantifoil

A lensless image of the carbon film, apertured to 15 μm, is shown in Figure 4.8. The same beam blocks were used as with the 'J' sample, and exposure times were comparable except for the large beam block data which was about 2 hours. Here we will only present the patched together final diffraction pattern.Figure 4.8(a) is an SEM picture of the sample, while Figure 4.8(b) shows the diffraction pattern. The non-central-symmetry of the diffraction pattern indicates that the sample has absorption and that the sample density is complex. Figure 4.8(c) shows the magnitude of the density for the lensless image, which agrees well with the SEM image. The slight disagreement between the alignment of the holes in the SEM and lensless images is due to parallax. The carbon film and mounting aperture are separated by approximately 56 μm - thus even a few degrees of tilt in the SEM stage slightly alters the parallax and the exact alignment of the smaller holes in the SEM image with respect to the large aperture. A line scan of the reconstructed image indicates that the current tabletop lensless microscope has a resolution of 214 nm.

The parallax of the sample was discovered when one of the reviewers pointed out that the hole patterns in the carbon film between Figure 4.8 (a) and c did not agree. We checked experimentally that the differences between the SEM and x-ray images can be wholly explained by parallax resulting from the different viewing angles of the SEM images. As stated above, the plane of the Quantifoil film and the aperture are separated by some distance (56 m), as is made clear in the different SEM images shown in Figure

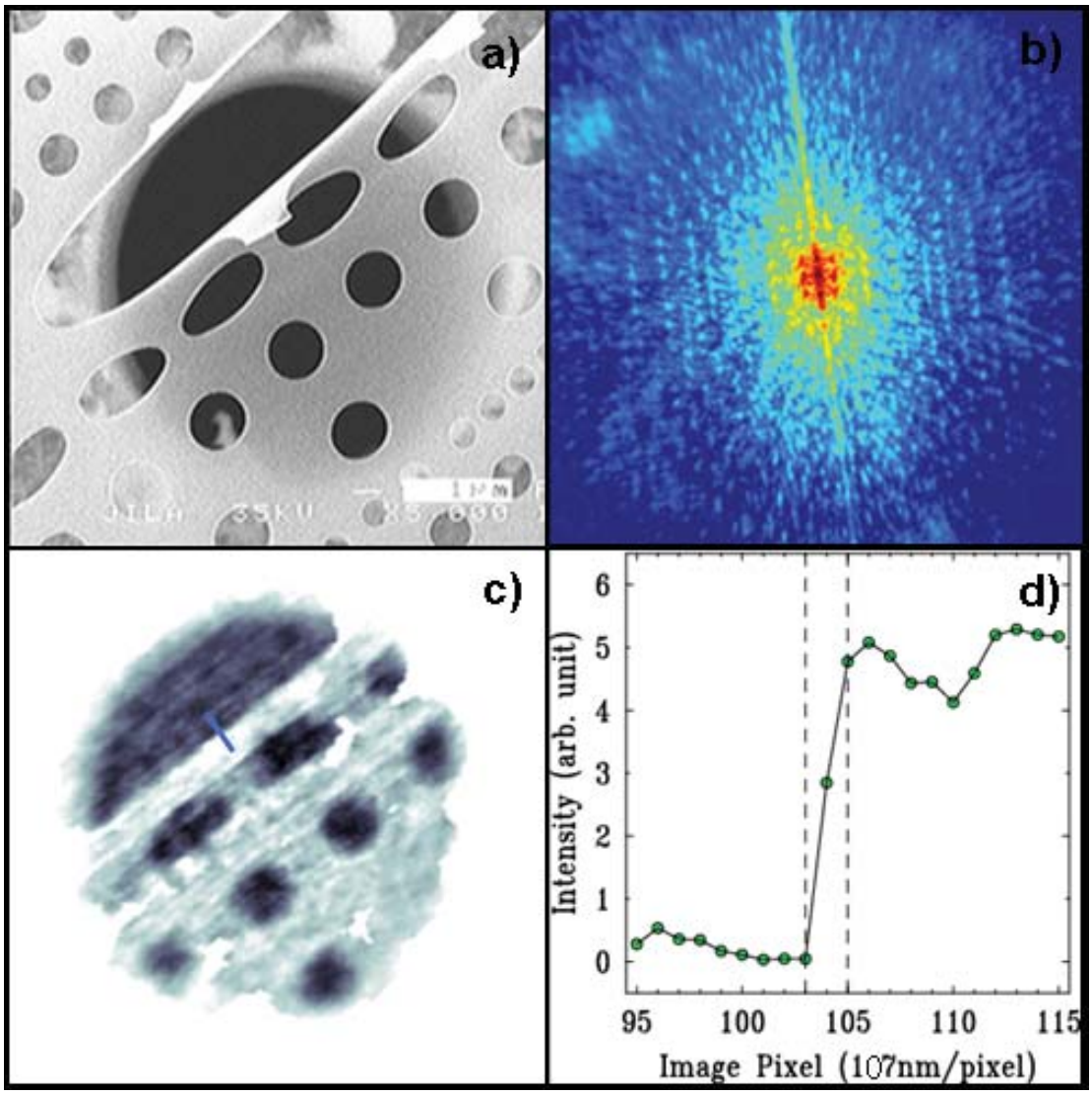

Figure 4.8: (a) SEM image of a masked carbon TEM film; (b) oversampled soft-x-ray diffraction pattern where the diffraction at the edge of the image corresponds to a momentum transfer of 0.059 nm^{-1}; and (c) magnitude of the reconstructed lensless image. The correspondence in size, number and position of holes, and aspect ratios between the EUV image and the SEM image can be seen. One pixel in the reconstructed image corresponds to 107 nm. The inset in (c) show a line-scan taken along the direction noted with the green solid line, demonstrating a spatial resolution of 214 nm [4].

4.9. By tilting the SEM stage by only a few degrees, we see that the number of holes that appear above the large 15 m aperture change. This finding adds strength to the argument that XCDI has a long depth of focus. Note that by measuring the shift in the holes, we can estimate the separation of the two films. With a tilt of 8 degrees, the holes in the film shift by 8 μm with respect to the aperture, giving us a separation of the two planes (aperture and quantifol) of about 56 μm. Since this distance is more than three times the size of the 15 μm laser-ablated aperture, there would be a significant amount of parallax. Thus we see that Figure 4.8 (c) and Figure 4.9 (b) agree well.

While these initial results were impressive, the resolutions are still low; comparable to a conventional optical microscope (see chapter 1). Three approaches are possible for improving the resolution of the microscope. First, higher spatial frequencies could be captured by going to a higher numerical aperture. This could be accomplished either by using a larger detector or moving the sample closer to the CCD. Second, the effective spectral bandwidth of the source could be improved by narrowing the individual harmonic peak or by using a tabletop SXR laser. Third, shorter wavelength HHG light could be used. The first two of these suggestions will be presented in the next section.

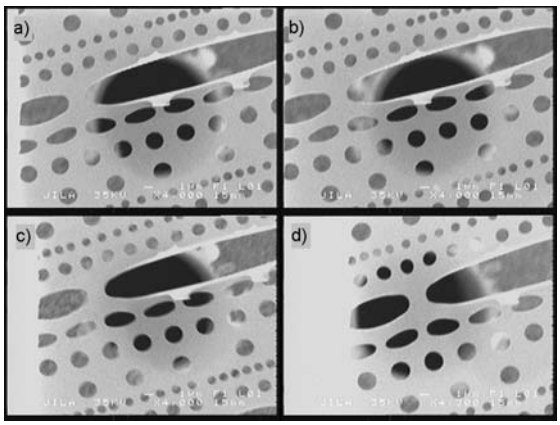

Figure 4.9: Scanning Electron Microscope images of 40 nm thick holey carbon film placed approximately 56 μm above a 15 μm aperture: (a) SEM stage at 0 degrees tilt, (b) SEM stage at -1.8 degrees tilt, (c) SEM stage at +1.8 degrees tilt, (d) SEM image at +8 degrees tilt.

4.4 Pushing the resolution: High Numerical Aperture XCDI

This section will describe work conducted to push XCDI to the sub-100 nm regime. The work continues with 29 nm HHG generation, but in a higher numerical aperture regime. Additionally, it will describe the work conducted on a tabletop SXR capillary discharge laser operating at 46.9 nm [75]. Both of these demonstrations will use high numerical aperture (NA) and achieve sub-100 nm resolution. Due to the high NA, a curvature correction scheme was developed to account for the high angle diffraction and allows near-diffraction-limited resolution of 1.5 λ. The SXR laser work was done with Przemek Wachulak and collaborators at Colorado State University in Fort Collins, Colorado in the groups of Mario Marconi, Jorge Rocca, and Carmen Menoni in the Electrical and Computer Engineering Department. The results of this section were published in the *Proceedings of the National Academy of Sciences of the USA* and much of the text in this section comes from that publication [5].

4.4.1 Experimental setup for high NA XCDI

The high NA experimental setup is shown in Figure 4.10. The same chamber as described earlier in section 4.1 was used. Coherent beams from either a soft x-ray laser or a high harmonic source are focused onto a sample using the same simple two-mirror relay arrangement. Light scattered from the object is then detected using a CCD camera positioned a few centimeters from the sample (typically 1.7 cm). Thin film filters are used to block unwanted longer wavelength radiation such as plasma emission from the laser. In the case of the soft x-ray laser, a single 100 nm thick aluminum filter was used to block plasma emission at longer wavelengths. For the high harmonic beams, two 200 nm thick aluminum filters blocked the driving laser light at 780 nm. Two multilayer mirrors, one flat and one with a 50 cm radius of curvature, were used to gently focus the soft x-ray beams onto the sample. Different bilayer thickness and

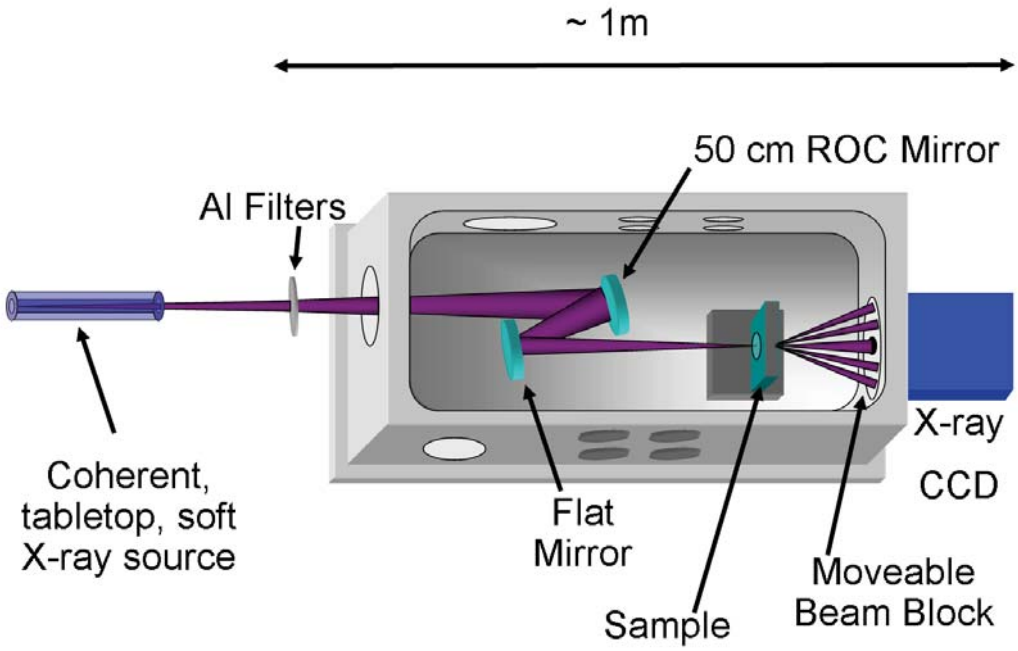

Figure 4.10: Setup of the tabletop soft x-ray diffraction microscope. A coherent soft x-ray beam is produced by high harmonic generation or by spatially filtering the emission from a capillary discharge laser in an Ar-filled hollow waveguide. The beam is gently focused by a multilayer mirror pair onto the sample, and the diffraction pattern is collected on an x-ray CCD. A moveable beam block allows for brighter portions of the diffraction pattern to be blocked to avoid saturating the CCD when acquiring the highest angle diffracted light [5].

materials (Sc/Si for 46.9nm or Mo/Si for 29 nm) were used to optimize reflection for the different wavelengths. The soft x-ray laser mirrors are 40% reflective at 46.9 nm, while the mirrors used to focus the high harmonic beam are 28% reflective at 29 nm.

The soft x-ray laser source is based on fast electric-discharge excitation in a thin capillary that creates a highly-ionized neon-like argon plasma lasing at $\lambda = 46.9$ nm. It produces pulses of energy ~ 0.2 mJ with ~ 4.5 mrad divergence at a repetition rate of 1 Hz [75]. Lasing takes place on the $3s^1P_1$ to $3p^1S_0$ transition of neon-like argon by exciting argon gas in an alumina capillary (3.2 mm diameter, 27 cm long) with a current pulse of amplitude ≈ 24 kA with a 10% to 90% rise time of ≈ 40 ns [75,127,128]. This laser occupies a footprint of 0.4 x 1 m^2. The fast current pulse is produced by discharging a cylindrical capacitor through a spark-gap switch connected in series with the capillary load. The current pulse rapidly compresses the plasma column to achieve a dense and hot plasma filament where a population inversion is created by electron impact excitation of the laser upper level and rapid radiative relaxation of the laser lower level [6]. The capacitor employs a water dielectric which provides high energy density and also cools the capillary. A continuous flow of Ar maintains a pressure of 490 mTorr in the capillary channel.

This laser is based on high-gain amplification of spontaneous emission from the laser transition and although it does not use a resonator, it nevertheless generates a beam with high spatial and temporal coherence. The longitudinal coherence length is determined by the Doppler-broadened linewidth of the laser transition at $\lambda/\Delta\lambda \sim 10^4$, corresponding to a longitudinal coherence length of $\xi_l \sim 500$ μm. The degree of spatial coherence increases with the length of the plasma column, and approaches full coherence for 36 cm long capillaries [96]. In this experiment, the laser output was spatially filtered to ensure good spatial coherence using a 1.5 mm diameter pinhole placed approximately 1.5 m from the output of the laser, where the beam is ≈ 1.5 cm in diameter. We estimate (using the van Cittert-Zernike theorem) that the beam has at least 85% fringe visibility

at the edges of the pinhole [6].

For both soft x-ray sources, the sample size was 7 μm. For the soft x-ray laser at 46.9 nm, the sample to CCD distance was 17 mm, giving an oversampling ratio of 8.5. For the high harmonic source at 29 nm, the sample to CCD distance was 42 mm, giving an oversampling ratio of 13. The samples used for both sources were 7 μm tall "waving stick girl" figures etched into a 100 nm thick silicon nitride window with electron-beam lithography by Anne Sakdinawat of the Center for X-ray Optics and Lawrence Berkeley National Laboratory. Since the silicon nitride is $\sim 4\%$ transmissive to 29 nm photons, 200 nm of gold was electroplated on the sample used with the high harmonic beam.

4.4.1.1 Phase retrieval of high NA data

Three separate exposures were used with similar beam blocks as described in section 4.1.2 and section 4.3.1 for both data sets, however for the high NA HHG data multiple shorter exposures were used. Similar data patching and processing steps were taken as was the case with the intial HHG XCDI data.All data sets were cropped down to an array of good signal to noise ratio data. For the SXR laser this was 1980 pixels square. For the HHG data included in the publication it was 2028 pixels. After background subtraction and filtering, the diffraction intensity was binned by numerically integrating 3x3 pixels into 1 pixel and then deconvolved with a sinc function [20].

Due to the strong absorption of soft x-rays by the specimen, the diffraction patterns in this section are non-centro-symmetric, resulting in the complex electron density. Phase retrieval of the complex electron density was carried out by using the guided hybrid-input-output (GHIO) algorithm (see sections 3.4 and 4.3.2) [20, 105]. This work used 20 initial reconstructions. After 3000 iterations, 20 images were reconstructed, which was defined as the 0th generation. An R-value was calculated for each image based on the difference between the measured and calculated magnitude of the Fourier transform. A seed image with the smallest R-value was selected for the reconstruction.

By multiplying the seed with each of the 20 images and taking the square root of the product, a new set of 20 images was obtained, which was used as the initial inputs for the next generation. We repeated the procedure for the next generation, and after the 7th generation, the 20 reconstructed images became consistent. The final reconstruction was chosen from the average of the best 3 images with the smallest R-values.

4.4.2 High NA results with 46.9 nm SXR laser

The coherent diffraction pattern from the first stick girl sample when illuminated by the soft x-ray laser for an exposure time of 300 shots (5 minutes at 1 Hz) is shown in Figure 4.11 (a). The final summed and processed diffraction pattern was then curvature corrected (explained in the next section) and is shown in Figure 4.11 (b). This diffraction has good signal to noise out to a 38 degree angle, or a NA = 0.62. This numerical aperture represented at the time the highest numerical aperture x-ray imaging at any wavelength.

Figure 4.11 (c) shows the final reconstruction of the stick figure. A lineout of the reconstructed image is shown in Figure 4.11 (c), indicating a resolution of 71 nm. This resolution, at 1.5 λ, compares very well with other lensless imaging experiments done at large scale facilities. Furthermore, our calculations have indicated that the resolution could reach the diffraction limit. The current resolution of 71 nm is limited by the size of the CCD detector, because the diffraction pattern in Figure 4.11 (b) was clearly cut off by the CCD edges. Using a larger CCD detector and the curvature-correction procedure, it should be possible to achieve diffraction-limited resolution using a tabletop soft x-ray diffraction microscope.

4.4.3 Curvature correction for high NA diffraction

The experimental setup was configured to enhance the spatial resolution by placing the detector as close to the sample as possible, which increases the numerical aper-

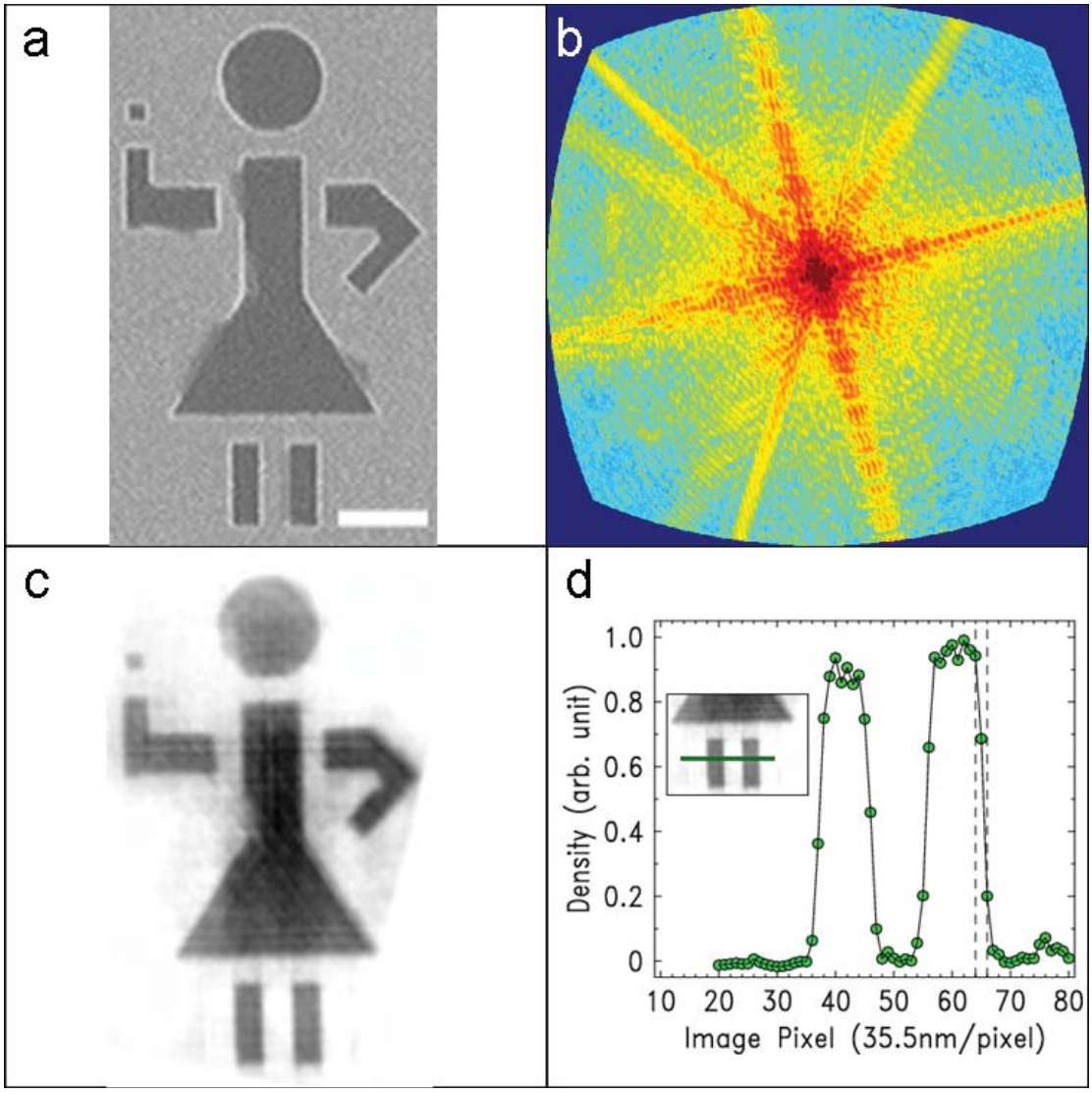

Figure 4.11: Lensless imaging using coherent soft x-ray laser beams at 47 nm. (a) Reflection image of the waving stick figure sample (scale bar = 1 micron) using an SEM. (b) Coherent soft x-ray diffraction pattern (in transmission) after curvature correction (maximum momentum transfer of 0.166 nm^{-1} at the edge of the CCD). (c) Reconstructed image with curvature correction. (d) Line-out of the image along the legs (shown in the inset), verifying a resolution of 71 nm [5].

ture of the microscope (up to NA = 0.62 here). In this mode of operation, the approximation of $\sin(\theta) \approx \theta$ is no longer valid, and therefore the diffraction intensity on the planar CCD is significantly distorted at higher angles, as can be seen in Figures 4.12 (a) and (b). To remove the distortion, we interpolated the diffraction pattern from a plane onto a spherical surface. Figures 4.12 (d) and (e) show the curvature-corrected diffraction pattern, where the radial stretching and skew of the speckles near the edge of the diffraction pattern (corresponding to high diffracted angles) are clearly removed. Figures 4.12 (c) and (f) show the magnitude of the reconstructed image before and after curvature-correction, indicating that curvature-correction indeed significantly improves the quality of the reconstruction. The lower width and increased sharpness of the curvature-corrected stick-girl image can be seen in the lineouts shown in the inset of Figure 4.12 (c) and (f). This correction of mapping the diffraction pattern onto a curved surface is really only a first approximation correction. A forthcoming publication that is an extension of this work with a more detailed curvature correction will soon be submitted with Kevin Raines and colleagues from John Miao's group at the University of California at Los Angeles.

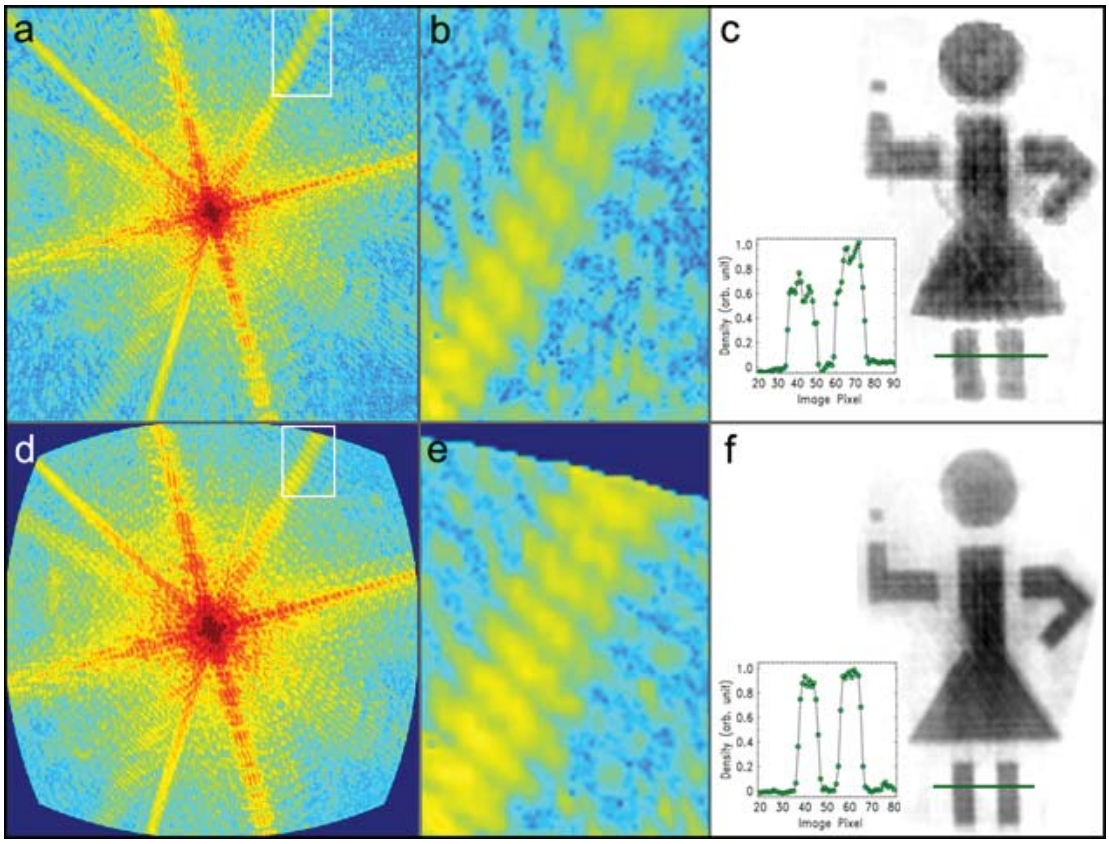

Figure 4.12: Curvature correction in high numerical aperture lensless imaging. (a), (d) Coherent soft x-ray diffraction pattern at 47 nm wavelength (in transmission) before and after curvature correction (maximum momentum transfer of 0.166 nm^{-1} at the edge of the CCD). (b), (e) Magnified diffraction pattern at high diffraction angles showing the radial blurring near the upper right edge in (b), which is absent in (e). (c), (f) Reconstructed image of waving stick figure without and with curvature correction. The lower width and increased sharpness of the curvature-corrected stick-girl image can be seen in the lineouts shown in the insets [5].

4.4.4 High NA results with 29 nm HHG

After the success of the high NA XCDI on the tabletop SXR laser, we repeated the experiment with a similar sample on the 29 nm HHG source. As mentioned before, this sample was coated with 200 nm of gold to prevent transmission of the 29 nm photons through the 100 nm Si_3N_4 substrate. Also, as was mentioned in section 4.1, for this work a shorter 5 cm waveguide was used which increased the 29 nm flux by almost an order of magnitude (to around 10^8 photons/s or 0.7 nW on the sample) while still maintaining a fully Gaussian mode and full spatial coherence. Two data sets are shown here that both have maximum scattering angles of about 18 degrees corresponding to a NA = 0.31. The first data set shown here actually came after the second, because only the first data set was published due to its higher image quality [5]. However both data sets demonstrate sub-100 nm resolution, a factor of two improvement over the Quantifoil data [4] and previously reported HHG zone plate microscopes [55].

Figure 4.13 summarizes the first data set of high resolution imaging results using a high harmonic source. A reflection image of a gold coated stick girl sample using an SEM is shown in Figure 4.13 (a), while Figure 4.13 (b) shows the curvature corrected high dynamic range soft x-ray diffraction pattern in transmission (NA = 0.31). Figure 4.13 (c) shows the reconstruction of the 7 μm stick figure, with a resolution of 94 nm verified in the lineout of Figure 4.13 (d). The reconstructed image has excellent fidelity with the SEM image, with the exception of missing the right hand. This is due to the finite resolution of the reconstruction, which is greater than the hand feature size, and possible incomplete etching of the substrate in this region.

Compared with Figure 4.11 (c), Figure 4.13 (c) shows slightly more internal density fluctuations, which is likely due to the lower temporal coherence (higher spectral bandwidth) of the high harmonic source compared with the soft x-ray laser. On the other hand, the region outside the sample boundary in Figure 4.13 (c) is much cleaner,

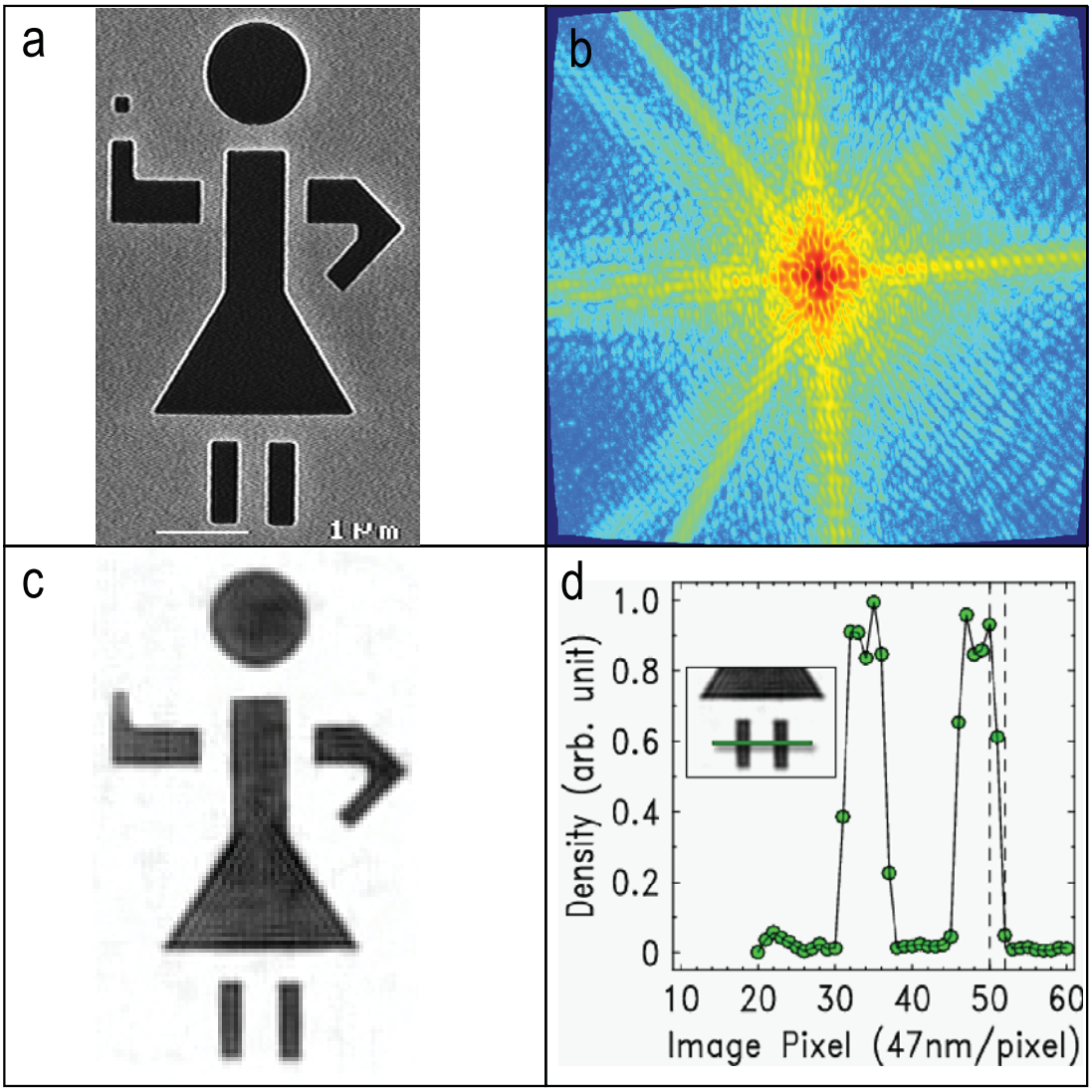

Figure 4.13: Lensless imaging using coherent high harmonic beams at 29 nm. (a) Reflection image of the sample (scale bar = 1 micron) using an SEM. (b) Coherent soft x-ray diffraction pattern (in transmission) after curvature correction (maximum momentum transfer of 0.134 nm^{-1} at the edge of the CCD). (c) Reconstructed image (d) lineout of the image along the legs (shown in the inset), demonstrating a resolution of 94 nm [5].

which is attributed to the higher spatial coherence of the high harmonic source. In addition, the higher spatial coherence of the high harmonic source allows all the output flux to be used, while the higher spectral bandwidth can support sub-10 fs pulse duration for dynamic imaging experiments. Furthermore, the bandwidth of the high harmonic source can be engineered through a variety of coherent control techniques, which will make it possible to precisely determine the time-space resolution tradeoff for such a source. In the case of the soft x-ray laser, an increase of the capillary length can simultaneously make the output essentially fully spatially coherent and significantly increase the pulse energy, making single shot exposure possible. These two sources are complementary and have actually been combined in a recent demonstration of HHG amplification in a tabletop SXR laser [58]. This source will prove very useful for single shot XCDI as it exhibits full spatial and temporal coherence.

Figure 4.14 shows the older high NA results from 29 nm HHG. This very interesting sample was sputter coated with a small DC sputtering chamber at JILA after already having been etched through using standard electron beam lithography. The sample in Figure 4.13 was coated with gold before etching, thus it has much cleaner edges. This result had significantly more noise in the diffraction pattern and reconstruction probably due to instability in the diffraction after an hour of exposure time for the large beam block data. All previous results in this chapter, besides Figure 4.13, were taken in the same way. A single hour long exposure on a CCD allows for significant accumulations of thermal and cosmic ray noise. However, the data in Figure 4.13 was recorded through 6 separate 20 minute exposures for 2 hours of exposure. This method allowed the individual exposures to be compared in order to make removal of cosmic rays easier. Additionally, this allowed for monitoring of the diffraction signal between the individual exposures. If the signal started to drift, the coupling into the front of the waveguide could be adjusted without affecting the harmonic beam pointing, thus allowing us to bring back the HHG signal. This greatly increased the stability of the

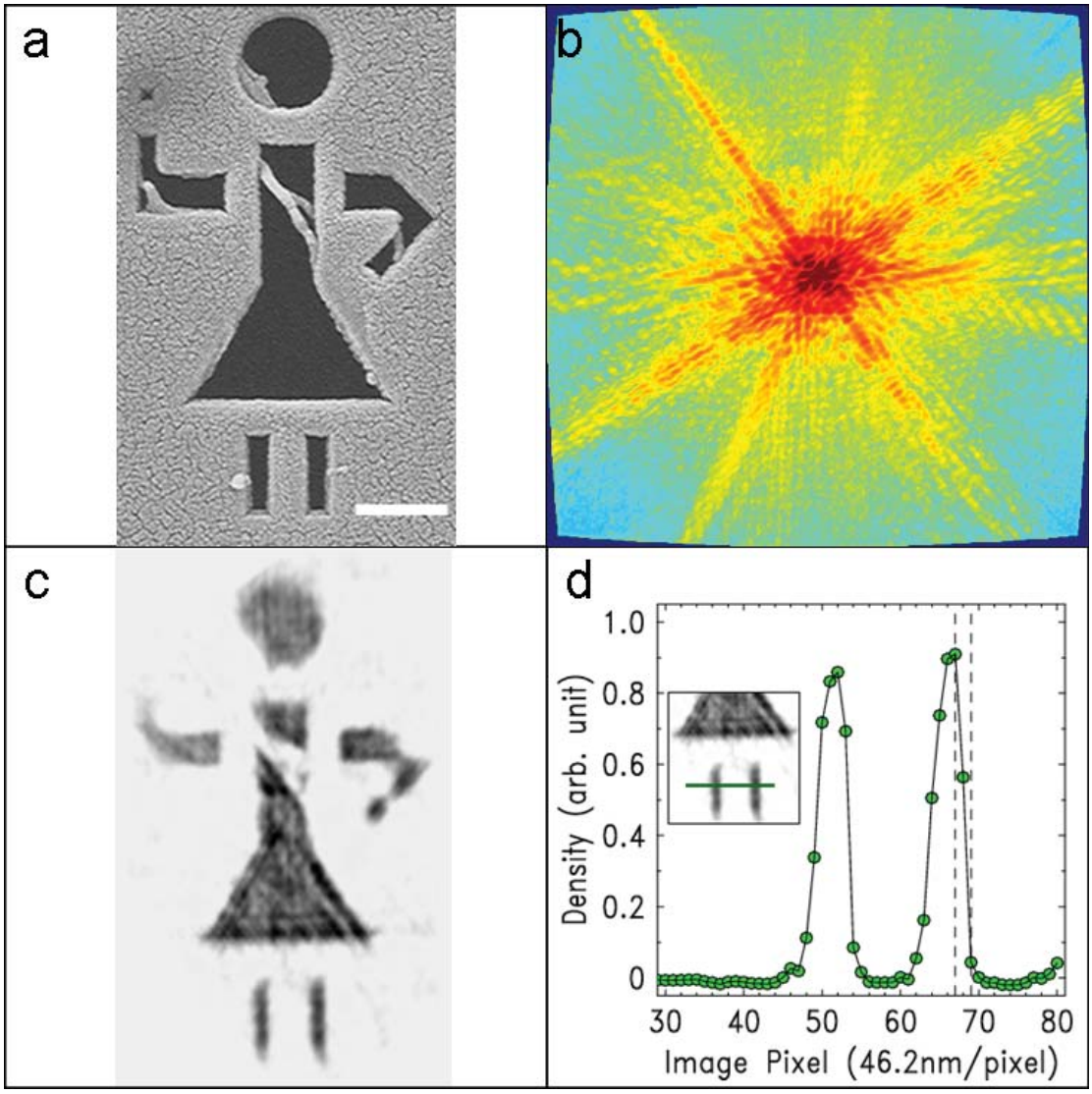

Figure 4.14: A previous demonstration of lensless imaging using coherent high harmonic beams at 29 nm. (a) Reflection image of the sample (scale bar = 1 micron) using an SEM. (b) Coherent soft x-ray diffraction pattern (in transmission) after curvature correction (maximum momentum transfer of up to 0.134 nm^{-1} at the edge of the CCD). (c) Reconstructed image (d) lineout of the image along the legs (shown in the inset), demonstrating a resolution of 92.5 nm.

signal and quality of the diffraction data.

4.5 Chapter Summary

This chapter presents the first high resolution XCDI results with tabletop coherent x-ray sources. Both reflection and transmission imaging schemes were presented. Approximately 200 nm resolution was achieved in a thick ($\sim$ 56 μm) sample using a 29 nm HHG source [4]. Higher resolutions (sub-100 nm) were shown using high numerical aperture geometries with two sources: a 46.9 nm capillary electrical discharge laser and the same 29 nm HHG source [5]. This high NA scheme, with NA up to 0.62, was a first for x-ray imaging and made possible near wavelength limited resolution (1.5 λ). As we scale these techniques to shorter wavelengths it may be possible to obtain sub-10 nm resolution with 3 nm water window light. However, at these shorter wavelengths tabletop sources will have lower flux levels. The next chapter will discuss a method of increasing image signal to noise with very low exposure levels.

Chapter 5

Pushing the Limits: Tabletop Fourier Transform Holography

The previous chapter demonstrated that tabletop coherent SXR sources can enable near wavelength limited XCDI [4,5]. However, the wavelengths used (29 and 47 nm) are not useful for probing thicker samples because they are very strongly absorbed [6]. Therefore, shorter wavelengths are desired to truly enable the usefulness of tabletop XCDI. As these shorter wavelength sources become available, they will initially have limited flux. Multi-reference holographies have demonstrated that good signal to noise images can be produced with relatively low flux [15, 116]. This chapter demonstrates one such holography, multi-reference Fourier transform holography on a tabletop coherent SXR source. These results came as part of an ongoing collaboration with Bill Schlotter and have been accepted for publication in *Optics Letters* [26]. Much of the text in this chapter has come out of drafts for that paper. Bill Schlotter's dissertation is an excellent source for the theory, application, and experimental considerations of FT holography [15].

5.1 Toward shorter wavelength tabletop XCDI

As was mentioned in section 3.5.2, another diffractive imaging technique that is complementary to CDI with iterative phase retrieval is Fourier transform holography (FT holography). Recent work using light from synchrotron sources and the FLASH free electron laser demonstrated that the image quality of FT holography can be improved

with short exposure times by employing multiple or parallel references beams [116, 123, 129, 130]. Thus FT holography is an attractive technique for tabletop soft x-ray microscopy where sources have limited flux.

In this work, we present the first implementation of multiple reference Fourier transform holography on a tabletop coherent x-ray source. We achieve 89 nm image resolution using 29 nm light, showing for the first time that multiple reference Fourier transform holography is viable for imaging with high numerical apertures (as high as NA >0.5). Then, using oversampling and an iterative algorithm to refine the Fourier transform holography images, we improve our image resolutions to <53 nm, demonstrating the highest numerical aperture x-ray holography to date. Finally, we show that Fourier transform holography can be used effectively with exposure times as short as 30 s for an image resolution of 125 nm. This represents a significant improvement over prior demonstrations of lensless imaging using high harmonic sources - where exposure times of more than an hour are required for comparable image quality [4, 5]. Because the ultrafast laser system used is available in many laboratories worldwide, this work can find application in many areas of science and technology.

5.2 Theory of Fourier Transform Holography

In FT holography, an unknown sample object and a known reference structure are illuminated with a single coherent beam. Interference between the scattered light from reference and object are detected in the far field as a Fourier transform hologram [113, 114, 131–134]. This is demonstrated schematically in 1D in Figure 5.1. The hologram is recorded as a diffraction pattern on an area detector-typically a charged-coupled device (CCD) camera. An image of the sample is then easily reconstructed by computing the magnitude of the two dimensional Fourier transformation of the detected hologram. To obtain the highest possible image resolution, the reference beam should diverge very strongly (corresponding to a small point spread function), thus requiring a small

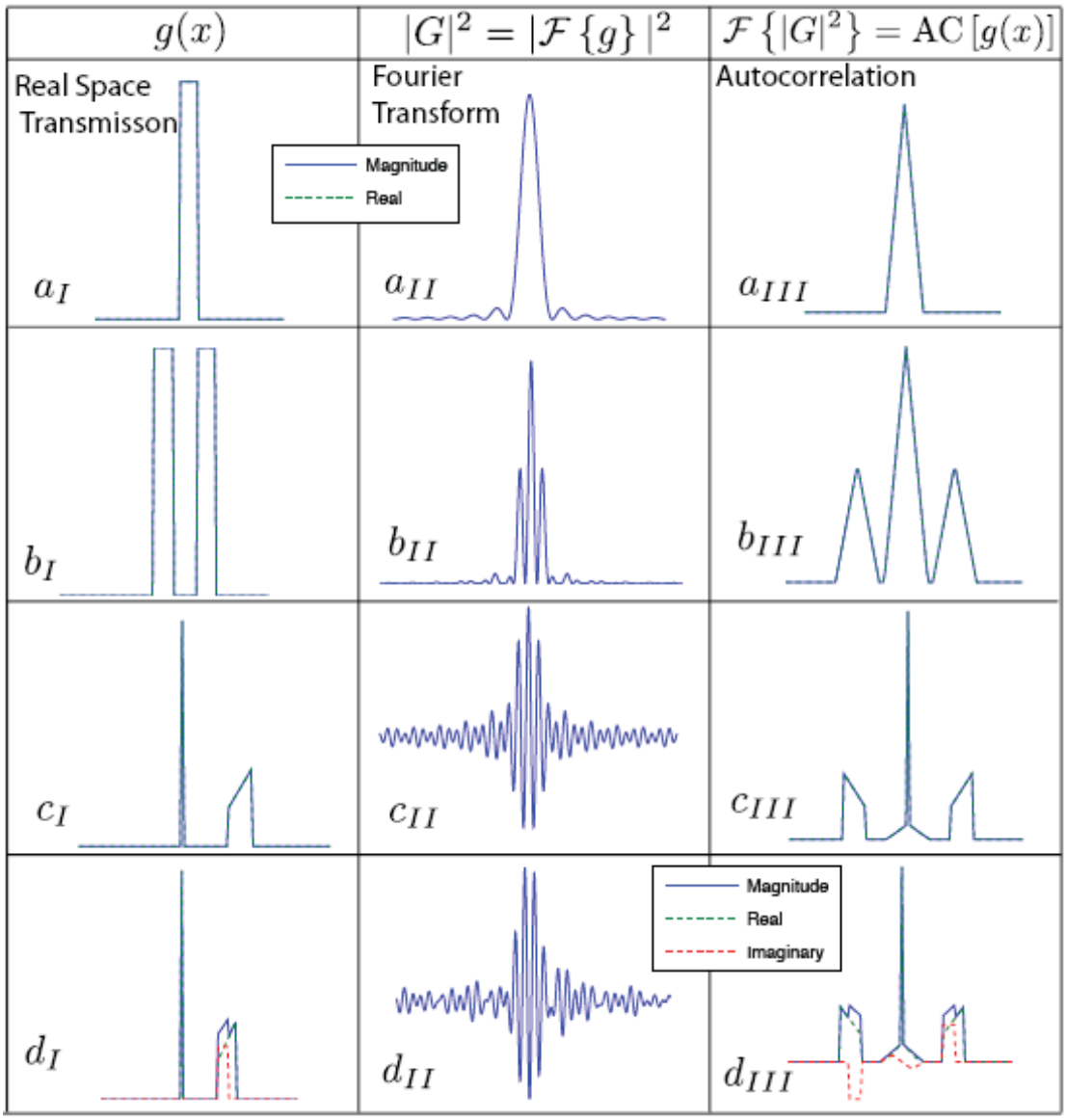

Figure 5.1: Schematic of Fourier relationship and Fourier Transform holography in 1 dimension (from Schlotter [15]). Column one shows different transmission functions ($g(x)$). Column two shows $|G|^2$, the magnitude squared of the Fourier transform (far field diffracted intensity) of $g(x)$ in column one. Column three shows the autocorrelation $F\{|G|^2\}$ of the diffracted wave. Row (a) shows the transmission, diffraction, and autocorrelation of a single slit. Row (b) shows the same information, except for a double slit. Notice now that in the autocorrelation there is a self-correlation peak (center) and cross-correlations peaks between the two slits (side peaks). Row (c) shows a sample (trapezoid) and delta-function-like reference point in transmission, diffraction, and autocorrelation. Now the autocorrelation cross-correlation peaks produce an image of the trapezoid sampel and its complex conjugate. This can be seen expecially in Row (d) where the trapezoid sample is complex.

reference source size located in the same plane as the sample. The size of the reference hole ultimately puts the limit on the image resolution obtainable in FT holography. Schlotter sets this limit at about 70% of the reference hole diameter in section 2.2 [15]. Several methods have been used to produce a small reference beam at soft x-ray wavelengths, such as tightly focusing a beam with a Fresnel zone plate lens [135], introducing a small scattering particle [136, 137], or drilling a small reference hole on the same slide that holds the sample [15, 48, 116, 138].

5.2.1 Mathematical representation of FT holography

To further understand the relevant theory of FT holography, we present a simplified mathematical treatment of it as presented in Bill Schlotter's dissertation [15]. If an opaque mask consisting of an object with transmission $t_o(x, y)$ and a reference hole with transmission $t_r(x, y)$ are simultaneously illuminated with a coherent light source with amplitude E_o, then the transmitted wave immediately behind the mask will be a sum

$$E(x, y) = E_o t_o(x, y) + E_o t_r(x, y) = r(x, y) + o(x, y) \tag{5.1}$$

where we have made the substitution $o(x, y) = E_o t_o(x, y)$ and $r(x, y) = E_o t_r(x, y)$. In the far field, the diffracted wave or hologram will take on the form of the Fourier transformation of $E_h(X, Y)$ as follows

$$E_h(X, Y) = \mathscr{F}[\epsilon(x, y)] = \mathscr{F}[r(x, y)] + \mathscr{F}[o(x, y)] \tag{5.2}$$

$$E_h = R + O. \tag{5.3}$$

Here the capital letters R and O represent the Fourier transform of r and o respectively and X, Y are the far field coordinates. Now, when we measure the hologram E_h in the far field, we only detect the intensity, I_h as

$$I_h = |R + O|^2 = \underbrace{RR^* + OO^*}_{AC} + \underbrace{OR^* + RO^*}_{XC} = \underbrace{|R|^2 + |O|^2}_{AC} + \underbrace{OR^* + RO^*}_{XC} \tag{5.4}$$

where $*$ represent complex conjugation, AC are the diffraction from each aperture alone and XC represents the interference between the two apertures.

Now, in order to retrieve the image imformation, we perform the spatial autocorrelation of the hologram by Fourier transformation

$$\mathscr{F}[I_h] = \mathscr{F}[|R|^2] + \mathscr{F}[|O|^2] + \mathscr{F}[OR^*] + \mathscr{F}[RO^*] \tag{5.5}$$

$$E_{rec} = \underbrace{r \star r + o \star o}_{AC} + \underbrace{o \star r + r \star o}_{XC} \tag{5.6}$$

where $\star$ represnts the complex correlation, r and o are the original transmitted fields of the reference and object respectively and E_{rec} is the recovered field of the spatial autocorrelation. We see that the recovered field contains the AC self correlation terms which appear at the center (DC) of the autocorrelations and that these will be surrounded by the XC cross correlation terms. These XC terms will represent a cross-correlation of the reference hole with the object and its complex conjugate. If the reference is very small compared to the object, then the cross correlation is a high resolution image.

5.2.2 Multiple reference FT holography

To increase the signal-to-noise of images produced using FT holography, multiple reference beams can be used [15, 116]. In multiple reference FT holography, each reference beam produces a separate image in the autocorrelation reconstruction. These images can then be averaged to improve the signal to noise and image quality [15, 116]. Schlotter *et al* demonstrated that a high resolution image could be obtained with only 2500 detected photons with this technique [15]. Some care needs to be taken when surounding a sample with multiple references in order to assure that the individual reconstructed sub-images do not overlap. The treatment of this issues is dealt with in Schlotter section 4.2 [15]. This technique could be useful for obtaining images with low flux HHG sources at shorter wavelengths.

5.3 First Demonstration of Tabletop X-ray FT Holography

This section summarizes the experimental setup and results of tabletop FT holography from a coherent 29 nm HHG source. To our knowledge, this is the first demonstration of x-ray FT holography on a tabletop source with sub-100 nm resolution.

5.3.1 Experimental setup for tabletop SXR FT holography

The schematic of the experimental setup is shown in Figure 5.2. The driving laser, harmonic setup, and illumination optics are all the same as described earlier in section 4.1 and in [4,5]. However, here, as in the high numerical aperture work, a 5 cm fiber was used in stead of a 10 cm fiber for increased 29 nm flux ($\sim 10^8$ photons/second or about 0.7 nW onto the sample). The mode quality and coherence properties are still preserved with this waveguide. Figure 5.3 shows the mode of the 29 nm beam from a 5 cm waveguide on a logarithmic scale with a power of about 0.7 nW in a bandwidth of about $\lambda/\Delta\lambda = 250$ at 29 nm. The beam saturated the CCD camera in less than 100 ms.

The test object used for this work is a nanostructured pattern inspired by the 1951 USAF test target, surrounded by five fully transmissive reference holes of $\sim 125 \pm 6$ nm diameter, as seen in Figure 5.2. The substrate for the sample is a 100 nm thick low stress, non-stoichiometric silicon nitride membrane. An x-ray opaque 400 nm Au film was deposited on the membrane by DC magnetron sputtering. The test object was milled into the 400 nm of gold using a focused ion beam, leaving only the silicon nitride membrane. The silicon-nitride membrane transmits $\sim 20\%$ of the incident 29 nm light, yielding a total photon flux through the test object roughly matched to the transmission through each one of the reference holes. This ensures good contrast in the interference fringes of the hologram, and thus of the reconstructed image. Schlotter 3.4 discusses the specifics of the sample preparation technique with FIB milling [15].

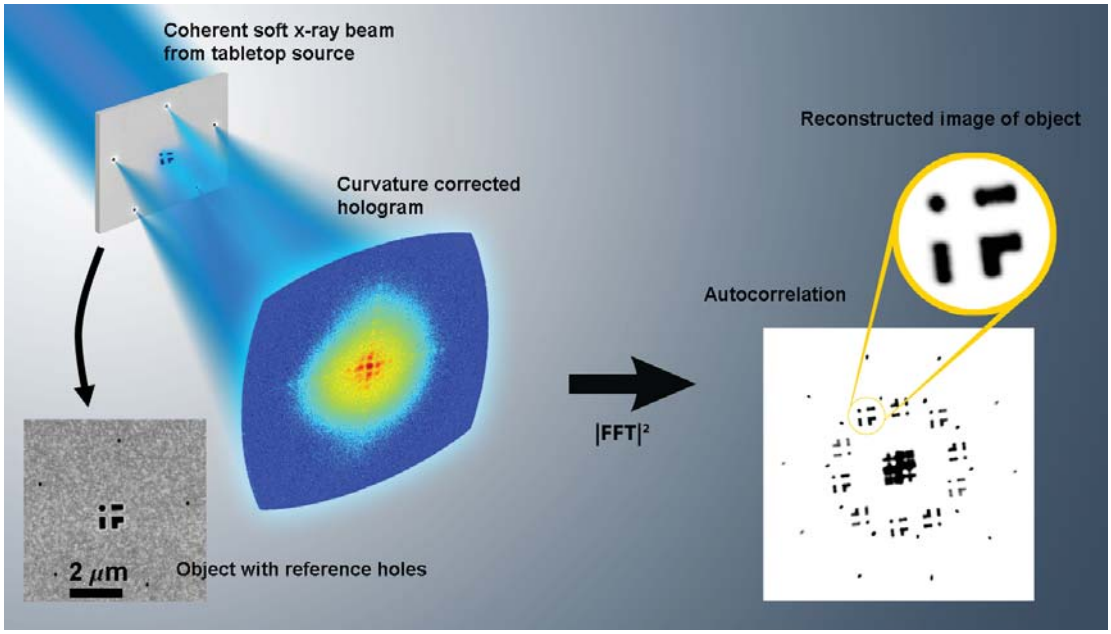

Figure 5.2: Schematic of multiple reference Fourier transform holography with a tabletop soft x-ray source. A coherent soft x-ray beam with $\lambda = 29$ nm from a tabletop high harmonic source illuminates a test pattern surrounded by five reference holes. The scattered soft x-ray light interferes and is recorded on a CCD camera in the far field as a hologram (log scale). Due to the high scattering angles recorded in the hologram, curvature correction is necessary. The spatial autocorrelation of the object can be retrieved by taking the squared magnitude of the Fourier transform of the hologram. A single sub-image from the hologram is shown demonstrating 89 nm resolution (Photo credit Greg Kuebler) [26].

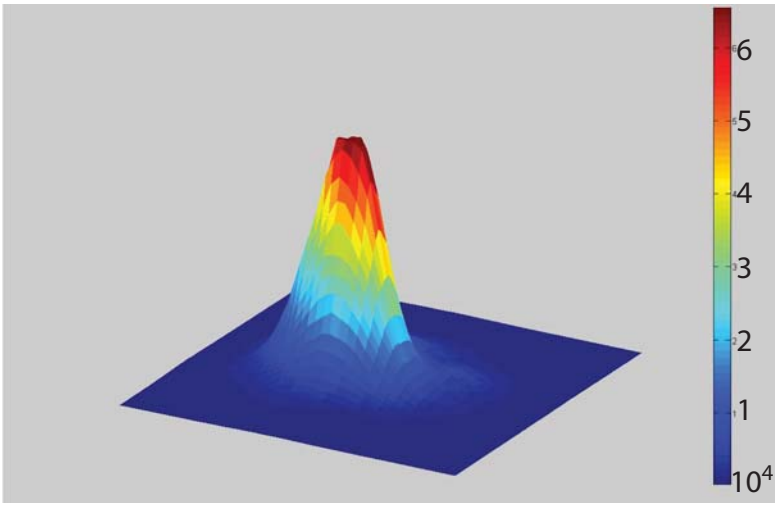

Figure 5.3: Logarithmic mode of a 29 nm Gaussian HHG beam from a 5 cm waveguide with about 0.7 nW of power in a bandwidth of about 250.

5.3.2 Results of 29 nm tabletop FT holography

Figure 5.4 summarizes our experimental results using FT holography alone. Figure 5.4 (a) shows a logarithmic, curvature corrected hologram of the sample shown in Figure 5.2. There is only 17 mm between the sample and the center of the detector (momentum transfer of $Q = 0$). Nevertheless signal can be detected above the noise more than 700 pixels away from the center (Q_{max}= $\pm$0.211 nm^{-1}). Such a large numerical aperture (NA=0.5) does not comply with the paraxial approximation because the wavefront originating at the sample will be significantly distorted when recorded on a flat detector. Correction of the curvature is accomplished by mapping the flat hologram onto a spherical surface as described in section 4.4.3. This technique corrects for distortions such as pixel skew and stretching at higher angles [5].

The hologram in Figure 5.4 (a) is a summation of 8 separate 600 second exposures that were each individually background subtracted. Additionally, fixed pattern noise and cosmic rays were removed for each exposure. After the individual exposures are summed, the hologram is curvature corrected. Because the curvature correction introduces a region of zeros at high Q, a Gaussian filter is applied to smooth the edge of the data. This last step prevents ringing after Fourier transformation of the hologram that would otherwise arise due to the presence of a hard edge in the data. The magnitude squared of the correlation reconstruction is shown in Figure 5.4 (b) and results from the magnitude of the spatial Fourier transformation of the hologram. At the center of the autocorrelation is the self-correlation of the sample. Surrounding these self-correlation terms are five object-to-reference cross correlations and their complex conjugates. Surrounding these cross-correlation sub-images are the reference-reference cross correlations. The difference in the intensities of the sub-images is caused by fluctuations in the flux transmitted through the reference holes due to variations in the size of the holes and non-uniform illumination of the sample.

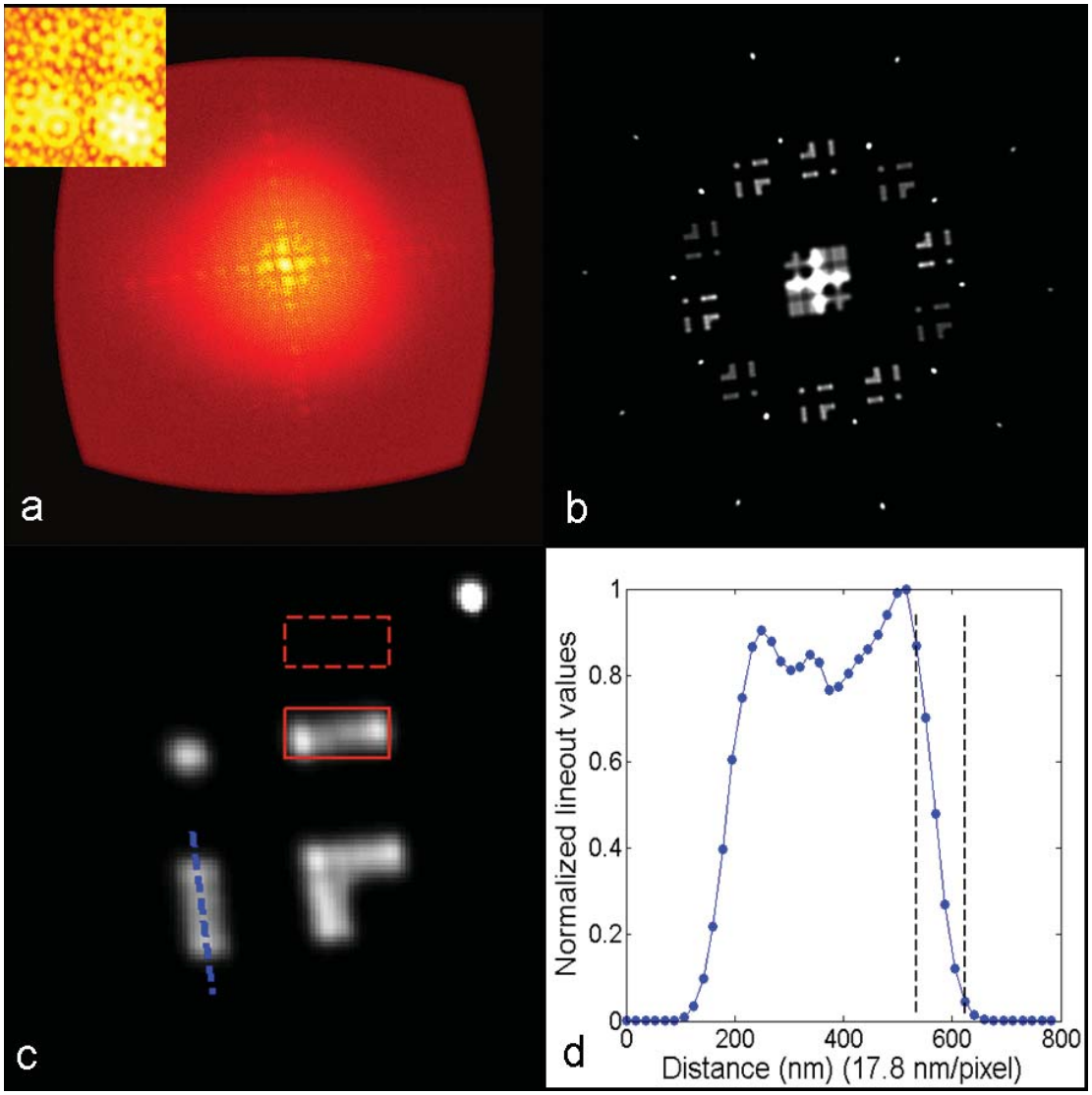

Figure 5.4: (a) Curvature corrected logarithmic hologram from composite 4800 s of exposure (8 separate 600 s exposures with maximum momentum transfer of $Q_{max} = \pm 0.211$ nm^{-1}). The inset shows the detail of the center of the diffraction pattern. (b) Magnitude squared of the autocorrelation reconstruction of the sample - the variations in sub-image intensity are most likely due to variations in reference hole transmitted intensity. (c) A single sub-image reconstruction with a sample line cut (blue dotted line). (d) Plot of the line-out demonstrating 89 nm resolution with a signal to noise of 73 [26].

One of the five sub-images from the autocorrelation shown in Figure 5.4 (b) is enlarged in Figure 5.4 (c). The signal-to-noise ratio in this image is measured by taking the mean of the autocorrelation signal magnitude in the red solid box and dividing it by the standard deviation of the pixels in the dashed red box which represents a zero signal background region. The signal-to-noise of this image is 73. Figure 5.4 (d) shows a lineout along the dashed blue line shown in Figure 5.4 (c), demonstrating a resolution of 89 nm. This resolution is more than four times higher than the highest resolution holographic image previously recorded using a tabletop source [56], and is only three times the illuminating wavelength of 29 nm. This result once again demonstrates that diffractive imaging can be used at very high numerical aperture with tabletop sources to achieve very high spatial resolution [5]. Given the very high signal-to-noise demonstrated in Figure 5.4, the exposure time can be reduced substantially. The fundamental resolution limit for this geometry where the object is convolved with a circular reference is $\sim 70\%$ of the diameter of the 125 nm reference holes, or $\sim$ 88 nm. In our current experiment, a resolution limited by the size of the reference holes, rather than the hologram signal-to-noise ratio, is obtained after only about 120 seconds of exposure.

5.3.3 High resolution FT holography with short exposures

In microscopy, a sample is often searched at lower resolution to identify a particular region of interest. Fourier transform holography is inherently a fast and simple imaging technique and the use of multiple references has myriad attributes including improved image redundancy [15,116]. This is particularly advantageous for rapidly surveying a sample. We demonstrate this by showing that useful image resolution can be achieved after only 30 s of exposure. Figure 5.5 (a) shows the hologram recorded with a 30 s exposure, containing approximately 15,000 detected (29 nm) photons. Figure 5.5 (b) shows one sub-image, where the signal-to-noise was calculated in the same way as for Figure 5.5 (c), and where a lineout was taken along the blue dashed line. The

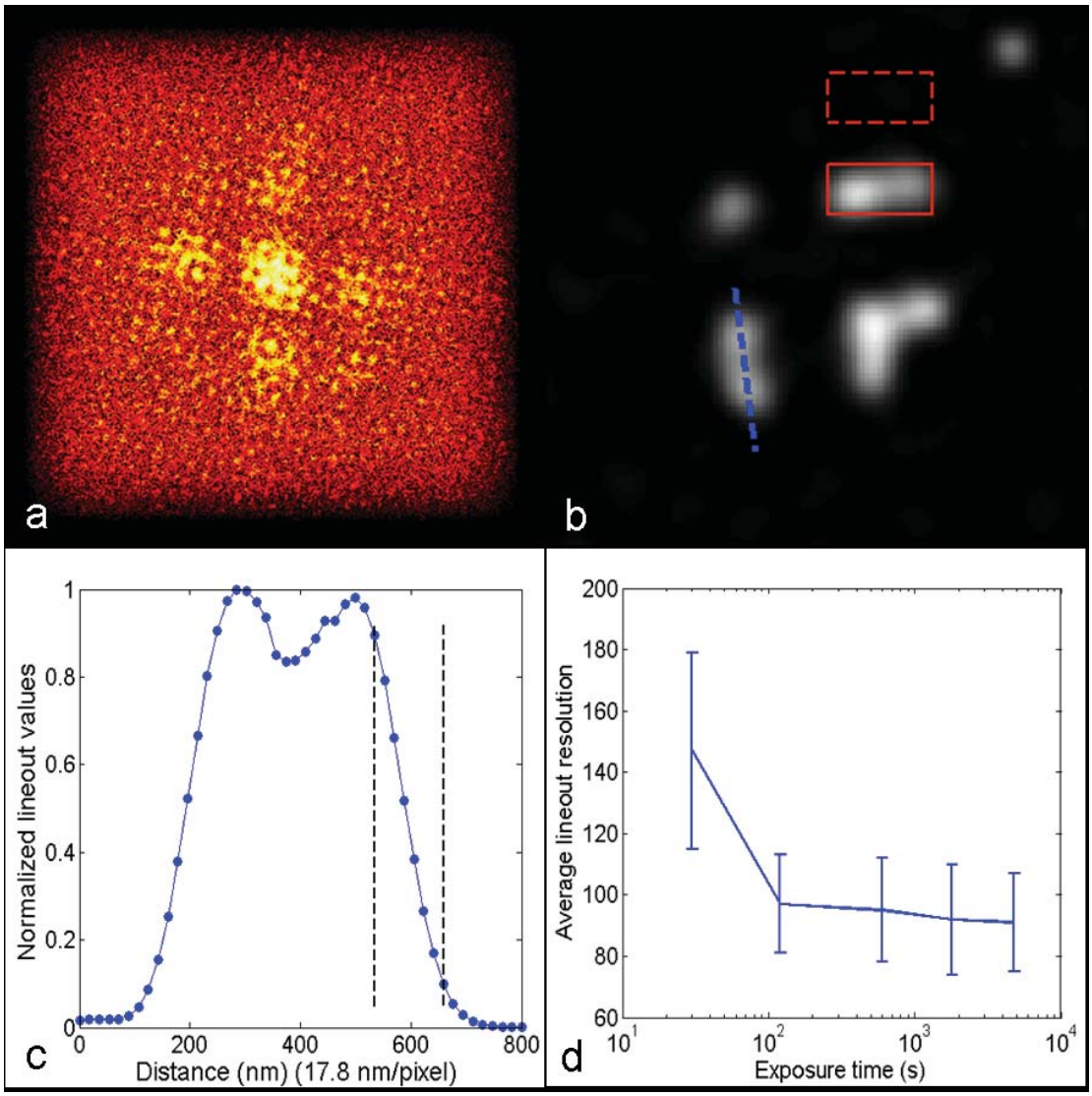

Figure 5.5: (a) Hologram recorded from a 30 s exposure (maximum momentum transfer of $Q_{max} = \pm 0.045$ nm^{-1}). (b) Sub-image from the magnitude squared of the autocorrelation for a 30 s exposure showing a lineout (blue dashed line). (c) Lineout of sub-image showing 125 nm resolution and a signal to noise ratio of 12.7. (d) Average of 20 lineout resolution measurements (4 per sub-image) per time step as a function of exposure time with error bars, showing the standard deviation of the resolution. Each diffraction pattern array was 2048 x 2048 pixels. The array was set to zero outside of the region where the signal from the diffraction pattern dropped below the noise. This reduced the noise in the reconstructed autocorrelation [26].

signal-to-noise ratio is 7, and the lineout resolution is 125 nm, as shown in Figure 5.5 (c). We note also that the current setup has a low ratio of detection photons to generated EUV light ($\ll 1\%$), due to the mirrors and filters in the beam path. Substantial reductions in exposure time are possible using a higher throughput setup, perhaps enabling near real-time diffractive imaging. Figure 5.5 (d) shows how the resolution scales as a function of exposure time for FT holography by taking the average of 20 lineouts (4 per sub-image) for exposure times of 30 s, 120 s, 600 s, 1800 s, 4800 s. Figure 5.5 (d) shows that the maximum image resolution achievable with the 125 ± 6 nm reference holes of 89 nm was attained after approximately 120 s of exposure.

5.3.4 Effects of high NA on FT holography

The importance of curvature correction for high numerical aperture Fourier transform holography is illustrated in Figure 5.6. Figure 5.6 (a) shows the non-curvature corrected composite 4800 s exposure hologram. A single autocorrelation sub-image from the non-curvature corrected data is shown in Figure 5.6 (b). These are compared to the curvature corrected hologram and corresponding autocorrelation sub-image in Figure 5.6 (c) and Figure 5.6 (d). The curvature correction eliminates the apparent aberration and thus substantially increases the image sharpness and clarity.

5.3.5 Hybrid holography phase retrieval approach

In microscopy, often a particular region of interest is isolated for a detailed higher resolution image. It is possible to significantly enhance the resolution of Fourier transform holographic images by applying an iterative algorithm to the oversampled hologram [22, 123, 129, 130, 138, 139]. The only input necessary for this hybrid approach is the previously recorded hologram. In real space the resolution of the holographic image reconstruction is limited by the extent of the reference. But for the hologram, in reciprocal space this restriction on resolution equates to the angular extent of the

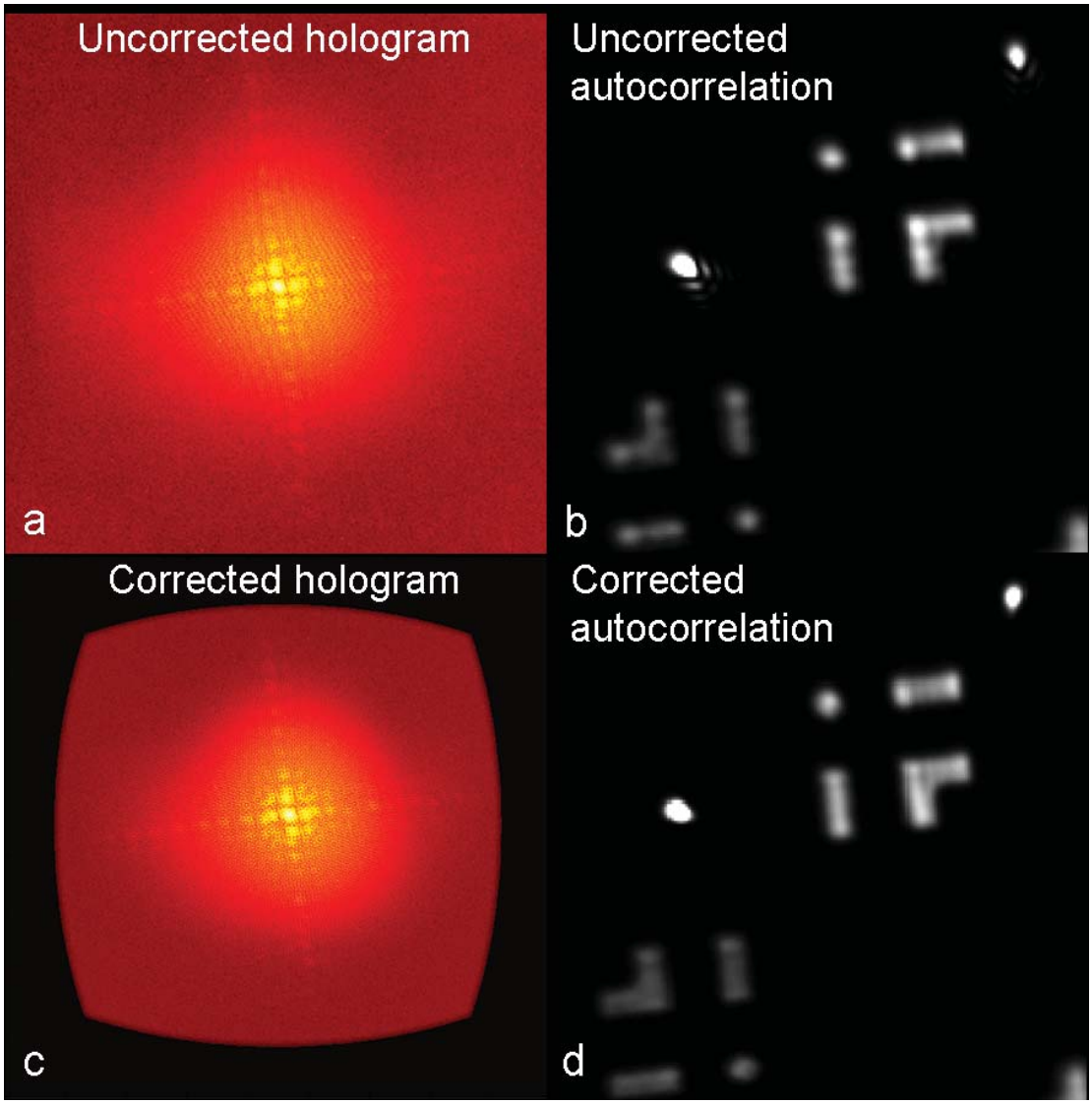

Figure 5.6: (a) Log of the non-curvature corrected hologram; (b) sub-image from autocorrelation without curvature correction showing image distortion; (c) log of the curvature corrected hologram; (d) sub-image from autocorrelation with curvature correction showing improved image quality.

reference wave, which is simply the Airy disk resulting from diffraction by the reference holes (see Figure 5.2). If light scattered from the unknown object extends beyond the reference Airy disk of the hologram, then higher spatial frequency information about the unknown object is recorded in the hologram - although it cannot be accessed using Fourier transform reconstruction alone. However, this information can be recovered using iterative phase retrieval algorithms on the oversampled diffraction pattern or hologram [22,48,123,129,130,138,139]. This allows further improvement of the reconstructed image resolution. As stated earlier, over a cumulative 4800 s exposure, measurable signal in the diffracted light was observed out to a 29° diffracted angle (momentum transfer of 0.211 nm^{-1}), corresponding to a potential image resolution of 30 nm. The measured diffraction pattern was preprocessed first by removing cosmic X-rays and subtracting the background. Following summation of the separate 600 s exposures the cumulative diffraction pattern was curvature-corrected. To maximize the signal-to-noise ratio of the diffraction pattern while maintaining the oversampling, the data were binned into 3 X 3 pixel blocks. Next, the entire pattern was deconvolved with a sinc kernel in real space to compensate for the finite pixel size of the CCD detector [20, 47, 109].

Following this preprocessing, the iterative algorithm is applied to enhance the resolution. First an initial rectangular loose support is estimated from the oversampling ratio. With this loose support, 16 independent reconstructions are computed with the guided hybrid input and output algorithm (GHIO) [20,47,104,109]. Each reconstruction starts with a random phase set as the initial input and is iterated back and forth between real and reciprocal space. In real space the electron density outside the support and negative density inside the support are slowly pushed to zero. In reciprocal space, the measured Fourier modulus (i.e. the square root of the diffraction intensity) is updated in each iteration. After 2000 iterations, 16 images are reconstructed, defined as the 0th generation. An R-factor is calculated for each image, i.e. the difference between the calculated Fourier transform modulus from the image and the measured diffraction

pattern modulus. A seed for the next generation is chosen by selecting the image with the lowest R-factor. By multiplying the seed with each of the 16 images and taking the square root of the product, we obtain a new set of 16 images, which is used as the initial input for the next generation. This process is repeated through 9 generations. After the final generation, the best seeds are averaged and a new tighter support was determined. With this new tight support, the diffraction pattern is again submitted to the GHIO reconstruction process, this time yielding the final image with a substantially improved resolution of 53 nm, as illustrated in Figure 5.7.

Figure 5.7 (a) shows a scanning electron microscope image of the FT holography sample. Figure 5.7 (b) shows the preprocessed, curvature corrected hologram from a composite 4800 s exposure that was used in the iterative phase retrieval. Figure 5.7 (c) shows the final reconstruction of the sample, demonstrating 53 nm resolution as shown by the lineout along the dashed blue line (shown in Figure 5.7 (d)).

This holography/oversampling phase retrieval hybrid technique has several notable advantages. First, while image recovery using phase retrieval takes tens of hours of processor time, reconstruction using the FTH method takes only seconds. Thus the holographic/oversampling phase retrieval hybrid technique allows quick feedback on low resolution information, with the possibility of further improving the resolution to the limit set by wavelength, numerical aperture, and signal-to-noise via phase retrieval. Also, as pointed out previously, the reference holes in Fourier transform holography break the symmetry of the phase retrieval problem, allowing for higher image quality and quicker convergence [123, 130]. This technique also eases the requirement for small reference features that are difficult to manufacture.

5.4 Conclusion

In conclusion, we have introduced a practical diffractive soft x-ray microscopy system capable of fast feedback, high resolution imaging (near 50 nm) using Fourier

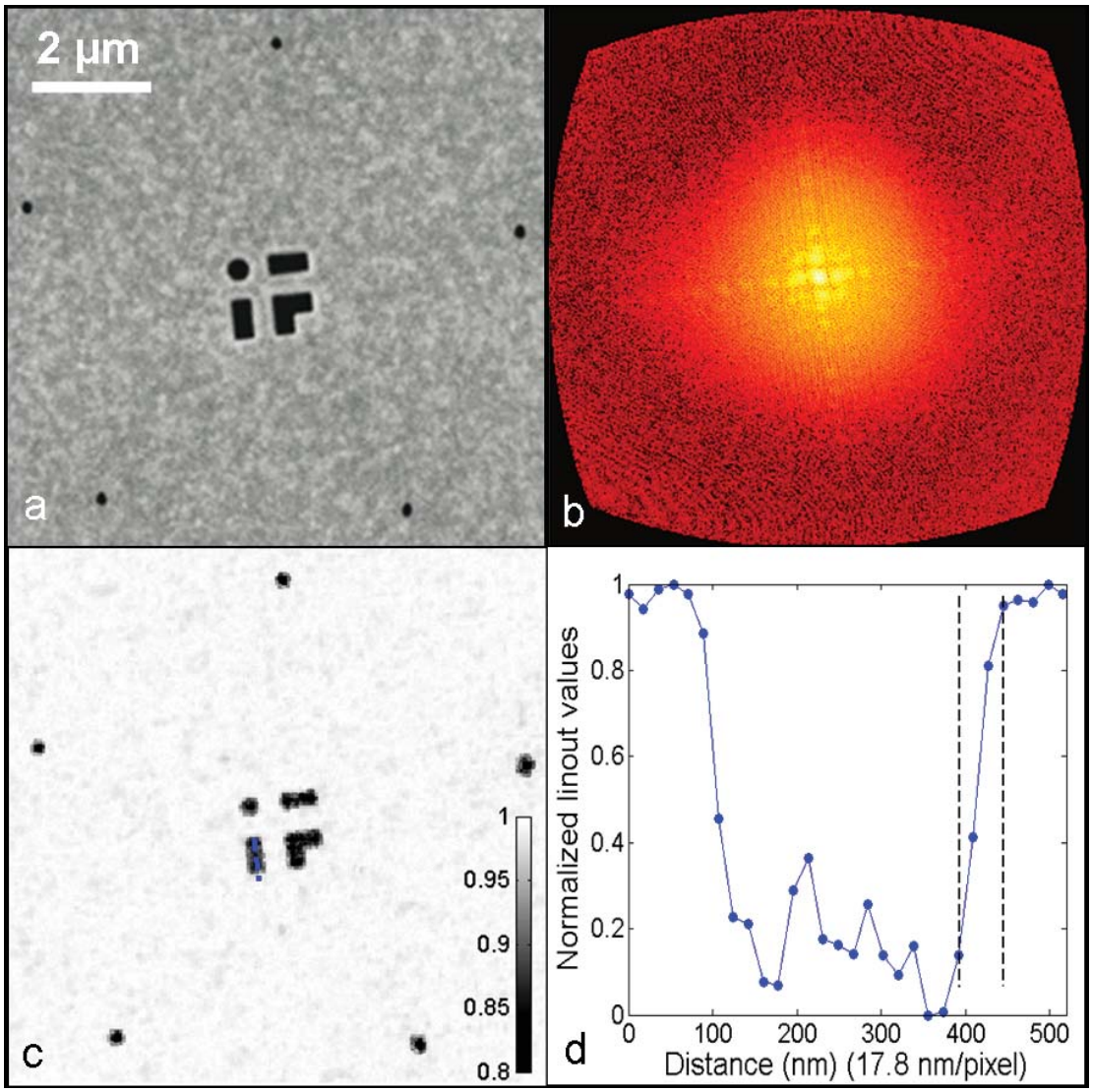

Figure 5.7: (a) Scanning electron microscope image of the five-reference-hole sample. (b) Log of the curvature corrected hologram used in the iterative phase retrieval (maximum momentum transfer of $Q_{max} = \pm 0.211$ nm^{-1}). (c) Reconstructed image of the sample using the GHIO phase retrieval algorithm to refine the resolution to 53 nm, as demonstrated in the lineout (blue dotted line) shown in (d) [26].

transform holography. All of the data presented are from a tabletop soft x-ray source and demonstrate that high numerical aperture (NA >0.5) coherent diffractive imaging is practical. By combining oversampling iterative phase retrieval with Fourier transform holography, we achieve near wavelength-limited 53 nm resolution using 29 nm light, thus demonstrating the highest numerical aperture x-ray holography to date. Moreover, good resolution images are possible with exposure times of only 30 s. This work represents a significant step forward over past work, and uses ultrafast laser systems that are available in many laboratories worldwide.

In the future, new phase matching schemes promise to increase the high harmonic flux at short wavelengths down to $\sim$ 1 nm, for applications in ultrafast biological and materials imaging on the nanometer scale as well as a wide range of applications in chemical and materials spectroscopies. Because FT holography is photon efficient, it is an ideal imaging scheme to use with high harmonic sources, particularly when combined with phase retrieval to achieve the highest spatial resolution. Finally, since these diffractive imaging schemes can exploit the ultrafast pulse duration capability of high harmonic generation, time resolved coherent imaging will be possible in the future with simultaneously high spatial and temporal resolution.

Chapter 6

Outlook: Future developments and applications

This dissertation has demonstrated that tabletop x-ray coherent diffractive imaging is possible at high resolution ($\sim$ 50 nm). It has demonstrated that high harmonic generation (HHG) is a compact, bright, and extremely coherent source of EUV/SXR radiation. Additionally, tabletop soft x-ray lasers, although not as coherent as HHG, can be spatially filtered to provide very bright coherent sources. Both of these sources were used in the first demonstrations of tabletop x-ray coherent diffractive imaging (XCDI) or lensless imaging. This section will review the future developments that will need to take place to truly make this microscope useful and some of the suggested applications for such a technique.

6.1 Future directions: a practical tabletop water window microscope

While these demonstrations are compelling, a practical tabletop coherent x-ray microscope will need to access shorter wavelengths (higher photon energies) in the 1-6 nm range (200-1000 eV). These wavelengths are not absorbed as strongly as the 30-50 nm range thus making imaging of thicker samples or even three dimensional tomography possible. We have already discussed in section 2.5 that SXR lasers have a punishing pump power scaling of $1/\lambda^4$, thus accessing these short wavelengths on tabletop SXR laser sources will be difficult [6]. Therefore, it is hoped that HHG will scale to usable

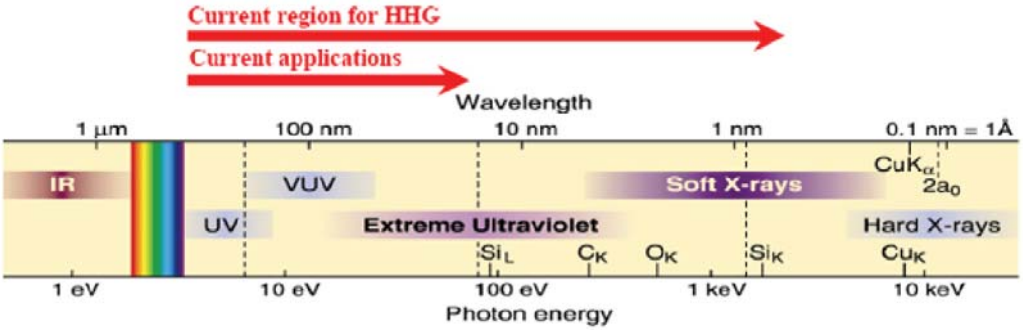

Figure 6.1: Current and future region where HHG may be a useful tabletop source of x-rays (adapted from Attwood [6] courtesy of M. Murnane).

wavelengths in the single nm wavelength range. Figure 6.1 shows the region in which HHG produces flux levels that make scientific or technological applications possible currently ($\sim$ 1 μW), and where HHG has potential for useful flux levels through the development of higher repetition rate lasers and better nonlinear optics. This section will discuss some preliminary work conducted at repeating these results at the 13.5 nm wavelength under the direction of fellow graduate student Daisy Raymondson. Then it will also discuss pathways towards useful water window imaging with HHG.

6.1.1 Recent developments at 13 nm

Section 2.3 described how HHG is a very tunable source of coherent SXR radiation. Our group previously demonstrated that helium can be phase matched to produce narrow divergence 13.5 nm x-rays [125], however imaging at this wavelength has not been demonstrated by our group. HHG from a helium gas jet has been used in a zone plate imaging configuration to achieve 200 nm resolution elsewhere, but imaging with 13.5 nm at sub-100 nm resolutions with HHG has yet to be achieved [55]. One potential reason is that available photon flux at 13.5 nm from helium is about 20 times less than 29 nm flux from argon due to the re-absorption of harmonic radiation in helium. This added absorption comes from, among other factors, the fact that helium is phase

matched at about 400 torr of pressure compared to phase matched argon at about 50 torr of pressure. The 13.5 nm wavelength has extremely important technological implications because of the development of extreme ultraviolet lithography (EUVL) for the semiconductor industry at that wavelength [6, 35]. Thus, if high resolution imaging (<50 nm) at 13.5 nm can be demonstrated on a high repetition rate tabletop source, it could have important applications in EUVL mask and mirror blank defect inspection.

Daisy Raymondson has demonstrated preliminary image resolutions down to 70 nm resolutions (see Daisy A. Raymondson Dissertation and forthcoming articles). She uses the same laser setup described in chapter 4, but focuses the fs laser pulses into a 100 μm diameter waveguide and phase matches in helium at a pressure of about 400 torr. Some preliminary data using FT holography with $\sim$ 200 nm reference holes is shown in figure 6.2. This result demonstrates approximately 184 nm resolution in 40 minutes of exposure. Additionally, Raymondson is working on higher repetition rate lasers (15 kHz instead of 3 kHz) that could increase the available 13.5 nm flux by a factor of 5 or more. With improved nonlinear optics, higher repetition rate lasers, and higher through put optical/harmonic discrimination schemes, 13.5 nm imaging with HHG may be able to achieve the same resolution-to-wavelength ratio as described in chapters 4 and 5, making sub-30 nm resolutions practical.

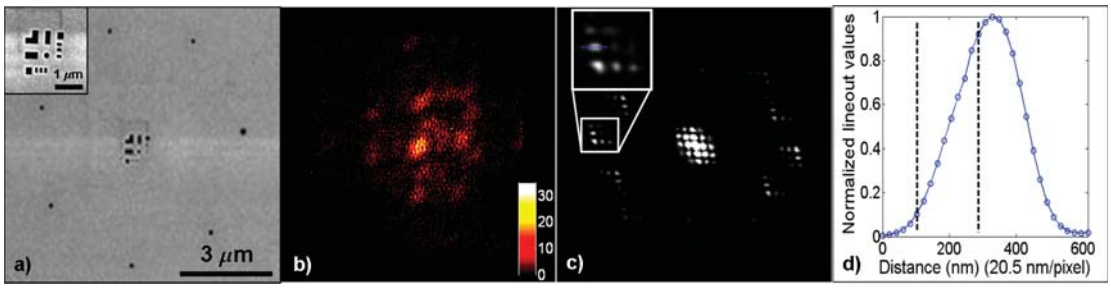

Figure 6.2: Preliminary results of 13 nm Fourier transform holography: (a) SEM image of FT holography sample with seven reference holes (b) 13.5 nm hologram from 40 minute exposure (log scale) (c) autocorrelation reconstruction of the sample (d) line cut through one sub-image showing 184 nm resolution [27].

6.1.2 Pathways to usable water window

Another potentially very large application of tabletop XCDI is biological imaging in the water window (between 284 eV and 543 eV) [6]. It has been said that one of the reasons x-ray water window imaging has not found broader applications in biology is that biologists do not want to have to take their laboratories to synchrotrons for imaging. Therefore, a tabletop source of coherent water window radiation source could achieve much broader application in the biological community. However, as discussed in section 2.3, HHG cannot be phase matched through traditional methods at these photon energies with driving laser wavelengths of 800 nm due to the high levels of ionization [87, 90]. Quasi-phase matching has been demonstrated with HHG up to photon energies of about 200 eV ($\sim$ 6 nm) but not yet into the water window [62,85,87,140]. However, Tenio Popmintchev and colleagues in our group have recently demonstrated phase matched water window generation with mid-IR driving wavelengths (1.4 μm) [66]. This is possible due to the lower ionization levels that occur when using mid-IR wavelengths. Currently efforts are underway to measure the coherence and demonstrate coherent imaging with this source. Therefore, biological tabletop water window XCDI looks very possible in the next two to three years.

6.2 Summary and outlook

This section has shown that the tabletop XCDI demonstrations from this dissertation have many potential applications to biology and materials science and technology. Water window biological imaging and EUVL metrology are only two of these that should be realized in coming years. With the development of new phase matching and quasi-phase matching techniques, better lasers, and better management of the harmonic light there is real possibility to have bright, coherent SXR radiation up to 1 keV ($\sim$ 1 nm). Additionally, XCDI with HHG may open a whole new field of tabletop ultrafast x-ray

imaging with femtosecond to attosecond resolution. Already efforts are underway in our group to repeat Ra'anan Tobey and Mark Siemens' work of studying the photoacoustic properties of thin films in imaging mode [141]. Additional time resolved studies will begin soon on magnetic materials. This may open the door to femtosecond dynamic studies of magnetic thin films with photon energies $\sim$ 800 eV and at resolutions approaching $<$10 nm [48, 142]. Thus, many interesting applications are already waiting for tabletop XCDI with HHG as soon as the SXR flux becomes available.

Bibliography

[1] S. W. Hell, "Far-field optical nanoscopy," Science, vol. 316, no. 5828, pp. 1153–1158, 2007.

[2] S. M. Hurtley and L. Helmuth, "The future looks bright," Science, vol. 300, no. 5616, p. 75, 2003.

[3] M. G. L. Gustafsson, "Nonlinear structured-illumination microscopy: Wide-field fluorescence imaging with theoretically unlimited resolution," Proceedings of the National Academy of Sciences of the United States of America, vol. 102, no. 37, pp. 13 081–13 086, 2005.

[4] R. L. Sandberg, A. Paul, D. A. Raymondson, S. Hadrich, D. M. Gaudiosi, J. Holtsnider, R. I. Tobey, O. Cohen, M. M. Murnane, H. C. Kapteyn, C. Song, J. Miao, Y. Liu, and F. Salmassi, "Lensless diffractive imaging using tabletop coherent high-harmonic soft-x-ray beams," Phys Rev Lett, vol. 99, no. 9, p. 098103.

[5] R. L. Sandberg, C. Song, P. W. Wachulak, D. A. Raymondson, A. Paul, B. Amirbekian, E. Lee, A. E. Sakdinawat, O. V. C. La, M. C. Marconi, C. S. Menoni, M. M. Murnane, J. J. Rocca, H. C. Kapteyn, and J. Miao, "High numerical aperture tabletop soft x-ray diffraction microscopy with 70-nm resolution," Proc Natl Acad Sci U S A, vol. 105, no. 1, pp. 24–7.

[6] D. Attwood, Soft X-Rays and Extreme Ultraviolet Radiation: Principles and Applications. Cambridge University Press, 2007.

[7] D. Müller, S. Backus, K. Read, M. Murnane, and H. Kapteyn, "Very high-peak-power lasers cryogenic cooling multiplies ti: sapphire output," Laser Focus World, vol. 41, no. 10, p. 65, 2005.

[8] "Kmlabs®." [Online]. Available: http://www.kmlabs.com

[9] X. F. Li, A. LHuillier, M. Ferray, L. A. Lompr, and G. Mainfray, "Multiple-harmonic generation in rare gases at high laser intensity," Physical Review A, vol. 39, no. 11, p. 5751.

[10] J. L. Krause, K. J. Schafer, and K. C. Kulander, "High-order harmonic generation from atoms and ions in the high intensity regime," Physical Review Letters, vol. 68, no. 24, p. 3535.

[11] P. B. Corkum, "Plasma perspective on strong field multiphoton ionization," Physical Review Letters, vol. 71, no. 13, p. 1994.

[12] H. C. Kapteyn, M. M. Murnane, and I. P. Christov, "Extreme nonlinear optics: coherent x rays from lasers," Phys. Today, vol. 58, no. 3, pp. 39–46, 2005.

[13] T. Brabec and F. Krausz, "Intense few-cycle laser fields: Frontiers of nonlinear optics," Reviews of Modern Physics, vol. 72, no. 2, pp. 545–591, 2000.

[14] A. R. Rundquist, "Phase-matched generation of coherent, ultrafast x-rays using high harmonics," Ph.D. dissertation, Washington State University, 1998.

[15] W. F. Schlotter, "Lensless fourier transform holography with soft x-rays," PhD Dissertation, Stanford University, 2007.

[16] R. A. Bartels, A. Paul, M. M. Murnane, H. C. Kapteyn, S. Backus, Y. Liu, and D. T. Attwood, "Absolute determination of the wavelength and spectrum of an extreme-ultraviolet beam by a young's double-slit measurement," Opt. Lett., vol. 27, no. 9, pp. 707–709, 2002.

[17] R. A. Bartels, A. Paul, H. Green, H. C. Kapteyn, M. M. Murnane, S. Backus, I. P. Christov, Y. Liu, D. Attwood, and C. Jacobsen, "Generation of spatially coherent light at extreme ultraviolet wavelengths," Science, vol. 297, no. 5580, pp. 376–8.

[18] J. Peatross and M. Ware, "Physics of light and optics," 2008, http://optics.byu.edu/textbook.aspx.

[19] J. R. Fienup, "Reconstruction of an object from the modulus of its fourier transform," Opt. Lett, vol. 3, no. 1, pp. 27–29, 1978.

[20] C. Song, D. Ramunno-Johnson, Y. Nishino, Y. Kohmura, T. Ishikawa, C. C. Chen, T. K. Lee, and J. Miao, "Phase retrieval from exactly oversampled diffraction intensity through deconvolution," Physical Review B, vol. 75, no. 1, p. 12102, 2007.

[21] P. Thibault, M. Dierolf, A. Menzel, O. Bunk, C. David, and F. Pfeiffer, "High-resolution scanning x-ray diffraction microscopy," Science, vol. 321, no. 5887, pp. 379–382, 2008.

[22] B. Abbey, K. A. Nugent, G. J. Williams, J. N. Clark, A. G. Peele, M. A. Pfeifer, M. de Jonge, and I. McNulty, "Keyhole coherent diffractive imaging," Nat Phys, vol. 4, no. 5, pp. 394–398.

[23] S. Marchesini, H. Chapman, S. Hau-Riege, R. London, A. Szoke, H. He, M. Howells, H. Padmore, R. Rosen, and J. Spence, "Coherent x-ray diffractive imaging: applications and limitations," Optics Express, vol. 11, no. 19, pp. 2344–2353, 2003.

[24] A. J. Paul, "Coherent euv light from high-order harmonic generation: Enhancement and applications to lensless diffractive imaging," PhD Dissertation, University of Colorado at Boulder, 2007. [Online]. Available: http://jilawww.colorado.edu/pubs/thesis/paul_ariel/paul_thesis.pdf

[25] "Quantifoil®holey carbon films." [Online]. Available: http://www.quanitfoil.com

[26] R. L. Sandberg, D. A. Raymondson, C. La-o vorakiat, A. Paul, K. J. Raines, J. Miao, M. M. Murnane, H. C. Kapteyn, and W. F. Schlotter, "Tabletop soft x-ray fourier transform holography with 50 nm resolution," Optics Letters, 2009 (in press).

[27] R. L. Sandberg, D. A. Raymondson, W. F. Schlotter, K. J. Raines, C. La-o vorakiat, A. Paul, M. M. Murnane, H. C. Kapteyn, and J. Miao, "Near diffraction limited coherent diffractive imaging with tabletop soft x-ray sources," Journal of Physics: Conference Series (Proceedings of the Conference on X-ray Microscopy), 2008 (in review).

[28] R. Hooke, Micrographia. Courier Dover Publications, 2003 (Original year 1665).

[29] R. J. Oldfield, Light Microscopy: An Illustrated Guide. CV Mosby, 1994.

[30] E. Abbe, "Beiträge zur theorie des mikroskops und der mikroskopischen wahrnehmung," SPIE milestone series, vol. 178, pp. 12–24, 2004 (Original 1873).

[31] E. Abbe, Gesammelte Abhandlungen. Jena: G. Fischer, 1904.

[32] M. Spencer, Fundamentals of Light Microscopy. Cambridge University Press, 1982.

[33] M. Parry-Hill and M. W. Davidson, "Microscope objectives: Immersion oil and refractive index," 2008 11 22 2008. [Online]. Available: http://www.microscopyu.com/

[34] J. J. Cargille, "Immersion oil and the microscope," 2008 11 22 1985.

[35] H. J. Levinson, Principles of Lithography. SPIE Press, 2005.

[36] M. W. Davidson, "Microscope objectives: Immersion oil and refractive index," 2008 11 24 2008. [Online]. Available: http://www.microscopyu.com/

[37] W. A. Hofer, A. S. Foster, and A. L. Shluger, "Theories of scanning probe microscopes at the atomic scale," Reviews of Modern Physics, vol. 75, no. 4, p. 1287.

[38] "Nobel prize website." [Online]. Available: http://nobelprize.org/nobel_prizes

[39] B. Bailey, D. L. Farkas, D. L. Taylor, and F. Lanni, "Enhancement of axial resolution in fluorescence microscopy by standing-wave excitation," Nature, vol. 366, no. 6450, pp. 44–48.

[40] M. G. L. Gustafsson, "Surpassing the lateral resolution limit by a factor of two using structured illumination microscopy," Journal of Microscopy, vol. 198, no. 2, pp. 82–87, 2000.

[41] J. C. H. Spence, Experimental high-resolution electron microscopy. Oxford University Press, 1988.

[42] W. Meyer-Ilse, D. Hamamoto, A. Nair, S. A. Lelievre, G. Denbeaux, L. Johnson, A. L. Pearson, D. Yager, M. A. Legros, and C. A. Larabell, "High resolution protein localization using soft x-ray microscopy," Journal of Microscopy, vol. 201, no. 3, pp. 395–403, 2001.

[43] S. B. McLane, E. W. Mller, and O. Nishikawa, "Field ion microscopy with an external image intensifier," Review of Scientific Instruments, vol. 35, p. 1297, 2004.

[44] L. A. Giannuzzi and F. A. Stevie, "A review of focused ion beam milling techniques for tem specimen preparation," Micron, vol. 30, no. 3, pp. 197–204, 1999.

[45] C. A. Larabell and M. A. Le Gros, "X-ray tomography generates 3-d reconstructions of the yeast, saccharomyces cerevisiae, at 60-nm resolution," Mol Biol Cell, vol. 15, no. 3, pp. 957–62.

[46] G. Meier, M. Bolte, R. Eiselt, B. Krger, D. Kim, and P. Fischer, "Direct imaging of stochastic domain-wall motion driven by nanosecond current pulses," Physical Review Letters, vol. 98, 2007.

[47] J. Miao, T. Ishikawa, T. Earnest, and Q. Shen, "Extending the methodology of x-ray crystallography to allow structure determination of non-crystalline materials, whole cells and single macromolecular complexes," Annu. Rev. Phys. Chem., vol. 59, p. 387, 2008.

[48] S. Eisebitt, J. Lüning, W. F. Schlotter, M. Lörgen, O. Hellwig, W. Eberhardt, and J. Stöhr, "Lensless imaging of magnetic nanostructures by x-ray spectroholography," Nature(London), vol. 432, no. 7019, pp. 885–888, 2004.

[49] W. Chao, B. D. Harteneck, J. A. Liddle, E. H. Anderson, and D. T. Attwood, "Soft x-ray microscopy at a spatial resolution better than 15 nm," Nature, vol. 435, no. 7046, pp. 1210–1213, 2005.

[50] J. Miao, P. Charalambous, J. Kirz, and D. Sayre, "Extending the methodology of x-ray crystallography to allow imaging of micrometer-sized non-crystalline specimens," Nature, vol. 400, p. 342, 1999.

[51] H. N. Chapman, A. Barty, M. J. Bogan, S. Boutet, M. Frank, S. P. Hau-Riege, S. Marchesini, B. W. Woods, S. Bajt, W. H. Benner, R. A. London, E. Plonjes, M. Kuhlmann, R. Treusch, S. Dusterer, T. Tschentscher, J. R. Schneider, E. Spiller, T. Moller, C. Bostedt, M. Hoener, D. A. Shapiro, K. O. Hodgson, D. van der Spoel, F. Burmeister, M. Bergh, C. Caleman, G. Huldt, M. M. Seibert, F. R. N. C. Maia, R. W. Lee, A. Szoke, N. Timneanu, and J. Hajdu, "Femtosecond diffractive imaging with a soft-x-ray free-electron laser," Nat Phys, vol. 2, no. 12, pp. 839–843.

[52] S. Marchesini, H. He, H. N. Chapman, S. P. Hau-Riege, A. Noy, M. R. Howells, U. Weierstall, and J. C. H. Spence, "X-ray image reconstruction from a diffraction pattern alone," Physical Review B, vol. 68, no. 14, p. 140101, 2003.

[53] D. Shapiro, P. Thibault, T. Beetz, V. Elser, M. Howells, C. Jacobsen, J. Kirz, E. Lima, H. Miao, A. M. Neiman, and D. Sayre, "Biological imaging by soft x-ray diffraction microscopy," Proceedings of the National Academy of Sciences of the United States of America, vol. 102, no. 43, pp. 15 343–15 346, 2005.

[54] G. Vaschenko, C. Brewer, F. Brizuela, Y. Wang, M. A. Larotonda, B. M. Luther, M. C. Marconi, J. J. Rocca, C. S. Menoni, and E. H. Anderson, "Sub-38nm resolution tabletop microscopy with 13nm wavelength laser light," Optics Letters, vol. 31, no. 9, pp. 1214–1216, 2006.

[55] M. Wieland, C. Spielmann, U. Kleineberg, T. Westerwalbesloh, U. Heinzmann, and T. Wilhein, "Toward time-resolved soft x-ray microscopy using pulsed fs-high-harmonic radiation," Ultramicroscopy, vol. 102, no. 2, pp. 93–100.

[56] P. W. Wachulak, R. A. Bartels, M. C. Marconi, C. S. Menoni, J. J. Rocca, Y. Lu, and B. Parkinson, "Sub 400 nm spatial resolution extreme ultraviolet holography with a table top laser," Optics Express, vol. 14, no. 21, pp. 9636–9642, 2006.

[57] P. W. Wachulak, M. C. Marconi, R. A. Bartels, C. S. Menoni, and J. J. Rocca, "Soft x-ray laser holography with wavelength resolution," J. Opt. Soc. Am. B, vol. 25, no. 11, pp. 1811–1814.

[58] Y. Wang, E. Granados, F. Pedaci, D. Alessi, B. Luther, M. Berrill, and J. J. Rocca, "Phase-coherent, injection-seeded, table-top soft-x-ray lasers at 18.9 nm and 13.9 nm," Nature Photonics, vol. 2, no. 2, pp. 94–98.

[59] C. Spielmann, N. H. Burnett, S. Sartania, R. Koppitsch, M. Schnurer, C. Kan, M. Lenzner, P. Wobrauschek, and F. Krausz, "Generation of coherent x-rays in the water window using 5-femtosecond laser pulses," Science, vol. 278, no. 5338, pp. 661–664, 1997.

[60] Z. Chang, A. Rundquist, H. Wang, M. M. Murnane, and H. C. Kapteyn, "Generation of coherent soft x rays at 2.7 nm using high harmonics," Physical Review Letters, vol. 79, no. 16, pp. 2967–2970, 1997.

[61] J. Seres, E. Seres, A. J. Verhoef, G. Tempea, C. Streli, P. Wobrauschek, V. Yakovlev, A. Scrinzi, C. Spielmann, and F. Krausz, "Laser technology: Source of coherent kiloelectronvolt x-rays," Nature, vol. 433, no. 7026, pp. 596–596.

[62] X. Zhang, A. L. Lytle, T. Popmintchev, X. Zhou, H. C. Kapteyn, M. M. Murnane, and O. Cohen, "Quasi-phase-matching and quantum-path control of high-harmonic generation using counterpropagating light," Nature Physics, vol. 3, pp. 270–275, 2007.

[63] M. Zepf, B. Dromey, M. Landreman, P. Foster, and S. M. Hooker, "Bright quasi-phase-matched soft-x-ray harmonic radiation from argon ions," Physical Review Letters, vol. 99, no. 14.

[64] J. Seres, V. S. Yakovlev, E. Seres, C. Streli, P. Wobrauschek, C. Spielmann, and F. Krausz, "Coherent superposition of laser-driven soft-x-ray harmonics from successive sources," Nat Phys, vol. 3, no. 12, pp. 878–883.

[65] A. L. Lytle, X. Zhang, P. Arpin, O. Cohen, M. M. Murnane, and H. C. Kapteyn, "Quasi-phase matching of high-order harmonic generation at high photon energies using counterpropagating pulses," Optics Letters, vol. 34, p. 174, 2008.

[66] T. Popmintchev, M.-C. Chen, O. Cohen, M. E. Grisham, J. J. Rocca, M. M. Murnane, and H. C. Kapteyn, "Extended phase matching of high harmonics driven by mid-infrared light," Opt. Lett., vol. 33, no. 18, pp. 2128–2130, 2008.

[67] S. Backus, C. G. Durfee Iii, M. M. Murnane, and H. C. Kapteyn, "High power ultrafast lasers," Review of Scientific Instruments, vol. 69, p. 1207, 1998.

[68] T. H. Maiman, "Stimulated optical radiation in ruby," Nature, vol. 187, no. 4736, pp. 493–494, 1960.

[69] P. A. Franken, A. E. Hill, C. W. Peters, and G. Weinreich, "Generation of optical harmonics," Physical Review Letters, vol. 7, no. 4, pp. 118–119, 1961.

[70] D. E. Spence, P. N. Kean, and W. Sibbett, Optics Letters, vol. 16, p. 42, 1991.

[71] I. P. Christov, M. M. Murnane, and H. C. Kapteyn, "High-harmonic generation of attosecond pulses in the single-cycle regime," Physical Review Letters, vol. 78, no. 7, pp. 1251–1254, 1997.

[72] M. Hentschel, R. Kienberger, C. Spielmann, G. A. Reider, N. Milosevic, T. Brabec, P. Corkum, U. Heinzmann, M. Drescher, and F. Krausz, "Attosecond metrology," Nature, vol. 414, no. 6863, pp. 509–513.

[73] E. Goulielmakis, M. Schultze, M. Hofstetter, V. S. Yakovlev, J. Gagnon, M. Uiberacker, A. L. Aquila, E. M. Gullikson, D. T. Attwood, R. Kienberger, F. Krausz, and U. Kleineberg, "Single-cycle nonlinear optics," Science, vol. 320, no. 5883, pp. 1614–1617, 2008.

[74] M. M. Murnane, H. C. Kapteyn, M. D. Rosen, and R. W. Falcone, "Ultrafast X-ray Pulses from Laser-Produced Plasmas," Science, vol. 251, no. 4993, pp. 531–536.

[75] J. J. Rocca, V. Shlyaptsev, F. G. Tomasel, O. D. Cortzar, D. Hartshorn, and J. L. A. Chilla, "Demonstration of a discharge pumped table-top soft-x-ray laser," Physical Review Letters, vol. 73, no. 16, p. 2192.

[76] F. Zernike and J. E. Midwinter, Applied nonlinear optics. Wiley New York, 1973.

[77] A. McPherson, G. Gibson, H. Jara, U. Johann, T. S. Luk, I. A. McIntyre, K. Boyer, and C. K. Rhodes, "Studies of multiphoton production of vacuum-ultraviolet radiation in the rare gases," J. Opt. Soc. Am. B, vol. 4, no. 4, pp. 595–601, 1987.

[78] L. V. Keldysh, "Ionization in the field of a strong em wave," Sov. Phys. JETP, vol. 20, p. 13071314, 1965.

[79] M. Ammosov, N. Delone, and p. . Krainov, V.P. 64 (1986), "Tunnel ionization of complex atoms and of atomic ions in an alternating electromagnetic field," Soviet Phys. JETP, vol. 64, no. 6, pp. 1191–1194, 1986.

[80] M. Lewenstein, P. Balcou, M. Y. Ivanov, A. LHuillier, and P. B. Corkum, "Theory of high-harmonic generation by low-frequency laser fields," Physical Review A, vol. 49, no. 3, p. 2117.

[81] P. Balcou and A. LHuillier, "Phase-matching effects in strong-field harmonic generation," Physical Review A, vol. 47, no. 2, p. 1447.

[82] A. Rundquist, C. G. Durfee Iii, Z. Chang, C. Herne, S. Backus, M. M. Murnane, and H. C. Kapteyn, "Phase-matched generation of coherent soft x-rays," Science, vol. 280, no. 5368, p. 1412, 1998.

[83] C. G. Durfee III, A. R. Rundquist, S. Backus, C. Herne, M. M. Murnane, and H. C. Kapteyn, "Phase matching of high-order harmonics in hollow waveguides," Physical Review Letters, vol. 83, no. 11, pp. 2187–2190, 1999.

[84] I. Christov, H. Kapteyn, and M. Murnane, "Quasi-phase matching of high-harmonics and attosecond pulses in modulated waveguides," Opt. Express, vol. 7, no. 11, pp. 362–367, 2000.

[85] A. Paul, R. A. Bartels, R. Tobey, H. Green, S. Weiman, I. P. Christov, M. M. Murnane, H. C. Kapteyn, and S. Backus, "Quasi-phase-matched generation of coherent extreme-ultraviolet light," Nature, vol. 421, no. 6918, pp. 51–54, 2003.

[86] J. Peatross, S. Voronov, and I. Prokopovich, "Selective zoning of high harmonic emission using counter-propagating light," Optics Express, vol. 1, no. 5, pp. 114–125, 1997.

[87] A. L. Lytle, X. Zhang, R. L. Sandberg, O. Cohen, H. C. Kapteyn, and M. M. Murnane, "Quasi-phase matching and characterization of high-order harmonic generation in hollow waveguides using counterpropagating light," Optics Express, vol. 16, no. 9, pp. 6544–6566, 2008.

[88] P. Salières, A. L'Huillier, and M. Lewenstein, "Coherence control of high-order harmonics," Physical Review Letters, vol. 74, no. 19, p. 3776.

[89] T. Ditmire, E. T. Gumbrell, R. A. Smith, J. W. G. Tisch, D. D. Meyerhofer, and M. H. R. Hutchinson, "Spatial coherence measurement of soft x-ray radiation produced by high order harmonic generation," Physical Review Letters, vol. 77, no. 23, p. 4756.

[90] A. L. Lytle, "Phase matching and coherence of high-order harmonic generation in hollow waveguides," PhD Dissertation, University of Colorado at Boulder, 2008. [Online]. Available: http://jilawww.colorado.edu/pubs/thesis/lytle_amy/lytle_thesis.pdf

[91] M. Wieland, R. Frueke, T. Wilhein, C. Spielmann, M. Pohl, and U. Kleineberg, "Submicron extreme ultraviolet imaging using high-harmonic radiation," Applied Physics Letters, vol. 81, p. 2520, 2002.

[92] R. Bartels, S. Backus, E. Zeek, L. Misoguti, G. Vdovin, I. P. Christov, M. M. Murnane, and H. C. Kapteyn, "Shaped-pulse optimization of coherent emission of high-harmonic soft x-rays," Nature, vol. 406, no. 6792, pp. 164–166.

[93] T. Wilhein, S. Rehbein, D. Hambach, M. Berglund, L. Rymell, and H. M. Hertz, "A slit grating spectrograph for quantitative soft x-ray spectroscopy," Review of Scientific Instruments, vol. 70, p. 1694, 1999.

[94] P. A. C. Takman, H. Stollberg, G. A. Johansson, A. Holmberg, M. Lindblom, and H. M. Hertz, "High-resolution compact x-ray microscopy," Journal of Microscopy, vol. 226, no. 2, pp. 175–181.

[95] J. J. Rocca, "Table-top soft x-ray lasers," Review of Scientific Instruments, vol. 70, no. 10, pp. 3799–3827.

[96] Y. Liu, M. Seminario, F. G. Tomasel, C. Chang, J. J. Rocca, and D. T. Attwood, "Achievement of essentially full spatial coherence in a high-average-power soft-x-ray laser," Physical Review A, vol. 63, no. 3, p. 033802.

[97] C. A. Brewer, F. Brizuela, P. Wachulak, D. H. Martz, W. Chao, E. H. Anderson, D. T. Attwood, A. V. Vinogradov, I. A. Artyukov, and A. G. Ponomareko, "Single-shot extreme ultraviolet laser imaging of nanostructures with wavelength resolution," Optics Letters, vol. 33, no. 5, pp. 518–520, 2008.

[98] Y. Wang, M. A. Larotonda, B. M. Luther, D. Alessi, M. Berrill, V. N. Shlyaptsev, and J. J. Rocca, "Demonstration of high-repetition-rate tabletop soft-x-ray lasers with saturated output at wavelengths down to 13.9 nm and gain down to 10.9 nm," Physical Review A (Atomic, Molecular, and Optical Physics), vol. 72, no. 5, p. 053807.

[99] K. J. Schafer and K. C. Kulander, "High harmonic generation from ultrafast pump lasers," Physical Review Letters, vol. 78, no. 4, p. 638.

[100] J. W. Goodman, Introduction to Fourier Optics, Second Edition. Boston: McGraw Hill, 1996.

[101] D. Sayre, "Some implications of a theorem due to shannon," Acta Crystallographica, vol. 5, no. 6, pp. 843–843, 1952.

[102] J. Miao and D. Sayre, "On possible extensions of x-ray crystallography through diffraction-pattern oversampling," Acta Crystallographica Section A, vol. 56, no. 6, pp. 596–605, 2000.

[103] J. D. Watson and F. H. C. Crick, "Molecular structure of nucleic acids: A structure for deoxyribose nucleic acid," Nature, vol. 171, no. 4356, pp. 737–738.

[104] J. Miao, D. Sayre, and H. N. Chapman, "Phase retrieval from the magnitude of the fourier transforms of nonperiodic objects," Journal of the Optical Society of America A, vol. 15, no. 6, pp. 1662–1669, 1998.

[105] J. Miao, T. Ishikawa, E. H. Anderson, and K. O. Hodgson, "Phase retrieval of diffraction patterns from noncrystalline samples using the oversampling method," Physical Review B, vol. 67, no. 17, p. 174104.

[106] J. R. Fienup, "Reconstruction of a complex-valued object from the modulus of its fourier transform using a support constraint," Optical Society of America, Journal, A: Optics and Image Science, vol. 4, pp. 118–123, 1987.

[107] R. W. Gerchberg and W. O. Saxton, "Practical algorithm for determination of phase from image and diffraction plane pictures," Optik, vol. 35, no. 2, pp. 237–&.

[108] S. Marchesini, "Invited article: A unified evaluation of iterative projection algorithms for phase retrieval," Review of Scientific Instruments, vol. 78, no. 1, p. 011301.

[109] C. C. Chen, J. Miao, C. W. Wang, and T. K. Lee, "Application of optimization technique to noncrystalline x-ray diffraction microscopy: Guided hybrid input-output method," Physical Review B, vol. 76, no. 6, p. 64113, 2007.

[110] R. Trebino, Frequency-Resolved Optical Gating: The Measurement of Ultrashort Laser Pulses. Kluwer Academic Publishers, 2002.

[111] R. Barakat and G. Newsam, "Necessary conditions for a unique solution to two-dimensional phase recovery," Journal of Mathematical Physics, vol. 25, no. 11, pp. 3190–3193, 1984.

[112] R. Neutze, R. Wouts, D. van der Spoel, E. Weckert, and J. Hajdu, "Potential for biomolecular imaging with femtosecond x-ray pulses," Nature, vol. 406, no. 6797, pp. 752–757.

[113] D. Gabor, "A new microscopic principle," Nature, vol. 161, no. 4098, pp. 777–778, 1948.

[114] D. Gabor, "Holography, 1948-1971," Science, vol. 177, no. 4046, pp. 299–313, 1972.

[115] J. B. Tiller, A. Barty, D. Paganin, and K. A. Nugent, "The holographic twin image problem: a deterministic phase solution," Optics Communications, vol. 183, no. 1-4, pp. 7–14.

[116] W. F. Schlotter, R. Rick, K. Chen, A. Scherz, J. Stöhr, J. Lüning, S. Eisebitt, C. Gunther, W. Eberhardt, O. Hellwig, and I. McNulty, "Multiple reference fourier transform holography with soft x rays," Applied Physics Letters, vol. 89, no. 16, pp. 163 112–3.

[117] D. Sayre, J. Kirz, R. Feder, D. M. Kim, and E. Spiller, "Transmission microscropy of unmodified biological materials: comparative radiation dosages with electrons and ultrasoft x-ray photons," Ultramicroscopy, vol. 2, no. 4, pp. 337–49, 1977.

[118] R. Henderson, "The potential and limitations of neutrons, electrons and x-rays for atomic resolution microscopy of unstained biological molecules," Q Rev Biophys, vol. 28, no. 2, pp. 171–93, 1995.

[119] Q. Shen, I. Bazarov, and P. Thibault, "Diffractive imaging of nonperiodic materials with future coherent x-ray sources," Journal of Synchrotron Radiation, vol. 11, no. 5, pp. 432–438, 2004.

[120] J. Miao, K. O. Hodgson, and D. Sayre, "An approach to three-dimensional structures of biomolecules by using single-molecule diffraction images," Proceedings of the National Academy of Sciences of the United States of America, vol. 98, no. 12, pp. 6641–6645, 2001.

[121] H. N. Chapman, S. P. Hau-Riege, M. J. Bogan, S. Bajt, A. Barty, S. Boutet, S. Marchesini, M. Frank, B. W. Woods, W. H. Benner, R. A. London, U. Rohner, A. Szoke, E. Spiller, T. Moller, C. Bostedt, D. A. Shapiro, M. Kuhlmann, R. Treusch, E. Plonjes, F. Burmeister, M. Bergh, C. Caleman, G. Huldt, M. M. Seibert, and J. Hajdu, "Femtosecond time-delay x-ray holography," Nature, vol. 448, no. 7154, pp. 676–679.

[122] M. J. Bogan, W. H. Benner, S. Boutet, U. Rohner, M. Frank, A. Barty, M. M. Seibert, F. Maia, S. Marchesini, S. Bajt, B. Woods, V. Riot, S. P. Hau-Riege, M. Svenda, E. Marklund, E. Spiller, J. Hajdu, and H. N. Chapman, "Single particle x-ray diffractive imaging," Nano Lett., vol. 8, no. 1, pp. 310–316, 2008.

[123] S. Marchesini, A. E. Sakdinawat, M. J. Bogan, A. Barty, H. N. Chapman, M. Frank, S. P. Hau-Riege, A. Sz, C. Cui, and D. A. Shapiro, "Massively parallel x-ray holography," Nature Photonics, vol. 2, no. 9, p. 560, 2008.

[124] A. Barty, M. J. Bogan, S. Hau-Riege, S. Marchesini, K. Sokolowski-Tinten, N. Stojanovic, H. Ehrke, A. Cavalleri, D. Stefan, and M. Frank, "Ultrafast single-shot diffraction imaging of nanoscale dynamics," Nature Photonics, vol. 2, no. 7, p. 415, 2008.

[125] X. Zhang, A. R. Libertun, A. Paul, E. Gagnon, S. Backus, I. P. Christov, M. M. Murnane, H. C. Kapteyn, R. A. Bartels, and Y. Liu, "Highly coherent light at 13 nm generated by use of quasi-phase-matched high-harmonic generation," Optics Letters, vol. 29, no. 12, pp. 1357–1359, 2004.

[126] G. Beutier, G. van der Laan, A. Marty, and F. Livet, "Back-illuminated ccd for coherent soft x-ray imaging," The European Physical Journal Applied Physics, vol. 42, no. 2, pp. 161–167, 2008.

[127] B. R. Benware, C. D. Macchietto, C. H. Moreno, and J. J. Rocca, "Demonstration of a high average power tabletop soft x-ray laser," Physical Review Letters, vol. 81, no. 26, p. 5804.

[128] C. D. Macchietto, B. R. Benware, and J. J. Rocca, "Generation of millijoule-level soft-x-ray laser pulses at a 4-hz repetition rate in a highly saturated tabletop capillary discharge amplifier," Opt. Lett., vol. 24, no. 16, pp. 1115–1117.

[129] S. Marchesini, S. Boutet, A. E. Sakdinawat, M. J. Bogan, S. Bajt, A. Barty, H. N. Chapman, M. Frank, S. P. Hau-Riege, and A. Szoke, "Ultrafast, ultrabright, x-ray holography using a uniformly-redundant array," Arxiv preprint arXiv:0801.4969, 2008.

[130] L. M. Stadler, C. Gutt, T. Autenrieth, O. Leupold, S. Rehbein, Y. Chushkin, and G. Grbel, "Hard x ray holographic diffraction imaging," Physical Review Letters, vol. 100, no. 24, p. 245503, 2008.

[131] G. W. Stroke and D. G. Falconer, "Attainment of high resolutions in wavefront-reconstruction imaging," Physics Letters, vol. 13, no. 4, pp. 306–309, 1964.

[132] J. T. Winthrop and C. R. Worthington, "X-ray microscopy by successive fourier transformation," Physics Letters, vol. 15, no. 2, pp. 124–126, 1965.

[133] G. W. Stroke, "Lensless fourier-transform method for optical holography," Applied Physics Letters, vol. 6, no. 10, pp. 201–203, 1965.

[134] G. W. Stroke and D. Gabor, An introduction to coherent optics and holography. Academic Press, New York, 1966.

[135] I. McNulty, J. Kirz, C. Jacobsen, E. H. Anderson, M. R. Howells, and D. P. Kern, "High-resolution imaging by fourier-transform x-ray holography," Science, vol. 256, no. 5059, pp. 1009–1012.

[136] H. He, U. Weierstall, J. C. H. Spence, M. Howells, H. A. Padmore, S. Marchesini, and H. N. Chapman, "Use of extended and prepared reference objects in experimental fourier transform x-ray holography," Applied Physics Letters, vol. 85, no. 13, pp. 2454–2456, 2004.

[137] H. N. Chapman, A. Barty, S. Marchesini, A. Noy, S. P. Hau-Riege, C. Cui, M. R. Howells, R. Rosen, H. He, and J. C. H. Spence, "High-resolution ab initio three-dimensional x-ray diffraction microscopy," Journal of the Optical Society of America A, vol. 23, no. 5, pp. 1179–1200, 2006.

[138] S. Eisebitt, M. Lörgen, W. Eberhardt, J. Lüning, S. Andrews, and J. Stöhr, "Scalable approach for lensless imaging at x-ray wavelengths," Applied Physics Letters, vol. 84, p. 3373, 2004.

[139] H. He, S. Marchesini, M. Howells, U. Weierstall, H. Chapman, S. Hau-Riege, A. Noy, and J. C. H. Spence, "Inversion of x-ray diffuse scattering to images using prepared objects," Physical Review B, vol. 67, no. 17, p. 174114, 2003.

[140] A. L. Lytle, X. Zhang, J. Peatross, M. M. Murnane, H. C. Kapteyn, and O. Cohen, "Probe of high-order harmonic generation in a hollow waveguide geometry using counterpropagating light," Physical Review Letters, vol. 98, no. 12, p. 123904, 2007.

[141] R. I. Tobey, M. E. Siemens, O. Cohen, M. M. Murnane, H. C. Kapteyn, and K. A. Nelson, "Ultrafast extreme ultraviolet holography: dynamic monitoring of surface deformation," Opt. Lett., vol. 32, no. 3, pp. 286–288, 2007.

[142] S. Eisebitt, M. Lörgen, W. Eberhardt, J. Lüning, and J. Stöhr, "Lensless x-ray imaging of magnetic materials: basic considerations," Applied Physics A: Materials Science & Processing, vol. 80, no. 5, pp. 921–927, 2005.